THERMAL AND EXERGO-ECONOMIC ANALYSIS OF A SYSTEM FOR HYDROGEN PRODUCTION INTEGRATED WITH SOLAR PHOTOVOLTAIC PANELS AND CO-GENERATION CYCLE

BY

ABDULLAH MOHAMMED AL-SHARAFI

A Dissertation Presented to the

DEANSHIP OF GRADUATE STUDIES

KING FAHD UNIVERSITY OF PETROLEUM & MINERALS

DHAHRAN, SAUDI ARABIA

In Partial Fulfillment of the

Requirements for the Degree of

DOCTOR OF PHILOSOPHY

In

MECHANICAL ENGINEERING

DECEMBER 2015

KING FAHD UNIVERSITY OF PETROLEUM & MINERALS

DHAHRAN, SAUDI ARABIA

DEANSHIP OF GRADUATE STUDIES

This dissertation, written by **ABDULLAH MOHAMMED AL-SHARAFI** under the direction of his dissertation advisor and approved by his dissertation committee, has been presented and accepted by the Dean of Graduate Studies, in partial fulfilment of the requirements for the degree of **DOCTOR OF PHILOSOPHY IN MECHANICAL ENGINEERING**.

Dissertation Committee

Dissertation Advisor
Dr. Ahmet Ziyaettin Sahin

Co-Advisor
Dr. Bekir S. Yilbas

Member
Dr. Shahzada Z. Shuja

Member
Dr. Abdul Khaliq

Member
Dr. Mazen M. Khaled

Department Chairman
Dr. Zuhair M. Gasem

Dean of Graduate Studies
Dr. Salam A. Zummo

11/1/16
Date

DEDICATION

To My Parents … To My Family

ACKNOWLEDGMENTS

I am most grateful to Almighty ALLAH, the Beneficent, the Merciful, for enabling me to complete this work. First and the foremost acknowledgments are due to the King Fahd University of Petroleum and Minerals and to the Department of Mechanical Engineering for supporting my research work.

I wish to express my deep appreciation and heartfelt gratitude to Dr. Ahmet Z. Sahin, my dissertation advisor for his unfailing encouragement, advices and suggestions through this work. I also wish to thank my dissertation Co-Advisor, Dr. Bekir S. Yilbas for his constructive guidance, support and continuous help during my work. Deep appreciation also goes to my PhD dissertation committee members, who perused my dissertation and recommended important improvements.

My deep thanks and appreciations are due to my beloved parents, my wife, my children my brothers, and rest of the family members who always prayed for my success.

TABLE OF CONTENTS

LIST OF TABLES

LIST OF FIGURES

ABSTRACT (ENGLISH)

NAME: ABDULLAH MOHAMMED AL-SHARAFI

TITEL: THERMAL AND EXERGO-ECONOMIC ANALYSIS OF A SYSTEM FOR HYDROGEN PRODUCTION INTEGRATED WITH SOLAR PHOTOVOLTAIC PANELS AND CO-GENERATION CYCLE

MAJOR: MECHANICAL ENGENEERING

DATE: DECEMBER 2015

Renewable energy resources have a great potential to cover large share of the world energy demand. However, an efficient energy storage system is essential which contribute significantly to overall cost. A direct solar energy conversion to chemical fuel would be one of the solutions for this problem. A hydrogen production system, which utilizes renewable energy resources, is promising for cost effective energy storage as compared to the other energy storage systems. One possible way is to produce hydrogen from waste water or nanofluid composing of water-Carbon Nanotubes (CNT) mixture via electrolysis process while incorporating the electrical energy generated by the renewable energy resources. Performance assessment of such multi-generation system is challenging because of the number of variables that have to be taken into account. Relaying on only one performance index such as energy efficiency, exergy efficiency or the cost of energy, may lead to erroneous decision for the selection of the size of the system components. An innovative idea is to establish a new performance assessment tool, which is called Overall Performance Index (OPI). OPI can combine multiple number of performance indicators with capability of assigning each one of them a weight depending on its impact on the system performance. The optimum number and size of such system components can then be decided for system configuration maximizing OPI. In this regard, an example of exergo-economic analysis of a combined cycle power generation system is introduced for efficiency and performance improvements incorporating GT PRO/PEACE Software Packages.

This study is extended to include investigations of power generation and hydrogen production potentials via solar and wind renewable energy resources at different locations in the Kingdom of Saudi Arabia, namely; Dhahran, Riyadh, Jeddah, Abha and Yanbu. These locations represent the climatic conditions variety in the Kingdom with different solar radiation and wind speed potentials. At each location, different renewable off-grid power generation systems are considered to cover a load demand of a typical house. These system incorporate; photovoltaic (PV) array, wind turbines, converter, batteries, electrolyzer, fuel cell (FC) and hydrogen tank. Consequently, six systems are considered in hourly base simulations, namely; PV/battery bank, wind/battery bank, PV/wind/battery bank, PV/FC, wind/FC and PV/wind/FC. Simulation and optimization studies are carried out to identify the most cost effective configuration of each system considered. The results show that integration of 2 kW PV array, 3 wind turbines, 2 kW converter and 7 batteries storage bank is the best configuration that gives the minimum levelized cost of energy (COE) of 0.609 $/kWh in Yanbu area. Replacing the battery bank by a combination of electrolyzer, fuel cell and hydrogen tank, storage system is possible; however, the cost increases due to the initial investment cost of the system components. Integrating PV/wind/FC in Abha area gives the minimum levelized cost of energy (COE) of 1.208 $/kWh. In the electrolysis process, hydrogen production rate remains low if pure water is used. To increase the production rate, the industrial waste water which has high content of hydrocarbon is introduced. The innovative idea of introducing low concentration ratio of Carbon Nanotubes (CNT) into the water is realized. This enables to increase the electrical and thermal conductivities, since the electrical and thermal conductivities of CNT are much higher than that of the water. To predict the effective thermal and electrical properties of the Nanofluid, COMSOL Multiphysics Software Package is incorporated. Algebraic equations are introduced to formulate the data obtained from the simulations for temperature dependent effective properties. It is demonstrated that the hydrogen production rate is enhanced via incorporating either industrial waste water or CNT-water nanofluid in the electrolysis process.

ABSTRACT (ARABIC)

ملخـــــص الرسالـــــة

الاسم : عبدالله محمد الشرفي

العنوان : تحليل حراري، إكسيرجي وحساب التكاليف لنظام إنتاج الهيدروجين مرتبط بخلايا الطاقة الشمسية ودورة الإنتاج المزدوج

التخصص : الهندسة الميكانيكية

التاريخ : ديسمبر 2015

إن مصادر الطاقة المتجددة لديها إمكانات كبيرة لتغطية حصة كبيرة من الطلب العالمي على الطاقة. ذلك يتطلب تركيب نظام عالي الكفاءة لتخزين الطاقة الأمرالذي يؤدي إلى رفع التكلفة. إن إمكانية تحويل الطاقة الشمسية إلى وقود كيميائي بطريقة مباشرة يشكل أحد الحلول لهذه المشكلة. يشكل نظام إنتاج الهيدروجين الذي يستخدم موارد الطاقة المتجددة إمكانية واعدة لتخزين الطاقة بتكلفة منخفضة مقارنةً مع أنظمة التخزين الأخرى. من الممكن إنتاج الهيدروجينن عن طريق التحليل الكهربائي للمياة العادمة أو للمائع النانوي المصنع من خليط الماء و أنابيب الكربون النانوية (CNT) مع توليد الطاقة الكهربائية اللازمة من مصادر الطاقة المتجددة. إن تقييم أداء نظام متعدد لتوليد الطاقة يمثل تحديا وينطوي على مهام معقدة نظرا لوجود العديد من المتغيرات التي يجب أن تؤخذ بعين الاعتبار. الإعتماد على مؤشر أداء واحد فقط مثل كفاءة الطاقة، كفاءة الإكسيرجي أو تكلفة توليد الطاقة، قد يؤدي الى قرار خاطئ في إختيار أحجام مكونات النظام. فكرة مبتكرة تتمثل في إنشاء مؤشر جديد لتقييم الأداء، وهو ما يسمى مؤشر الأداء العام (OPI). يمكن أن ينطوي مؤشر الأداء العام على عدد من مؤشرات الأداء مع إمكانية تعيين وزن لكل مؤشر إعتماداً على مدى تأثيره على أداء النظام. إن العدد والحجم المثاليين لمكونات النظام تكمن حيث يتم تحقيق أقصى قيمة لمؤشر الأداء العام (OPI). في هذا الشأن، سيتم التحليل الإكسيرجي-الاقتصادي لنظام توليد الطاقة عبر الدورة المدمجة من أجل رفع الكفاءة وتحسين الأداء باستخدام برنامج GT PRO- PEACE. في هذه الرسالة، تم التحقق من إمكانية توليد الطاقة وإنتاج الهيدروجين عن طريق موارد الطاقة الشمسية وطاقة الرياح المتجددة في مواقع مختلفة في المملكة العربية السعودية، وهي: الظهران، الرياض، جدة، أبها وينبع حيث تعكس هذه المواقع تنوع الظروف المناخية في المملكة واختلاف موارد الإشعاع الشمسي وسرعة الرياح. في كل موقع، تمت دراسة أنظمة مختلفة منفصلة عن الشبكة الكهربائية لتوليد الطاقة من موارد الطاقة المتجددة لتغطية الطلب الكهربائي لمنزل نموذجي عن طريق دمج: مصفوفات خلايا الطاقة الشمسية (PV)، توربينات الرياح، محول كهربائي، بنك بطاريات، وحدة التحليل الكهربائي، خلايا الوقود (FC) وخزان الهيدروجين. عن طريق المحاكاة المعتمدة على كل ساعة في السنة، تمت دراسة ستة أنظمة: خلايا الطاقة الشمسية (PV) / بنك بطاريات، توربينات الرياح/ بنك بطاريات، خلايا الطاقة الشمسية (PV) / توربينات الرياح / بنك بطاريات، خلايا الطاقة الشمسية (PV)/ خلايا الوقود (FC)، توربينات الرياح / خلايا الوقود (FC)، خلايا الطاقة الشمسية (PV) / توربينات الرياح

/ خلايا الوقود (FC). تهدف المحاكاة إلى تحديد عدد وحجم مكونات النظام التي تؤدي إلى أفضل أداء مع أقل تكلفة. أظهرت النتائج أن النظام المؤلف من دمج مصفوفة 2 كيلو واط من خلايا الطاقة الشمسية، 3 توربينات الرياح ،محول كهربائي سعة 2 كيلو واط و 7 بطاريات تخزين، يمثل النظام المثالي والذي يؤدي إلى الحد الأدنى لتكلفة الطاقة (COE = 0.609 $ / كيلوواط ساعة) في منطقة ينبع. أظهرت التنائج أنه من الممكن استبدال بنك البطاريات بنظام التخزين الكهربائي المؤلف من: وحدة التحليل الكهربائي، خلايا الوقود (FC) وخزان الهيدروجين. لكن التكلفة تزداد بسبب التكلفة الأولية المرتفعة لمكونات النظام. إن دمج خلايا الطاقة الشمسية (PV) / توربينات الرياح / خلايا الوقود (FC) في منطقة أبها يعطي الحد الأدنى تكلفة (COE = 1.208 $ / كيلوواط ساعة). في عملية التحليل الكهربائي، يكون معدل إنتاج الهيدروجين منخفضاً إذا تم استخدام مياه نقية. لزيادة معدل الإنتاج، من الممكن إستخدام مياه الصرف الصناعي التي تحتوي على كمية كبيرة من الهيدروكربونات. فكرة مبتكرة تكمن في إضافة نسبة تركيز منخفضة من أنابيب الكربون النانوية (CNT) إلى الماء تؤدي إلى زيادة الموصلية الكهربائية والحرارية للخليط بسبب أن الموصلية الكهربائية والحرارية لأنابيب الكربون النانوية (CNT) أعلى بكثير من مثيلاتها للماء النقي. لإيجاد الخصائص الحرارية والكهربائية الفعالة للمائع النانوي (Nanofluid)، تم إستخدام برنامج (COMSOL Multiphysics). عن طريق نتائج المحاكاة، تم تطوير نموذج عددي للتنبؤ بالخصائص الفعالة للمائع النانوي (Nanofluid) والتي تتفق جيداً مع نظيراتها التي تم الحصول عليها من التجارب المعملية. تم إيجاد معادلات جبرية لصياغة البيانات التي تم الحصول عليها من نتائج المحاكاة للخصائص الفعالة للمائع النانوي مع تغير درجة الحرارة. من خلال التجارب المعملية، تم إثبات أن معدل إنتاج الهيدروجين يزداد من خلال إستخدام مياة الصرف الصناعي أو المائع النانوي المصنع من خليط الماء و أنابيب الكربون النانوية (CNT) في عملية التحليل الكهربائي.

CHAPTER 1

INTRODUCTION

Today, energy applications are integral part of people's lives such applications include cars, mobile phones, medicines, air conditioning, heating and cooling, and etc. These applications extend beyond the individual use to vast areas which entirely depend on availability of energy resources, such areas include; agriculture, computing, manufacturing, construction, health and social services. Furthermore, world energy consumption is increasing substantially and energy in different forms became an essential requirement for the social, cultural, and economic developments in recent years. Therefore, the importance of energy in the life of the individual and the communities has drawn the attention of scientists and researchers in various scientific fields to conduct research on utilization of the available traditional resources in an efficient manner and to integrate renewable energy resources with commercially viable domestic energy systems.

In the recent years, renewable energy alternatives became the best solutions for the global warming and greenhouse effects resulted from the continuous use of the

conventional energy resources like coal and oil. However, renewable energy systems still suffer from the high cost of the equipments especially, storage systems. The most promising renewable energy resources are solar and wind. To secure 100% off-grid power supply using renewable energy resource, an efficient storage system becomes necessary, which represents the major contribution to the total cost. Solar energy power generation systems should have large storage systems due to the shortage of the solar radiation at nights or harsh weather conditions and cloudy sky. The power generated from the sun during the day lights should be stored and used at the night time where the load demand is usually higher. On the other hand, the power generated by a wind turbine is proportional to the third power of the local wind speed of the installation location. Each wind turbine has a shortage of a high wind speed; in which case, electricity generation rate reduces. If the wind speed of the installation location is less than the cut-in wind speed of the wind turbine, electricity generation will not be available and hence, utilization of the storage system becomes essential. Incorporating more than one renewable energy resources in a hybrid system increases the system reliability and decreases the size of the storage system. Usually, a storage battery bank is used in renewable energy systems. The life time of the battery bank is low comparing with the other renewable energy system components and they have to be replaced many times during the project life time. In addition, it represents a large contribution to the total cost of the off-grid renewable energy generation systems.

Hydrogen is considered as a storage mean of energy, which in the future can be vastly used for transportation applications both in private cars and buses for public transportation. It has the highest energy density comparing with the other fuels with (120

MJ/kg) [1]. In addition, it can be used as energy storage media with low cost comparing with the current storage ways. It can be produced through steam reforming of coal and natural gas or through water electrolysis. For better sustainability, hydrogen can be produced through water electrolysis using renewable energy resources which ensures pollution free and recyclable process. This clean process is given the name “hydrogen economy” where hydrogen is produced from a verity of renewable energy resources and is considered as the energy storage medium and energy carrier [2].

1.1 Motivation

Due to the fact that conventional energy resources, practically the fossil fuels, are depleted, more effort is given towards innovative modifications of the traditional power plants for more efficient power generation. In this regard, it is possible to produce multiple outputs from such power generation systems like cogeneration and combined power plants where more than one form of energy such as heat and electric power are produced.

Wider use of fossil fuels produces adverse effects by unfavorable recent climate change as well as constraints from greenhouse gasses emissions. Fuel demanding sectors, such as transportation, impose utilization of environmentally friendly technologies which can contribute to increase hydrogen production, which is considered as energy carrier for future applications. The state-of-the-art of using renewable energy for hydrogen production, made the main motivation of this study. The utilization of solar and wind

renewable energy resources from technical and economical point of views, electricity production which can subsequently be exploited for hydrogen production, which can be examined through water electrolysis. Hydrogen production rate is low when pure water is used. In the current research, an experimental investigation of the hydrogen production rate enhancement is carried out via using waste water in the electrolyzer cell. Another interesting idea is the introducing of small concentration of Carbon Nano Tubes (CNT) into the water. This arrangement would lead to enhancement of the thermal and electrical conductivities of the mixture and increase the hydrogen production potential. A new numerical approach to predict the effective properties of the water-CNT nanofluid mixture is introduced utilizing COMSOL Multiphysics Finite Element Software [3].

1.2 Scope of the Work

This dissertation is associated with different aspects which are involved with increasing the contribution of renewable energy resources for meeting the energy application sectors demand and producing hydrogen. Moreover, introducing a new tool for performance assessment of the cogeneration power plants is accomplished towards increasing the efficiency and improvement of the system performance. Because of that, the present research involves with multifold aspects. More details about the scope of the work are given in the following subsections.

1.2.1 Overall Performance Index for Combined Power Plants

Designing a combined cycle power generation systems is a complicated task due to the number of variables that needs to be considered in design configuration. Relying on only one performance index to assess the hybrid system performance may leads to wrong selection of the system configuration. In the present work, a new approach of assessing the performance of a combined cycle power plant using the concept of overall performance index (OPI) is presented [4]. The overall performance index can involve any number of indicators that are important for assessment of the thermodynamic system with capability to assign each one of them a weight depending on its importance on the overall performance. As a case study, performance assessment of a combined cycle power plant is investigated based on OPI analysis.

In this part, an exergo-economic analysis of a combined cycle power plant is carried out by changing the operation conditions, namely; ambient temperature and relative humidity for different values of the gas turbine pressure ratio. In the combined cycle power plant, there is a gas-turbine (Brayton) cycle topping a steam turbine (Rankine) cycle. Brayton cycle operates at much higher temperature level comparing with Rankine cycle. Therefore, the combined cycle has a higher thermal efficiency comparing with either Brayton or Rankine cycle executed individually. The high temperature exhaust gas is used as the energy source for the bottoming cycle which is the steam power cycle.

Traditionally, first law of thermodynamic including the generated power and the thermal efficiency or the second low exergy efficiency were used for system performance assessment; however, in the present study, the (OPI) concept is used to combine energy

efficiency, exergy efficiency, levelized cost of electricity and total investment. The simulations are carried out incorporating GT PRO/PEACE Software Packages [5]. The best performance of the thermodynamics power plant will be at the point where the OPI can be maximized.

1.2.2 Using Different Renewable Energy Systems for Power Generation and Hydrogen Production in KSA

The aim of this part is to investigate the potentials of power generation and hydrogen production via solar and wind renewable energy resources. To reflect the climatic conditions variety in the Kingdom with different solar radiation and wind speed potentials, different locations in the Kingdom was considered in the hourly base simulations, namely; Dhahran, Riyadh, Jeddah, Abha and Yanbu. Different renewable off-grid power generation systems are considered to cover a load demand of a typical house incorporating; photovoltaic (PV) array, wind turbines, converter, batteries, electrolyzer, fuel cell (FC) and hydrogen tank. Six systems are considered in the simulations, namely; PV/battery bank, wind/battery bank, PV/wind/battery bank, PV/FC, wind/FC and PV/wind/FC. The simulations and the optimizations studies are carried out to identify the cost effective configurations with aid of Hybrid Optimization of Multiple Energy Resources Software (HOMER [6]).

In this regard, feasibility study and economical analysis for using renewable energy resources to meet a load demand of a typical house are carried out. The possible

renewable energy resources are solar, wind or a combination of solar and wind in a hybrid system. The storage systems considered are either consisting of battery bank or a combination of electrolyzer, fuel cell and hydrogen tank, storage system. For each system, different sizes of the system components are incorporated. Any combination of the sizes or numbers of these components leads to one configuration of the system. The main goal of any configuration is to cover the load in every hour during one complete year by renewable energy without any deficiency. Any configuration that is not meeting the requirements is to be discarded. The configurations that are meeting these requirements are ranked based on the total net present cost and the one that has the minimum cost is considered as the optimum configuration. The simulation results of these six different renewable systems are explained in detail for Dhahran area incorporating one complete year weather data. The best system that leads to the minimum cost while meeting the load requirements is specified. To have the insight of changing the location of these renewable energy systems, the hourly based simulations are repeated for the other four different locations namely; Riyadh, Jeddah, Abha and Yanbu. The simulation results are analyzed to assess the renewable energy potential at these different locations in accordance with the best performance. In addition, assessment of hydrogen production via renewable energy is carried out for the systems that have the combination of electrolyzer, fuel cell and hydrogen tank as a storage system.

1.2.3 Thermal and Electrical Characteristics of Water-CNT Nanofluid

Using of high conductive nano particles, such as carbon nanotubes (CNT), enhances the thermal and electrical conductivities of the carrier fluid. Depending upon the volumetric concentration of particles and their distribution in the carrier fluid, multifold enhancement of thermal and electrical properties is possible. Using the mixture in the electrolysis process would lead to enhance the rate of hydrogen production. It is an essential step to measure the nanofluid effective properties before using it in the electrolysis process.

Therefore, in this part of the dissertation, thermal and electrical properties of water-CNT mixture are assessed at microscopic level. Intensive work is carried out to numerically predict the effective thermal and electrical properties of the nanofluid incorporating the same conditions of the experimental measurements. Special distribution of the carbon nanotubes in water is obtained experimentally at micro scale for different durations of the heating situation of the nanofluid. Thermal and electrical properties are predicted numerically incorporating the particle distributions obtained from the experiment. The mass based analysis is also introduced to determine the thermal properties of the mixture. The findings are compared for those obtained from the simulations based on experimentally obtained micro-images. Algebraic equations are introduced to formulate the data obtained from the simulations for temperature dependent properties at different concentration ratios.

CHAPTER 2

LITERATURE REVIEW

2.1 Introduction

This dissertation involves with different aspects towards improved utilization of the traditional power generation methods that use the conventional fossil fuel resources and increasing the contribution of the renewable energy applications. Therefore, in this chapter, a literature survey is carried out, which summarize the findings of various research papers focusing on thermal power plants performance assessments, renewable energy utilization, thermal and electrical properties of water-CNT nanofluid, and hydrogen production by electrolysis via renewable energy resources.

2.2 Literature Survey

Performance assessment of hybrid Power Plant systems is very important for design and prior to installation. In general, the combined cycle power generation system consists of many components with relatively high costs. The selection of the numbers and sizes of these components is mainly subjected to the designer purposes while satisfying a required reliability limit. Therefore, it becomes necessary to gather data and information about all related components associated with the system. This can be carried out to provide a statistical measure of how the system performance changes over time using proper simulation schemes and programs. Traditionally, thermodynamic system performance is evaluated by the first law of thermodynamic including the generated power and the thermal efficiency. The second law exergy efficiency provides additional insight toward improvement of thermodynamic systems performance and optimization. Recently, exergy, exergo-economic and environmental analysis are introduced to analyze thermal performance of a combined cycle power plant. The exergy analysis can be incorporated to determine the exergy destruction magnitude and exergy losses at each component of the power plant system which helps the designer for possible effective improvements [7-10]. Exergo-economic analysis relates the exergy analysis to the associated costs, in which the target is to minimize the exergy destruction and the levelized cost of electricity [11]. Extensive research studies were carried out to assess the performance of combined cycle power plants seeking higher thermal efficiency, less environmental impact and utilizing the available exergy potential [12-17].

In this regard, Ozturk [18] analyzed the energy and exergy efficiencies of a combined ground source heat pump system that consists of a heat pump cycle, a radiator thermal cycle, a ground heat exchanger cycle and a cooling tower cycle. Parametric study is conducted by changing the operation conditions. He found that the exergy efficiency decreases and exergy destruction is minimized with increasing the ambient temperature.

Exergy analysis of a combined power and cooling cycle that integrate a Rankine and absorption refrigeration cycle is conducted by Fontalvo et al. [19] in which they used ammonia-water mixture as the working fluid. MATLAB computer code was developed to assess the performance of the combined cycle. Their results revealed that overall exergy destruction decreases with increasing the pressure ratio and increasing the turbine efficiency reduces the total exergy destruction.

Baghernejad and Yaghoubi [20] studied the performance of solar parabolic trough integrated with combined cycle power plant incorporating first and second laws of thermodynamic efficiencies in the analysis. The assessment of the performance was based on the real data collected from a local power plant in which case, 159 MW, 132 MW and 17 MW were produced by gas turbines, steam turbine and solar plant, respectively. They found that the solar collectors are the main source of irreversibilities in the plant with exergy efficiency of 27% due to the materials and manufacturing constrains.

Exergo-economic and environmental assessment of a cogeneration of heat and power cycle is carried out by Khaljani et al. [21] incorporating first and second law efficiencies as well as the economical aspect. Thier results revealed that the most exergy

destruction occurs at the combustion chamber followed by the steam generator, gas and steam turbines, respectively. Monitoring the exergo-economic factor showed that 85.11 % of the cost, is due to exergy destruction cost whereas only a 14.89 % of that is due to cost of investment.

Al-Sulaiman [22] carried out an exergy analysis of either Rankine or a combined cycle topping an organic Rankine cycle in which, seven different refrigerants were examined. The thermal power system was driven by parabolic trough solar collectors. An Engineering Equation Solver (EES) computer code was developed to accomplish the simulations. His results revealed that the exergetic efficiency is proportional to the solar radiation and more than 50% of inlet exergy is destructed in the solar collector and more than 13% of the inlet exergy is destructed in the evaporator.

Global warming and pollutions have great impacts on the life on the Earth in the recent decades that have driven scientists to utilize the new clean energy resources. Renewable energy resources have received more attention for environmental friendly power generation. Solar and wind power generation systems are the most attractive alternatives [23-26]. The generated power from these resources is influenced by the climatic conditions, such as; solar radiation, wind speed, ambient temperature, etc…[27]. Although renewable energy generation is growing, storing energy remains the missing link for clean power generation [28].

Hydrogen is one of the excellent fuels with high energy storage capacity. Hydrogen can store energy for long time and its combustion produces water only without

causing environmental pollutants. Furthermore, hydrogen has an economic advantage over the batteries for long time storage [29].

For hydrogen to play a major role in the energy sector in the mid to long term future, one must be able to produce hydrogen in an environmentally responsible and cost effective way. It can be produced through steam reforming of coal and natural gas or through water electrolysis by supplying the required power from either fossil fuel resources or renewable energy resources in order to reduce the pollutions. The combination of water electrolyzer, fuel cell and hydrogen tank can be used as an alternative storage system replacing the battery bank. For such load requirement, when the output power of the renewable energy system covers the load demand at the corresponding time, the surplus energy goes to water electrolyzer where hydrogen is generated. Hydrogen tank is used to store the hydrogen for later use. Many research studies were carried out to investigate the potential of using renewable energy resources for hydrogen production.

In this regard, Kalinci [30] compared different renewable energy alternatives that are used to produce electricity for Bozcaada Island, Turkey where good potential of solar energy is reported. The simulations and the optimization are realized by incorporating HOMER Software for the renewable-grid connected systems and standalone systems. His results showed that the most suitable grid connected system was grid-wind with 0.103 $/kWh, levelized cost of energy (COE) whereas the suitable off-grid system was wind-photovoltaic (PV)-fuel cell (FC) with COE of 0.836 $/kWh.

The use of a PV- fuel cell - battery system was evaluated by Silva et al. [31] to meet the load demand of a remote environmental protective area in the Amazon region. They compared the use of hydrogen electrolyzer and tank or the use of batteries as energy storage alternative with the aid of HOMER Software. They study concluded that the batteries were still the best option to store the energy and the levelized cost of electricity is 1.352 $/kWh.

Dursun [32] studied the potential of meeting the load demand of a university campus in Turkey by renewable energy. He considered a system that incorporates PV and fuel-cell system to reduce the conventional power generation ways impact on the local environment. His study showed that the grid connected systems has the lowest cost of investment and the lowest cost of energy and the grid connected-PV-fuel cells system has the cost of energy of 0.294 $/kWh.

Kingdom of Saudi Arabia has a high potential of renewable energy resources of solar and wind. The range of the average daily solar radiation varies from 4 to 7.5 kWh/m^2 whereas it is only 1 kWh/m^2 in Europe [33]. Many studies have been carried out for different renewable energy systems alternatives in different locations in the Kingdom [34-38]. The results of these studies showed that this country with a vast area and many scattered villages and locations had a great potential of standalone solar and wind power generation systems.

The electrical and thermal transport properties of fluids can be enhanced through introducing high thermal and electrical conductive nano-particles like carbon nanotubes (CNT) into the carrier fluid while forming the nanofluid mixture (liquid dispersions of

nanoparticles). This arrangement introduces an innovative solution to overcome the inherently poor properties of the water due to their low electrical and thermal conductivities. This arrangement gives an opportunity to enhancement of the hydrogen production rate of an electrolysis process via using the water-CNT mixture in the electrolyzer.

The importance of the nanofluids is associated with their high potential to be the working fluids for the applications where the high thermal performance is required such as solar collectors, heat exchangers, air-conditioning, electronic cooling systems, and nuclear reactors etc. Furthermore, carbon nanotubes (CNT) can be mixed with the carrier fluid to improve the electrical conductivity, such as in the water electrolysis reactor enhancement of the electrical conductivity. In this case, mixing the CNT and the carrier fluid is necessary to improve the rate of the Hydrogen production with minimum electric resistance in the system.

In most of the applications, thermal properties such as thermal conductivity and specific heat capacity of the carrier fluid are estimated incorporating mass based analysis and with particle shape factor connections. However, assumption of the shape factor and mass based analysis result in erroneous thermal properties of the carrier fluid. Consequently, investigation of the thermal properties of water-carbon nanotubes mixture at microscopic level becomes essential.

In the regard of nanofluids characterization, Harish et al. [39] studied the effect of mixture of single wall carbon nanotubes (SWCNT) with ethylene glycol on the effective thermal conductivity. Their findings showed that enhancement of the effective thermal

conductivity was possible and the improvement reached to maximum for 14.8% for 0.2% volume fraction of the SWCNT.

Influence of CNT structures on thermal conductivity of nanofluid was investigated by Nasiri et al. [40]. They incorporated five different structures, namely; single, double and two different multiwall carbon nanotubes (CNT) and the findings revealed that the stable thermal conductivity enhancement was possible for all the nanostructures considered.

SiO_2 and Al_2O_3 water based nanofluids were characterized, in terms of thermal conductivity, specific heat and viscosity, by Mondragon et al. [41]. They observed that adding silica and alumina to the water resulted in enhancement of the thermal properties of the mixture, provided that, the thermal conductivity decreased at high temperatures ($T \geq 80$ C°). This behavior at this temperature was associated with the solubility of the nanoparticles which could cause the decrease of thermal conductivity.

Jeong et al. [42] experimentally investigated the viscosity and thermal conductivity of ZnO nanofluids. Their findings revealed that for 0.05 to 5 volume percent of ZnO, the viscosity and thermal conductivity were higher than those of the base fluid by 5.3 to 68.6% and 3 to 19.8%, respectively.

Second law analysis of nanofluid flow has been carried out by Moghaddami et al. [43]. They examined the effects of nanoparticles on the entropy generation rate of water-Al_2O_3 nanofluid flows through a circular pipe under uniform wall heat flux condition. Their results showed that inclusion 1% volume concentration of nanoparticles decreased the total entropy generation about 3.6%.

Effect of copper–water nanofluid as a cooling medium was studied numerically incorporating the finite volume approach by Santra et al. [44]. Their findings revealed that heat transfer enhancement took place for increased in solid volume fraction for all Reynolds numbers considered. An experimental investigation of Fe_2O_3 nanofluids with varying mass concentrations ranging between 5 and 20% was carried out by Colla et al. [45]. They showed that thermal conductivity enhancement was proportional to temperature increases and Fe_2O_3 particle concentration.

Extensive research findings have been reported in the previous studies [46-51] exploring the predictive models for thermal conductivity of carbon nanotubes based nanofluids, such as, Maxwell model [49], Hamilton and Crosser model [50], Yu and Choi model [51] and etc. They recommended further parametric studies to produce high impact on the analytical models incorporating carbon nanotubes length and volume fraction.

The flow characteristics of a stationary liquid droplet are influenced by the Marangoni flow and natural convection when temperature gradient is generated across the droplet. Addition of carbon nanotubes (CNT) to the fluid modifies the flow and heat transfer characteristics of the droplet. This is attributed to the change of thermal properties such as thermal conductivity and specific heat capacity of the carrier fluid. Since the thermal response of the carrier fluid in the droplet is transient, varying surface tension gradient with temperature during the heating period alters the flow and heat transfer characteristics within the droplet. In addition, the wetting characteristics and the contact angle of the droplet depend on the surface texture and surface free energy of the solid substrate. In this case, changing the contact angle of the droplet through modifying the surface

characteristics in terms of texture and free energy varies the heat transfer rates and flow field within the droplet [52]. The thermal response of the droplet is involved with multi-physics; therefore, numerical investigation provides useful information about the physical insight into the thermal-flow behavior in the droplet.

Since the flow and heat transfer characteristics depend on the thermal properties of the carrier fluid in the droplet and the droplet contact angle, investigation into thermal and flow characteristics becomes essential. Considerable research studies were carried out to examine the droplet behavior, heat transfer characteristics, evaporation, and condensation of water droplets [53-57].

In this regard, Wegener [58] studied the effects of droplet diameter, kinematic viscosity ratio and interfacial tension gradient, on the heat transfer in a droplet incorporating the Marangoni flow. The predictions showed that the droplet size strongly influenced the heat and mass transfer characteristics in the droplet unlike the effect of changing the kinematic viscosity ratio. In addition, he demonstrated that smallest gradients in interfacial tension gradient could initiate the Marangoni flow.

Girard et al. [59] showed that the influence of the Marangoni convection current on the evaporation rate was negligible for the small water droplets heated on the hot surface. Their findings revealed that the approach based on heat diffusion was sufficient to estimate the evaporation rates from the droplet.

Thokchom et al. [60] investigated the effects of surface temperature and the aggregation of solute polystyrene particles on the flow field inside a water droplet. They used particle image velocimetry (PIV) technique to determine the particles velocity

within the droplet. Bhardwaja et al. [61] studied the formation of deposits during drying of nano-liter colloidal drops on a flat substrate. Their findings revealed that Marangoni convection significantly influenced the internal flow and the deposit pattern, which was assessed from a ring-like pattern, formed in the droplet.

Huang et al. [62] investigated the influence of contact angle on freezing process of a water droplet laying on a cold hydrophobic surface. They used a copper foil surface prepared through a chemical etching and fluorination modification method. They found that the droplet size had a strong influence on the complete freezing time; in addition, increasing contact angle resulted in extension of the freezing period.

Talbot et al. [63] investigated evaporation rate of picolitre water and ethanol droplets on different substrate surfaces. Their results showed that the drying time was strongly dependent on the surface hydrophobicity, in which the evaporation rate was faster for the hydrophobic surfaces.

The detailed examination of Marangoni induced flow field was presented earlier [64, 65] and thermocapillary driven flows are reviewed by Schatz and Neitzel [65]. Moreover, some of the research studies focused on the evaporation of microlitre droplets [66-69]. It was demonstrated that under laboratory environment (1 atm ambient pressure and 300 K temperature), the evaporation rate was low due to the limited diffusion rate of the vapor from the liquid-vapor interface into the ambient atmosphere. However, when the droplet size was considerably small, the evaporation could be governed by the kinetics of the molecular transfer across the interface.

Lu et al. [70] carried out simulation of the evaporation of a liquid droplet on a heated surface. They considered the effect of buoyancy force, thermo capillary force, and viscous resistance. Their results showed that Marangoni convection resulted in a counterclockwise circulation cell while natural convection caused a clockwise circulation cell within the droplet. Although both enhanced the evaporation rates, the largest increase took place due to Marangoni convection.

The influence of the nano-particles on the flow field and heat transfer characteristics in a droplet of carrier fluid has not been examined extensively. Consequently, in this dissertation, droplets formed from the carrier fluid composes of a mixture of water and carbon nanotubes (CNT) is considered and the numerical simulation is carried out to examine the fluid motion in the droplet of water-CNT mixture. In the analysis, effects of Marangoni and natural convection on the flow field are incorporated. The effective thermal properties of the carrier fluid are analyzed using microscopic technique.

Under optimistic technological and economic assumptions, recent scenarios are showing a possible hydrogen demand of 3% up to 8% of the global final energy demand until 2050 [71]. In this part of the literature review, the concentration will be mainly given of the previous work that focused on the hydrogen production by electrolysis.

Eker et al. [72], used a wastewater taken from PAK MAYA Bakers Yeast Company, Izmir, Turkey- for Hydrogen production. They used PV cells to produce the required electricity for the electrolyzer using electrodes made from stainless steel. They compared the amount of the Hydrogen produced from the waste water and from tap water in time period of eighteen days (432 hours). They compared the hydrogen production rate

when using tap water or wastewater. The resultant hydrogen production rate was 0.522 Lit/day using tap water whereas it was about 4.32 Lit/day using wastewater. These results proved that considerable improvement of hydrogen production rate by utilizing wastewater.

The same setup device of [73] was used by Kargi , to compare three types of electrodes, graphite, stainless steel and aluminum rods to produce hydrogen by water electrolysis. The results of Karagi showed that using the aluminum electrode leads to the maximum hydrogen gas formation (CHF) (120 liters in 8 days) and the minimum was with the graphite electrode (4 Lit). So the electrode that is made from aluminum was the best option among the three used materials.

Coskun et al. [74] conducted a study to find out the possibility of producing biogas and hydrogen from a milk-processing waste water (70% Methane and 30% CO_2) in Turkey. Their results indicated that a maximum of 54.2 million m3 biogas/yr and 12,670 ton H_2/yr can be produced from waste water. The overall energy efficiency of the hydrogen production using different reforming processes at different temperatures was between 19 and 70%. The overall exergy efficiency for 900˚C reforming and different ambient temperatures was ranging from 8 to 48%.

In light of the previous literature survey, it is clear that relying on one indicator for thermal power plants performance assessments may lead to wrong selection of the sizes of the system components. Therefore, in this dissertation, an exergo-economic analysis is carried out for a combined cycle power plant using the first law and the second law of thermodynamics and the economic principles while incorporating GT PRO/PEACE

Software Packages [5]. An Overall Performance Index (OPI) is defined and MATLAB computer code is developed to assess and analyze the optimum operational and design configuration of the power plant [4]. Four performance indicators are considered for the analysis; namely, energy efficiency (ENE), exergy efficiency (EXE), levelized cost of electricity (COE), and the total investment (TI) cost. OPI combines these four indicators depending on their impact on the system performance and user demands. Three possible scenarios are considered in which different weight factor is assigned to the performance indicators when assessing the performance. These scenarios are: i) the conventional case in which the levelized cost of electricity is given a high priority, ii) environmental conscious case in which the exergy efficiency is given a high priority, and iii) the economical case in which the total cost of investment is given a high priority. In each case, the best system configuration will be at the point that OPI can be maximized.

Renewable energy potential is considerable in the Kingdom of Saudi Arabia. Therefore, an assessment study is carried out to integrate solar and wind renewable energy resources to meet a load requirement and contribute to reduce the greenhouse effects and global warming phenomena resulting from the extensive use of the conventional fossil fuels. Renewable energy applications require efficient storage systems such as battery bank. In this dissertation, six different renewable energy systems scenarios are incorporated to cover such load demand and hydrogen production utilizing different storage systems. In the present study, the concentration is also given to the enhancement of the hydrogen production through electrolysis process and how to improve it by using either wastewater, which has high amount of hydrocarbons or by adding Carbon Nano Tubes (CNT) particles to the water which act as a catalyst to enhance the water thermal and

electrical conductivities. Predicting the effective thermal and electrical properties of the water-CNT mixture is essential before using it in the electrolysis process. In this regards, intensive numerical simulations are carried out incorporating COMSOL Multiphysics Software Package [3]. In the simulation, the effective properties of the mixture are predicted via using proper boundary conditions that is in line with the experimental conditions at different concentration ratios. Good agreements are found between the simulation findings and their experimental counterparts. Mathematical relations have been formulated for the effective properties at different concentration ratios and wide temperature range.

CHAPTER 3

MATHEMATICAL ANALYSIS

3.1 Introduction

In this chapter, mathematical models relevant to each aspect of this dissertation are described. First and second laws of thermodynamics analysis related to the energy and exergy efficiencies of a combined power plant are carried out. An economic analysis is also incorporated. The effects of the energy efficiency, exergy efficiency, levelized cost of electricity and total investment, performance indicators are combined in an overall performance index (OPI).

Complete mathematical models of renewable energy (solar and wind) through photovoltaic panels and wind power generators to meet a specific load and for hydrogen production are described. Different energy storage systems are considered. An optimization procedure is developed determine the best combination of the renewable energy system components to minimize the levelized cost of energy.

Numerical simulations are carried out in line with the experimental conditions to predict the effective properties of a mixture of Carbon Nano Tubes and water and characterize the flow and thermal fields in a nanofluid droplet. Mathematical models associated with the numerical simulation are given.

3.2 Combined Cycle Power Plant Performance Analysis

To analyze the performance of such power plant, both the energy and exergy efficiencies are considered. In addition, the net power output of the cycle is analyzed. The levelized cost of electricity (COE) and the total investment are also considered to carry out and exergo-economic analysis. Finally, the overall performance index is introduced to optimize the combined cycle power plant by considering the performance indicators such as energy efficiency (ENE), exergy efficiency (EXE), levelized cost of electricity (COE) and total investment (TI).

3.2.1 Energy Analysis

The schematic diagram for the combined cycle power plant considered in this dissertation is shown in Figure (1). The energy balance (i.e. the first law of thermodynamics) that is applicable to all the steady and uniform flow devices in the combined cycle power plant and it can be written as:

$$\dot{Q}_r - \dot{W} + \sum \dot{m}_{in} h_{in} - \sum \dot{m}_{out} h_{out} = 0 \qquad (3.1)$$

where

$\dot{Q}_r$ is the input heat transfer to the device.

$\dot{m}$ is the mass flow rate.

$\dot{W}$ is the power generation by the device.

h is the enthalpy of the fluid stream.

In Equation (3.1), the kinetic and potential energy terms are assumed to be negligible.

The energy efficiency of the plant is

$$\eta_{th} = \frac{\dot{W}_{gt} + \dot{W}_{st}}{\dot{Q}_{in}} \qquad (3.2)$$

where

$\dot{W}_{gt}$ is the power generated in the gas turbine.

$\dot{W}_{st}$ is the power generated in the steam turbine.

$\dot{Q}_{in}$ is the heat input to the combustion chamber due to the combustion of fuel.

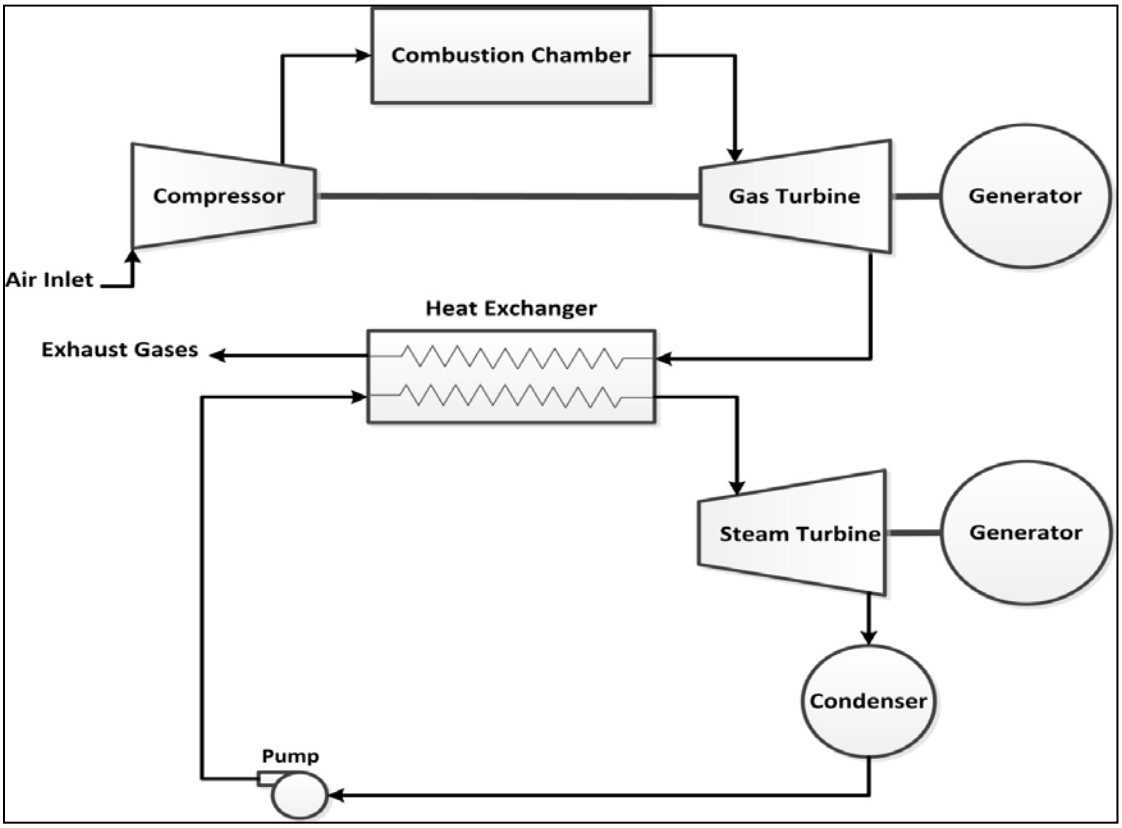

Figure 1: Simplified schematic diagram of the combined cycle power plant.

3.2.2 Exergy Analysis

Exergy analysis is a suitable and efficient method to identify the types, magnitudes and locations of irreversibilities in a thermodynamic system. It considers not only the quantity but also the quality of energy and enables to locate the losses and carry out improvements for better consumption of the useful energy. Both the first and the second laws of

thermodynamics are considered in the exergy analysis to define the second law efficiency of an energy intensive system as a realistic measure of performance.

A given stream of fluid may possess physical and chemical exergy. Physical exergy is defined as the maximum reversible amount of work that can be obtained when the stream of fluid is brought to the environmental state defined as the dead state and given by the standard atmospheric conditions of pressure P_0 and temperature T_0. The physical exergy e_x^{ph} is given by:

$$e_x^{ph} = (h - h_0) - T_0(s - s_0) \tag{3.3}$$

where

h is the specific enthalpy of the stream.

s is the and the specific entropy of the stream.

and

$h_0 = h\ (T_0, P_0)$

(3.4)

$s_0 = s\ (T_0, P_0)$ (3.5)

where $e_x^{ph} = \bar{e}_x^{ph} / M$ is the physical exergy per unit mass.

M is the molar mass.

On the other hand, the chemical exergy is defined as the maximum work that can be obtained when the considered system is brought into reaction with reference substances present in the environment. The values of standard chemical exergies $\bar{e}_x^{ch}$ on the molar basis for various substances can be found in the literature [75]. The chemical exergy of an ideal mixture is given as

$$\bar{e}_{x,mix}^{ch} = \sum_i y_i \bar{e}_x^{ch} + \bar{R} T_0 \sum_i y_i \ln y_i \tag{3.6}$$

where

y_i is the molar fraction of the component i in the mixture.

$\bar{R}$ is the universal gas constant.

Thus, the total exergy of a stream per unit mass flow rate can be written as

$$e_{x,tot} = e_x^{ph} + e_x^{ch} \tag{3.7}$$

where

$e_x^{ch} = \overline{e}_x^{ch} / M$ is the chemical exergy per unit mass.

The amount of irreversibility due to losses $\dot{I}$ in a steady flow device can be evaluated by considering the exergy balance on a control volume across the device, which can be written as:

(Total exergy in) = (Total exergy out) + (Irreversibility losses)

or

$$\sum \dot{m}_{in} e_{x,in} + \dot{Q}_r \left(1 - \frac{T_0}{T_r}\right) = \sum \dot{m}_{out} e_{x,out} + \dot{W} + \dot{I} \qquad (3.8)$$

where

$\dot{W}$ is the power generated by the device.

$\dot{Q}_r$ is the heat transfer rate to the control volume.

$\dot{m}$ is the mass flow rate.

T_0 is the reference ambient temperature.

T_r is the temperature of the reservoir from which the heat transfer occurs.

The second term of Equation (3.8) is the exergy input due to the heat transfer to the control volume.

The irreversibility losses $\dot{I}$ represent the total exergy destruction and are related to the entropy generation rate as

$$\dot{I} = T_0 \dot{S}_{gen} \geq 0 \tag{3.9}$$

Based on the above exergy balance, the exergy efficiency can be defined as

$$\eta_{ex} = \frac{(\text{Total exergy out})}{(\text{Total exergy in})} = 1 - \frac{(\text{Irreversibility losses})}{(\text{Total exergy in})} \tag{3.10}$$

The reference environmental conditions for the exergy analysis were T_0 = 298.15K, P_0 = 101.325 kPa.

3.2.3 The levelized cost of electricity

The levelized cost of electricity (COE) is the net present value ($) of the unit amount (kWh) of electricity generated over the lifetime of the cogenerating plant cycle. In determining the COE, all costs over the lifetime are considered. These include the initial and capital initial cost, operations and maintenance costs, and cost of fuel. Thus, the levelized cost of electricity (COE) is given by [76],

$$COE = \frac{\sum_{t=1}^{n} \frac{I_t + OM_t + F_t}{(1+\delta)^t}}{\sum_{t=1}^{n} \frac{E_t}{(1+\delta)^t}} \quad (3.11)$$

where

I_t investment expenditures in the year t.

OM_t operations and maintenance expenditures in the year t.

F_t fuel expenditures in the year t.

E_t electricity generation in the year t.

δ discount rate.

n expected lifetime of system or the combined cycle power plant.

3.2.4 Overall Performance Index Analysis

The overall performance index (OPI) is an optimized performance measure of the combined cycle power plant that takes into consideration all the performance indicators that are important for the user. The importance and the weight of the performance indicators for the combined cycle power plant depend on the user demand, type of application, and the local condition in which the plant is installed. To evaluate the overall performance index (OPI) a performance matrix is constructed to define the weight of each index depending on its importance and how it will effects the overall performance

index (OPI) [4]. The procedure of constructing the performance matrix is described in the following section.

3.2.5 Developing a Performance Matrix

Developing a performance matrix is a process that begins by specifying goals and ranges of performance for several indicators that are related to the performance of the system under consideration. The performance indicators that are used for combined cycle power plant performance assessment are Energy Efficiency (ENE), Exergy Efficiency (EXE), Levelized Cost of Electricity (COE) and Total Investment (TI) as shown in Table (1).

Table 1: Performance matrix

	Performance Level										
	Stretch Goal		Goal				Baseline				
Performance Indicator (PI)	1	2	3	4	5	6	7	8	9	10	Weight Case#3
ENE (%)											
EXE (%)											
COE ($/kWh)											
TI (MM$)											

The relative importance and the impact on the overall performance index (OPI) of each performance indicator have to be determined. The total weight for the performance indicators must add up to 100%. As a case study in the present work, 20%, 20%, 30% and 30% have been given to ENE, EXE, COE and TI respectively, as shown in Table (2).

Table 2: Performance matrix with weights

	Performance Level										
	Stretch Goal		Goal				Baseline				
Performance Indicator (PI)	1	2	3	4	5	6	7	8	9	10	Weight Case#3
ENE (%)											20
EXE (%)											20
COE ($/kWh)											30
TI (MM$)											30

The baseline and the goal levels values for each performance indicator are specified. In addition, a “stretch goal” for each performance indicator is determined. The stretch goal reflects extraordinary performance of the hybrid system (Table (3)).

Table 3: Performance matrix with baselines and goals

	Performance Level										
	Stretch Goal		Goal				Baseline				
Performance Indicator (PI)	1	2	3	4	5	6	7	8	9	10	Weight Case#3
ENE (%)			52				44				20
EXE (%)			50				42				20
COE ($/kWh)			0.06				0.07				30
TI (MM$)			80				120				30

After determining the baseline, goal and stretch goal for each performance indicator, the intermediate goals are established by simply interpolating using simple numeric increments in between. Finally, appropriate values are specified for the performance levels worse than the baseline performance as shown in Table (4).

Table 4: Performance matrix with completed performance levels

	Performance Level										
	Stretch Goal		Goal				Baseline				
Performance Indicator (PI)	1	2	3	4	5	6	7	8	9	10	Weight Case#3
ENE (%)	56	54	52	50	48	46	44	42	40	38	20
EXE (%)	54	52	50	48	46	44	42	40	38	36	20
COE ($/kWh)	0.04	0.05	0.06	0.0625	0.065	0.0675	0.07	0.0734	0.0767	0.08	30
TI (MM$)	40	60	80	90	100	110	120	145	170	195	30

Once the performance matrix is completed, it can be used to evaluate the performance of the combined cycle including the selected performance indicators, performance levels and the assigned weights using the developed mathematical model and numerical code.

3.2.6 Calculating the Overall Performance Index

The variation of the (OPI) will give an indication how the combined cycle power generation system is performing under the real circumstances and randomness on the weather conditions such as the ambient temperature and the humidity. Through this procedure, the selection of the right configuration (size, i.e. the pressure ratio) of the combined cycle power plant can be determined to yield the maximum (OPI) under the

given environmental and weather conditions. The performance indicators considered to maximize the overall performance index in this study include the energy efficiency (ENE [%]), exergy efficiency (EXE [%]), levelized cost of electricity (COE [$/kWh]), and the total investment (TI [MM$]). Depending on their importance for the user, appropriate weight factors are selected for these performance indicators in the analysis. The complete performance matrix with level score raw is shown in Table (5).

After calculating the current values of each performance indicator for any configuration of the system parameters such as pressure ratio of the gas turbine, ambient temperature and relative humidity, a scoring system has to be constructed to evaluate the overall performance index (OPI). The level score is a specific percent that reflects the satisfactory level multiplied by the weight of that indicator. 100% is specified to the goal performance level (level 3). If the value of performance indicators is less than the goal and toward the stretch goal ,extraordinary performance of the system is achieved and more satisfactory level is specified up-to 120% at level 1 where we consider ENE = 56%, EXE = 54%, COE = 0.04 $/kWh and TI = 40 MM$. If the current value of performance indicators is more than the goal, less satisfactory percent is specified until it becomes 80% at the baseline level (level 7) and it keep decreasing until it reaches zero at level 10. This does mean that any combination of the pressure ratio, ambient temperature and relative humidity that leads to ENE $\geq$ 38 %, EXE $\geq$ 36 %, COE $\geq$ 0.08 $/kWh and TI $\geq$ 195 MM$ is rejected. The complete performance matrix with level score raw is shown in Table (5).

Table 5: Complete performance matrix with level score raw

	Performance Level										
	Stretch Goal		Goal				Baseline				
Performance Indicator (PI)	1	2	3	4	5	6	7	8	9	10	Weight Case#3
ENE (%)	56	54	52	50	48	46	44	42	40	38	20
EXE (%)	54	52	50	48	46	44	42	40	38	36	20
COE ($/kWh)	0.04	0.05	0.06	0.0625	0.065	0.0675	0.07	0.0734	0.0767	0.08	30
TI (MM$)	40	60	80	90	100	110	120	145	170	195	30
LEVEL SCORE	1.2×Wt	1.1×Wt	1×Wt	0.95×Wt	0.9×Wt	0.85×Wt	0.8×Wt	0.53×Wt	0.26×Wt	0×Wt	

Using the level score raw may leads to have the same score for such performance index if its value falls between two levels. For example, if ENE value is 52.8 %, 52.5 % or 53 %, the corresponding level is always level 3 and the score is 100% multiplied by the weight of ENE, which is 20 %. Therefore, the level score is the same, which does not reflect that there are differences in the ENE values. To avoid this behavior during the simulation, a curve fitting technique is adopted to obtain a mathematical expression for the level score raw data, (Table (5)) as a function of the level using third order polynomial with R^2 = 0.9998 accuracy as shown in Figure (2). Utilizing the score function and for any value of such indicator that falls between two levels, the level is interpolated and the corresponding score is evaluated, utilizing the mathematical expression of the score function. This procedure is repeated for all performance indicators (ENE, EXE, COE and

TI). Then, the overall performance index (OPI) is the summation of all performance indicator scores. Figure (3) shows the flow chart of the steps of developing the performance matrix.

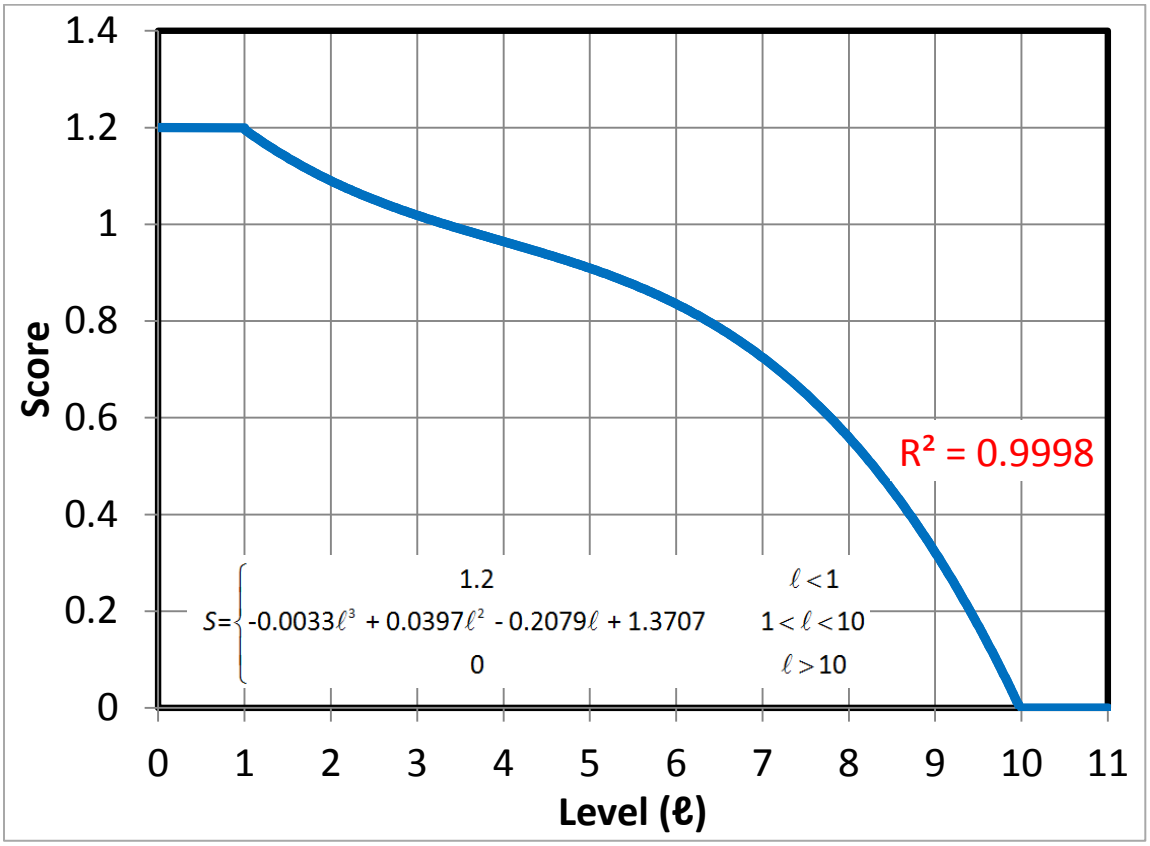

Figure 2: Score function as a third order polynomial curve fitting of the level score

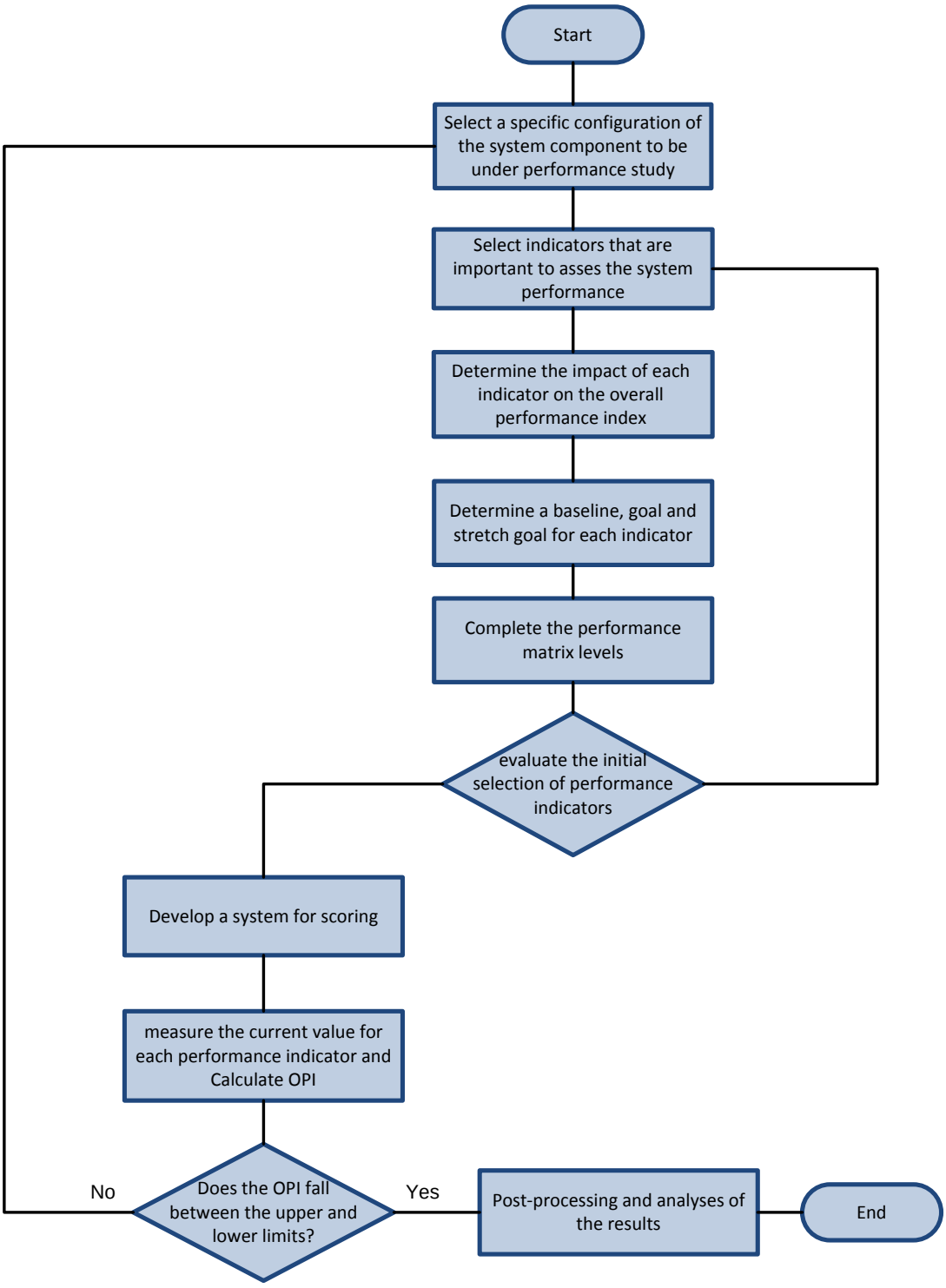

Figure 3: Flow chart of developing the performance matrix

3.3 Renewable Energy Systems for Power Generation and Hydrogen Production in Kingdom of Saudi Arabia

In this part of the dissertation, assessments of the potentials of solar and wind renewable energy recourses for electricity and hydrogen production will be presented. Mathematical models related to systems components are given in the following subsections.

3.3.1 PV Module

The total output power of the photovoltaic array is proportional to the current, voltage and the number of the photovoltaic modules and can be determined from:

$$P_{PV} = n_{pv} V_{PV} \; i_{PV} \tag{3.12}$$

where:

n_{pv} is the number of the photovoltaic modules.

V_{PV} is the voltage.

i_{PV} is the current of the photovoltaic module.

The optimum operating point current and voltage of the PV module are given, respectively, as [77]:

$$i_{PV} = i_{SC}\left(1 - C_1\left[\exp\left(\frac{V_{PV} - \Delta V}{C_2 V_{OC}}\right) - 1\right]\right) + \Delta i \tag{3.13}$$

and [77]:

$$V_{PV} = V_{mp}\left[1 + 0.0539\log\left(\frac{I_T}{I_{st}}\right)\right] + \beta_o \Delta T \tag{3.14}$$

where

$$C_1 = \left(1 - \frac{i_{mp}}{i_{SC}}\right)\exp\left(-\frac{V_{mp}}{C_2 V_{OC}}\right) \tag{3.15}$$

$$C_2 = \frac{V_{mp}/(V_{OC} - 1)}{\ln\left(1 - i_{mp}/i_{SC}\right)} \tag{3.16}$$

$$\Delta V = V_{PV} - V_{mp} \tag{3.17}$$

$$\Delta i = \alpha_o \left(\frac{I_T}{I_{st}} \right) \Delta T + \left(\frac{I_T}{I_{st}} - 1 \right) i_{SC} \tag{3.18}$$

$$\Delta T = T_{cell} - T_{st} \tag{3.19}$$

$$T_{cell} = T_A + 0.02 I_T \tag{3.20}$$

in which

i_{sc} is the short-circuit current.

V_{mp} is the maximum-power voltage.

(V_{oc}) is the open-circuit voltage.

i_{mp} is the maximum-power current.

α_o is the current temperature coefficient.

β_o is the voltage temperature coefficient of the module.

I_T is the total solar radiation on tilted panel.

I_{st} is the standard solar radiation (1000 W/m^2).

$T_{A.}$ is the ambient temperature.

The standard ambient temperature is T_{st} = 25˚C. The manufacturer specifications of the selected PV module are listed in Table (6).

Table 6: Technical specifications of the photovoltaic module [78]

Model	P_{mp}(W)	$V_{nominal}$ (V)	V_{mp} (V)	I_{mp}(A)	V_{oc}(V)	I_{sc}(A)	A (m^2)	Price($)
BP350	50	12	17.5	2.9	21.8	3.17	0.451	350

3.3.2 Wind Turbine

The generated power by wind turbine is calculated utilizing the manufacturer characteristic curve and the wind speed [24] as:

$$\frac{v}{v_o} = \left(\frac{z}{z_o} \right)^{\gamma} \tag{3.21}$$

where

v is the wind speed at the hub height z.

v_o is the measured wind speed at the reference height (z_o = 10 m).

γ is the ground surface friction coefficient.

A typical value of (1/7) is used for the ground surface friction coefficient [24].

The wind power generator output can be expressed by adopting curve fitting technique of its characteristic curve as:

$$P_w(v)=\begin{cases} 0 & for \rightarrow \quad v < v_c \\ a_1 v^n \ldots \; b_1 v^2 + c_1 v + d_1 & for \rightarrow \; v_c \le v < v_1 \\ a_2 v^n \ldots \; b_2 v^2 + c_2 v + d_2 & for \rightarrow \; v_1 \le v < v_2 \\ a_3 v^n \ldots \; b_3 v^2 + c_3 v + d_3 & for \rightarrow \; v_2 \le v < v_f \\ 0 & for \rightarrow \quad v > v_f \end{cases} \tag{3.22}$$

where

$P_w(v)$ is the output power of wind turbine.

v_c is the cut-in speed of the wind turbine.

v_f is the cut-off speed of the wind turbine.

v_1 and v_2 are the intermediate wind speed levels.

Table (7) lists the specifications of the selected wind turbine whereas Figure (4) shows the turbine characteristic curve.

Table 7: Technical specifications of the selected wind turbine [79]

Model	Power rated (W)	$V_{nominal}$ (V)	V_{ci} (m/s)	V_r (m/s)	Price($)
BWCXL 1000	1000	24	2.5	11	2500

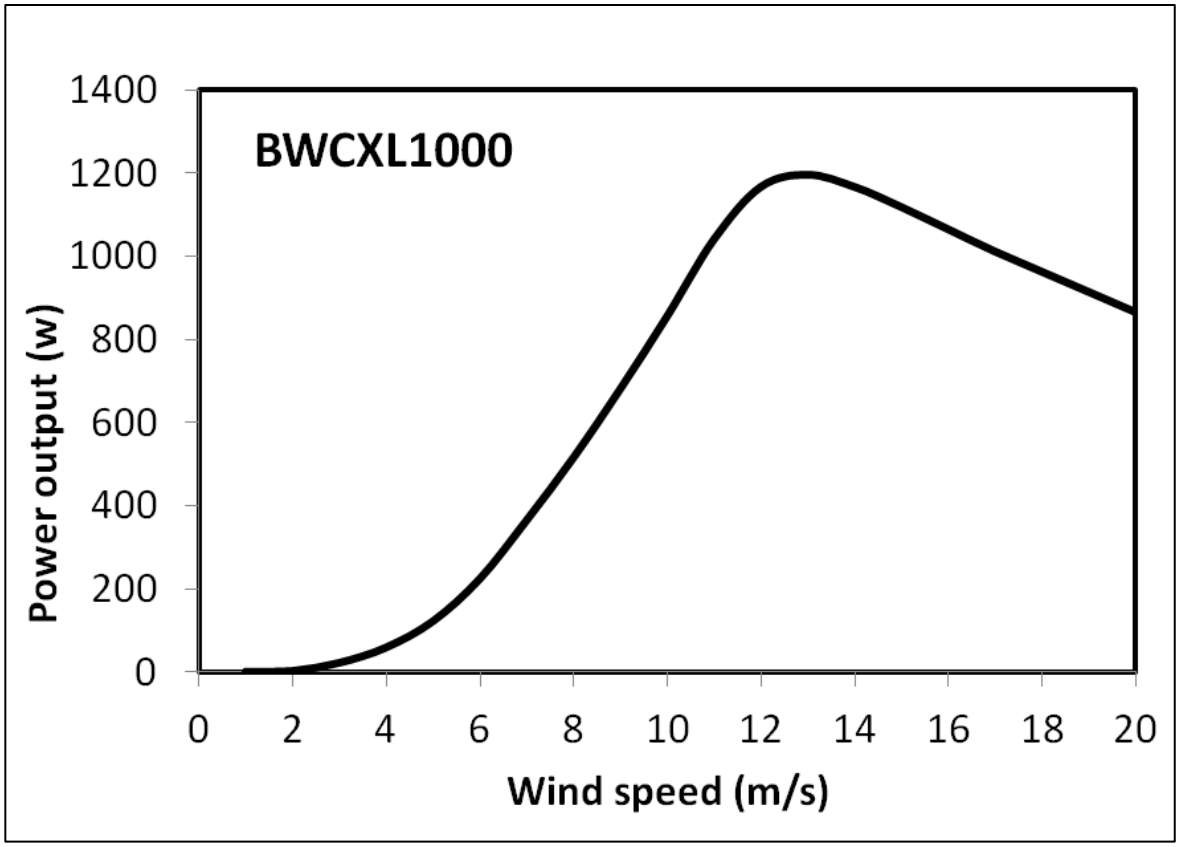

Figure 4: Characteristics curve of the selected wind turbine [80]

3.3.3 Battery Bank

During the charging mode, the state of charge capacity of the battery as function of time is [24]:

$$C_B(t) = C_B(t-1).(1-\sigma) + \left(P_T(t) - \frac{P_L(t)}{\eta_{conv}} \right) \eta_{Batt} \qquad (3.23)$$

where

P_T is the system total output power.

P_L is the load demand at the corresponding hour.

During the discharge mode, the capacity of battery bank at the time (t) can be written as:

$$C_B(t) = C_B(t-1)(1-\sigma) + \left(\frac{P_L(t)}{\eta_{conv}} - P_T(t) \right) \tag{3.24}$$

The state of charge of the battery bank must be maintained between the limits.

$$C_{B\min} \le C_B(t) \le C_{B\max} \tag{3.25}$$

where

$C_{B\max}$ is the nominal capacity of battery bank, C_{Batt} .

$$C_{B\max} = C_{Batt} \tag{3.26}$$

and

$C_{B\min}$ is determined by the maximum depth of discharge (DOD) as:

$$C_{B\min} = (1 - DOD)C_{Batt} \tag{3.27}$$

where a value of 80% is normally used for DOD. The specifications of the battery are listed in Table (8).

Table 8: Technical specifications of the battery [81]

Model	Nominal capacity (Ah)	Voltage (V)	Minimum charge (%)	Price ($)
Concorde (PVX-2120L)	253	12	20	465

3.3.4 Other Components

The load should be covered by the by the renewable energy system power output. In case that the generated power is more than the load demand, the surplus energy can be used to produce hydrogen by the electrolyzer through an electrolysis process of the water. The

electrolyzer is a container which is filled by the electrolyte liquid in which two electrodes is used to carry out the electrolysis process. The initial capital cost and replacement cost were 2000 $/kW. The life time is 15 years and no operating and maintenance costs considered for the electrolyzer within the project lifetime (25 years). Proton Exchange membrane (PEM) fuel cell is used to convert the chemical energy to electricity through electrochemical reaction. It receives the external supply of fuel such as hydrogen and converts it to electricity by an oxidation process and the products are electricity, heat and water with no pollutants. Different sizes of the fuel cell are considered in the considered systems. The summation of the initial investment and replacement costs is 3000 $/kW and the operating and maintenance cost is 0.1 $/h and the lifetime of the fuel cell is 40000 h. When the system output power is more than the load requirements, the surplus electricity will be used to generate hydrogen using the electrolyzer through electrolysis process. The generated hydrogen is stored in a 30 bar hydrogen tank. This storage system can be used in place of the battery energy storage system. The initial capital cost and the replacement cost of the hydrogen tank are 1500 $/kg with no operating and maintenance costs considered in the project lifetime (25 years). The converter capital and replacement costs are 1000 $/kW and its life time is 15 years.

3.3.5 Optimization

The simulation and the optimization of the off-grid renewable generation systems are achieved by HOMER Software (Hybrid Optimization of Multiple Energy Resources) [6] . For any size of the storage system, the size of the PV array or the number of the wind

turbines are increased until there is no shortage of the power supply to the load is realized. Different sizes of the systems components lead to thousands of configurations.

In the optimization technique of HOMER, the optimum configuration that leads to minimizing the cost while meeting the designer-specified constrains, is considered [82]. Optimal sizing of the system is achieved by the minimization of the loss of power supply probability (LPSP) and the cost of energy (COE).

LPSP is defined as the ratio of summation of all hourly loss of power supply values (LPS), over the total required load.

$$LPSP = \frac{\sum_{t=1}^{8760} LPS(t)}{\sum_{t=1}^{8760} P_L(t)\,\Delta t} \tag{3.28}$$

where LPS(t) is:

$$LPS(t) = P_L(t)\Delta t - (P_T \Delta t + C_B(t-1) - C_{B\min})\eta_{conv} \tag{3.29}$$

where

Δt is the time step used for the calculations (that is 1 h).

If LPSP = 0, the load requirements is always met by renewable energy whereas if LPSP = 1, the system of the renewable energy can never meet the load requirements. In second case, the battery is at the minimum allowable storage capacity.

The renewable fraction (Renewable Contribution) is:

$$RF = 1 - LPSP \tag{3.30}$$

The net present value of a system is the summation of initial, installing and operating the system over its lifetime.

The levelized cost of energy is defined as [24]:

$$COE = \frac{NPC \times CRF}{\sum_{t=1}^{8760} P_L(t)\,\Delta t} \tag{3.31}$$

where

NPC is the net total present value of all system components.

CRF is the capital recovery factor:

$$CRF = \frac{i(1+i)^n}{(1+i)^n - 1} \tag{3.32}$$

$$NPC = C_{PV} + C_{Wind} + C_{Batt} + C_{Electrolyzer} + C_{FC} + C_{H_2 \text{ tank}} + C_{conv} \tag{3.33}$$

where

i is the real interest rate which are taken in this study as 6%.

n is the project life time in years (25 years).

C_{PV} is the initial and maintenance costs of the PV array.

C_{wind} is the initial and maintenance costs of the wind turbines.

C_{Batt} is the initial and maintenance costs of the battery bank.

$C_{Electrolyzer}$ is the initial and maintenance costs of the electrolyzer.

C_{FC} is the initial and maintenance costs of the fuel cell.

C_{H2tank} is the capital and maintenance costs of the hydrogen tank.

C_{Conv} is capital and maintenance costs of the converter

The combination of the system components that leads to minimizing COE is considered as the optimum configuration.

3.4 Thermal and Electrical Characteristics of Semi-Conductive Nanofluid

Although nanofluids contain low volume fraction of the conducting particles, thermal properties enhancement of the carrier fluid is substantial [39-42, 83]. Incorporating mass based analysis for effective thermal properties prediction of the nanofluids leads erroneous findings. This is due to the distribution and connectivity of the nanoparticles in the carrier fluid. Therefore, investigation of the thermal property enhancement of the nanofluid becomes essential for appropriate assessment of the thermal system performance. Consequently, in the present study, the nanofluid which is prepared by uniform dispersion of multi-wall carbon nanotube (MWCNT) with 1% concentration into water is considered to examine thermal and electrical properties of the mixture. Experiments are carried out to obtain the thermal and electrical characteristics of the nanofluid prepared. Specific heat capacity (C_p) is determined from the data obtained from differential scanning calorimeter and conductance meter is used to measure the electrical conductivity of the nanofluid. In addition, numerical simulations are carried out incorporating COMSOL Multiphysics Software [3]. During the simulations, thermal and electrical properties of the MWCNT are assumed to be constant because of the temperature range considered in the simulations. However, the properties of water are taken as temperature dependent in the simulations. The predictions are compared with those obtained from the mass based analysis and the experimental data. Table (9) gives

the data used for carbon nanotubes in the simulations whereas the properties of the water are considered as temperature dependant functions.

Table 9: Properties of multi-walled carbon nanotube MWCNT used in the simulations

Density (ρ) [84-86]	270 kg/m^3
Thermal Conductivity (k)[87]	3000 W/(mK)
Heat Capacity at Constant Pressure (C_p) [88]	500 J/(kgK)
Electrical Conductivity (σ) [86]	100 S/cm

Numerical approach is implemented to characterize the thermal and electrical properties of water-CNT mixture. Since the concentration of CNT in the carrier fluid 9water) is 1%, a single fluid model is considered. The governing equations with the appropriate boundary conditions are solved to determine the effective properties of the nanofluid. The time dependent energy equation can be written as:

$$\rho c_p \frac{\partial T}{\partial t} + \rho c_p V \cdot \nabla T = \nabla \cdot \left(k \nabla T \right) \tag{3.34}$$

where;

ρ is the density.

c_p is the specific heat capacity.

k is the thermal conductivity.

To determine the thermal conductivity of the water-CNT mixture, numerical simulations are carried out by specifying temperature boundary conditions on the edges at x = 0 m and x = L m of experimental micro images that represent the real distribution of the CNT in the water at different concentration ratios. In the case of mass based analysis for the thermal properties, the followings are introduced.

3.4.1 Effective Density

The effective density of the homogeneous bulk liquid (mixture of water and CNT) can be determined using mass balance as [70]:

$$\rho_{eff} = c\,\rho_{CNT} + (1-c)\,\rho_W \tag{3.35}$$

where

c is the volume concentration of carbon nanotubes in water.

ρ_{eff} is the effective density of the nano-fluid.

Subscripts: *CNT* is the carbon nanotubes and *W* is the water.

3.4.2 Effective Specific Heat Capacity

The specific heat of the homogeneous mixture of nanofluid is calculated via energy balance as [89]:

$$c_{p\_eff} = \frac{c\left(\rho c_p\right)_{CNT} + (1-c)\left(\rho c_p\right)_W}{\rho_{eff}} \tag{3.36}$$

where

C_{p_eff} is the specific heat of the nano-fluid mixture.

3.4.3 Effective Thermal Conductivity

Effective thermal conductivity of nano-fluid is determined using the Maxwell model [89]; therefore, thermal conductivity of the homogeneous mixture can be written as:

$$k_{eff} = k_W \frac{2 + k_{CNT}/k_W + 2c\left(k_{CNT}/k_W - 1\right)}{2 + k_{CNT}/k_W - c\left(k_{CNT}/k_W - 1\right)} \tag{3.37}$$

where

k_{eff} is the effective thermal conductivity of the nano-fluid.

3.4.4 Effective Electrical Conductivity

The same procedure of the thermal conductivity can be applied to determine the electrical conductivity of water-CNT mixture. In this case, a gradient of electrical potential is applied at x=0 m and x=L m and the current density and the electrical field are monitored. Thus, the electrical resistivity can be formulated as:

$$\xi = \frac{E}{J} \tag{3.38}$$

where

ξ is the electrical resistivity.

E is the electrical potential.

J is the current density.

So, the effective electrical conductivity of the nanofluid can be written as:

$$\sigma = \frac{1}{\xi} \tag{3.39}$$

CHAPTER 4

RESULTS AND DISCUSSION

4.1 Introduction

This chapter presents the results and discussion of the cases relevant to the thermal system analysis and surface characteristics that are considered in this dissertation. The findings and discussions are demonstrated here under appropriate subsections:

- Overall Performance Assessment of a Combined Cycle Power Plant: An Exergo-Economic Analysis.

- Techno-Economic Analysis and Optimization of Different Renewable Energy Systems for Power Generation and Hydrogen Production in Dhahran Area, Kingdom of Saudi Arabia.
- Generalizing the Renewable Energy Systems for Power Generation and Hydrogen Production at Several Areas in the Kingdom of Saudi Arabia.
- Thermal and Electrical Characteristics of Semi-Conductive Nanofluid.
- Marangoni-Convection Flow and Heat Transfer Characteristics of Water-CNT Nanofluid.

Each of the above cases is discussed in detail in the following sections.

4.2 Overall Performance Assessment of a Combined Cycle Power Plant: An Exergo-Economic Analysis

A performance optimization for a combined cycle power plant is performed using exergo-economic analysis and overall performance index procedure. Performance analysis is carried out considering the meteorological conditions at a location on the shoreline of the Arabian Gulf in northeastern Saudi Arabia, near Dhahran (26°N, 50°E). This area is considered to be semi- desert, due to its extremely low precipitation rate, high temperatures, and frequent windstorms. The performance of the power plant is influenced by the environmental conditions such as temperature and humidity. The surface air temperature and humidity data that were collected for a period of 20 years from 1984-2004, were used in the simulations. Figure (5) shows the frequency distribution of daily average ambient temperature and relative humidity for Dhahran. The

average ambient temperature varies from 20 to 40^{o}C throughout the year with a yearly average of 31^{o}C. The average relative humidity in Dhahran is 49%.

A base case is selected in order to study the performance of the combined cycle power plant in which GE 5371PA model gas turbine is selected from the GT PRO library. The technical specifications and the price of the gas turbine are given in Table (10). The pressure ratio r_p of this gas turbine is 10. The effects of the ambient temperature and the humidity ratio on the energy efficiency, exergy efficiency and the cost of electricity for the selected base case model is are given in Figure (6). Increase in the ambient temperature decreases both the energy efficiency and exergy efficiency. On the contrary, the cost of electricity increases as the ambient temperature increases. The reduction in the energy efficiency and the exergy efficiency is more pronounced as the ambient temperature increases above 40^{o}C, as can be seen from Figures (7) and (8), respectively. The decrease in the exergy efficiency, given in Equation (3.10), is due to the relative increase in the irreversibilities and decrease in the net output power in the power plant as both the ambient temperature and the relative humidity increase. Figure (6) shows also that increase in the relative humidity results in the decrease of both the energy efficiency and exergy efficiency to a lesser extend as compared with the ambient temperature. Thus, the effect of the relative humidity on the cost of electricity is not significant. The cost of energy varies between 0.071 – 0.075 $/kWh within the ranges of ambient temperature and the humidity ratios (Figure (9)). Since the cost of electricity, as given in Equation (3.11), is inversely proportional to the total energy output of the power plant, the significant decrease in the net output power as a result of increase in the ambient temperature is responsible for the increase in the cost of electricity as shown in Figure

(9). On the other hand, Figure (10) shows a comparison of energy and exergy efficiencies and their variation with the ambient temperature. As mentioned above, both of the energy and exergy efficiencies decrease as the ambient temperature increases, however, the exergy efficiency remains lower than the energy efficiency in all the range of ambient temperature variation. Since the exergy efficiency considers also the quality of energy, it represents a more realistic measure of the combined cycle power plant performance.

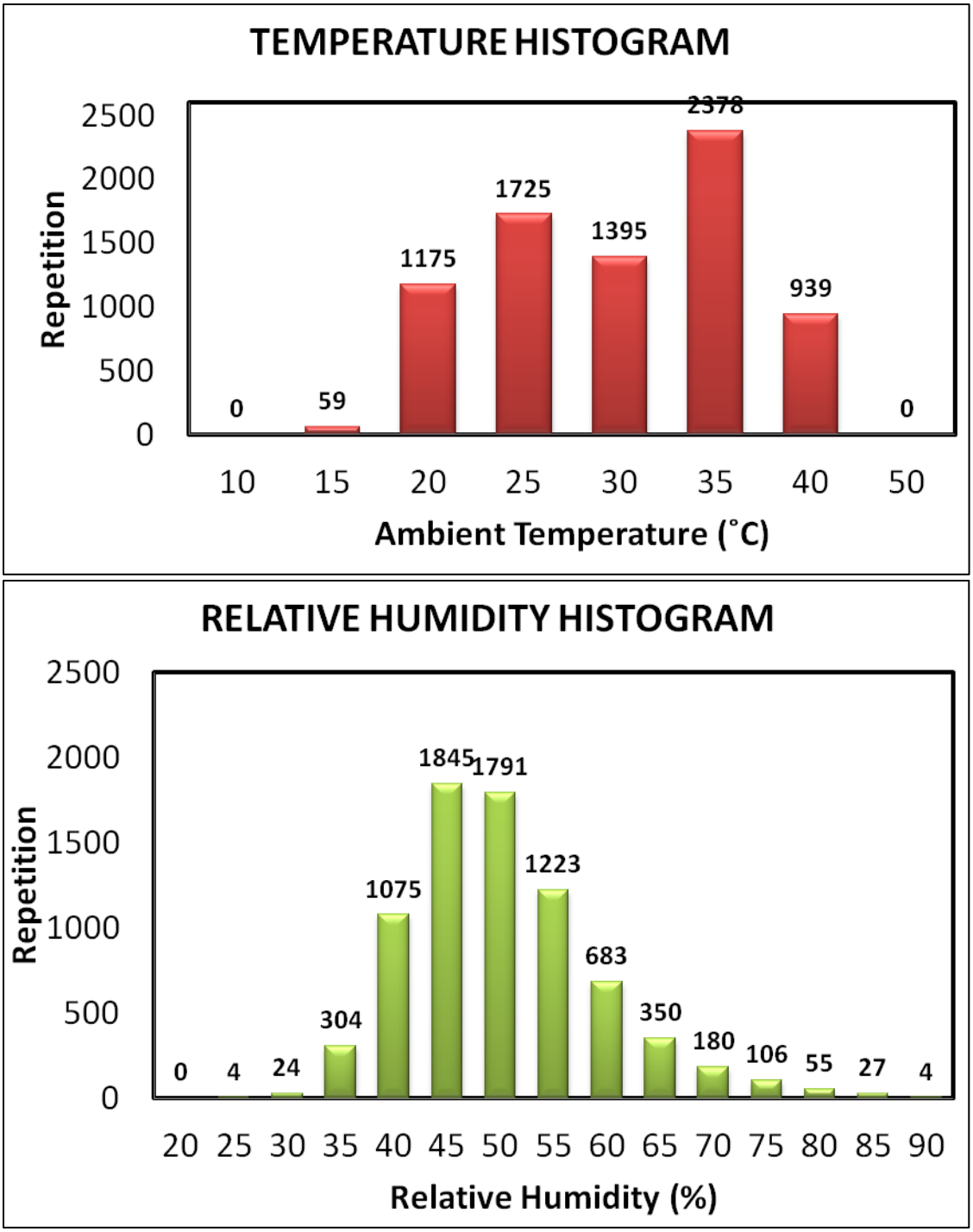

Figure 5: Frequency distribution of daily average ambient temperature and relative humidity during 1984-2004 for Dhahran city in the kingdom of Saudi Arabia.

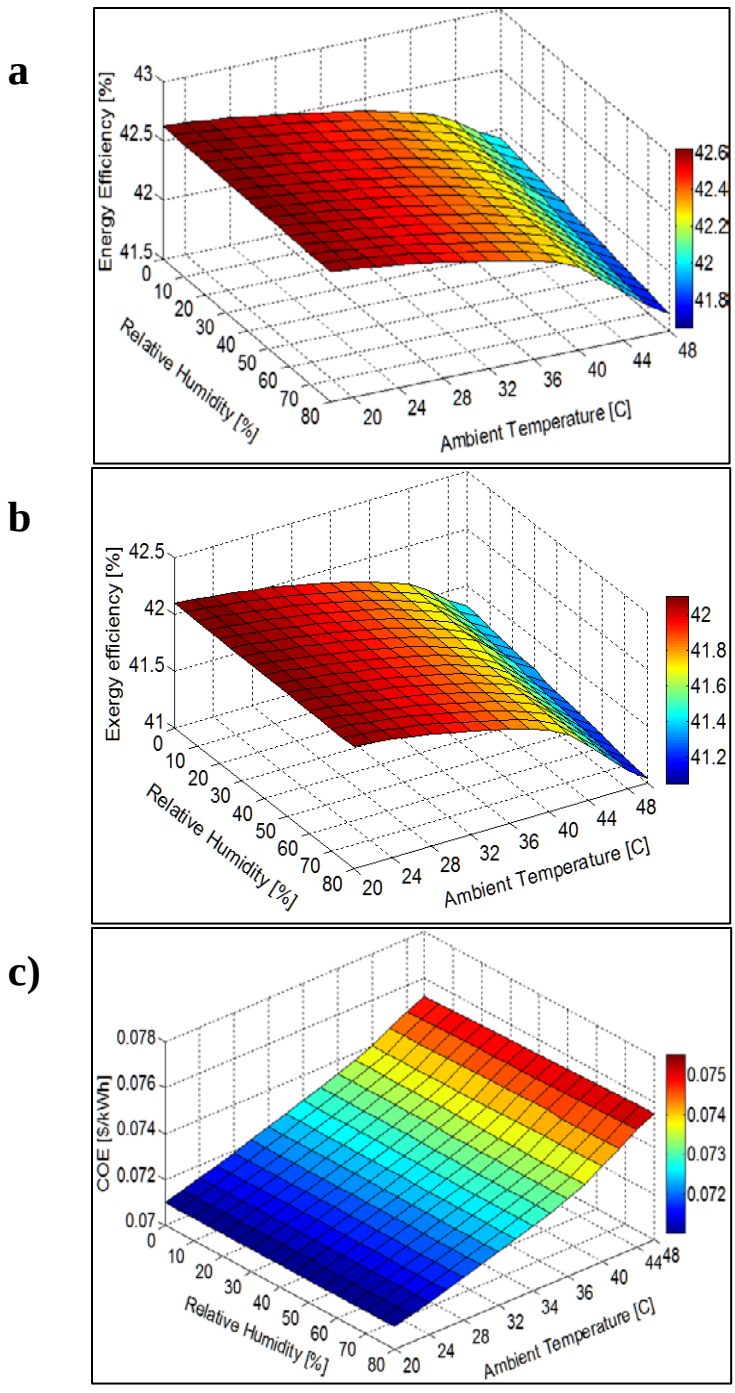

Figure 6: Surface plots efficiencies and levelized cost of electricity: a) energy efficiency, b) exergy efficiency and c) levelized cost of electricity variations with the ambient temperature and relative humidity. The considered pressure ratio of the gas turbine r_p = 10.

Table 10: Technical specifications of the gas turbine selected as the base case model [5]

ID	Manufacturer & Model	Pressure Ratio	Turbine Inlet Temperature [C]	Turbine Exit Temperature [C]	Price [Million $]
1	GE 5371PA	10	963	485	10.8

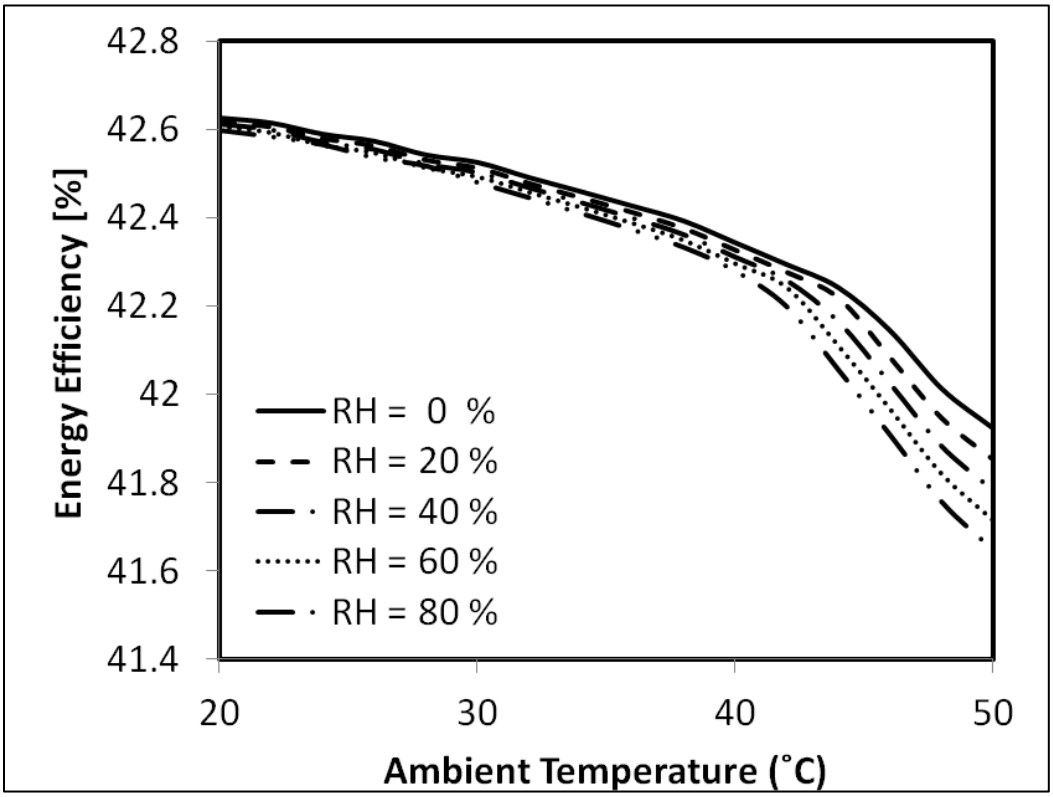

Figure 7: Effect of the ambient temperature and relative humidity on the first law efficiency. RH is the relative humidity and the considered pressure ratio of the gas turbine $r_p = 10$.

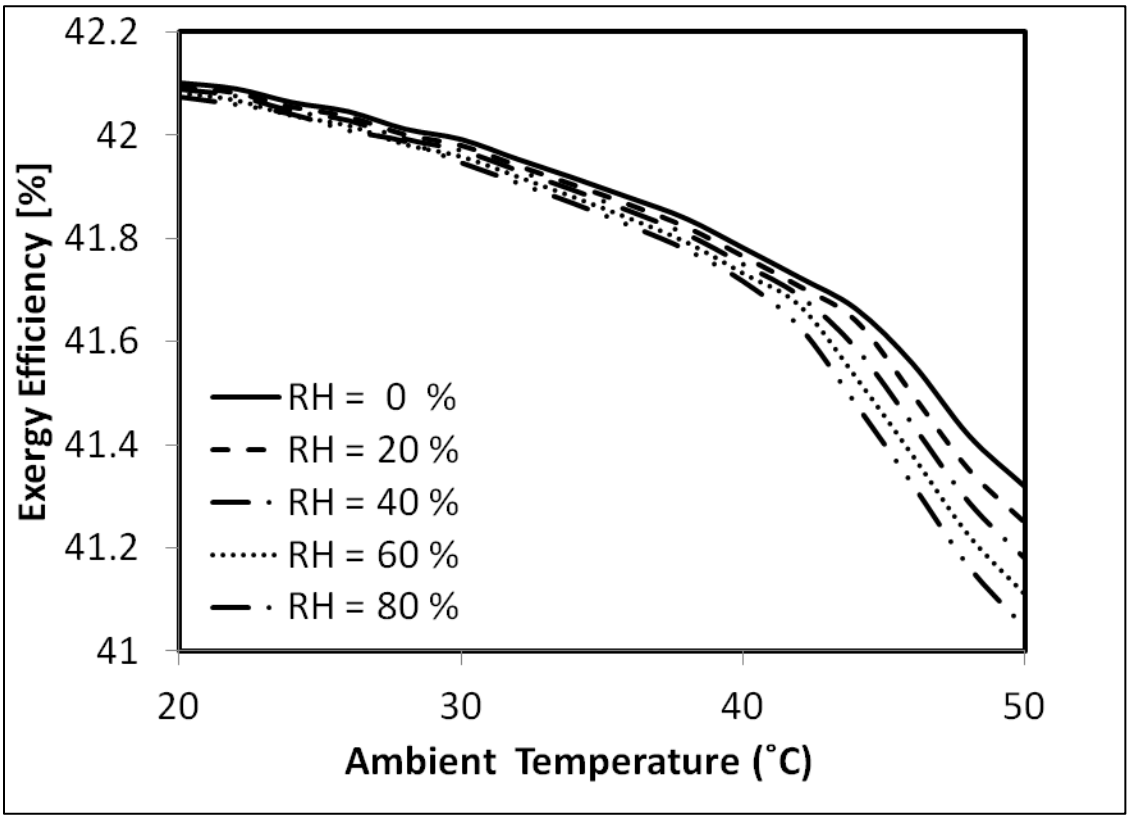

Figure 8: Effect of the ambient temperature and relative humidity on the second law efficiency. RH is the relative humidity and the considered pressure ratio of the gas turbine r_p = 10.

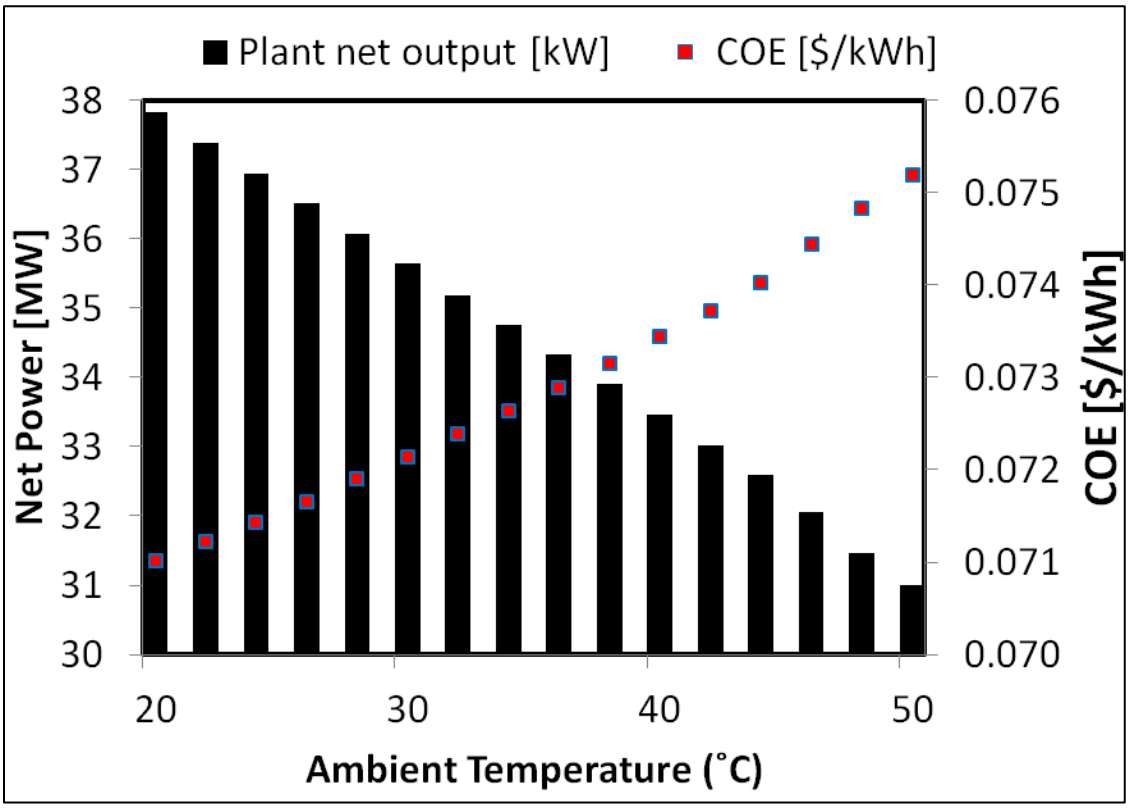

Figure 9: Effect of the ambient temperature on the plant net output power and levelized cost of electricity. The relative humidity RH = 0 % and the considered pressure ratio of the gas turbine r_p = 10.

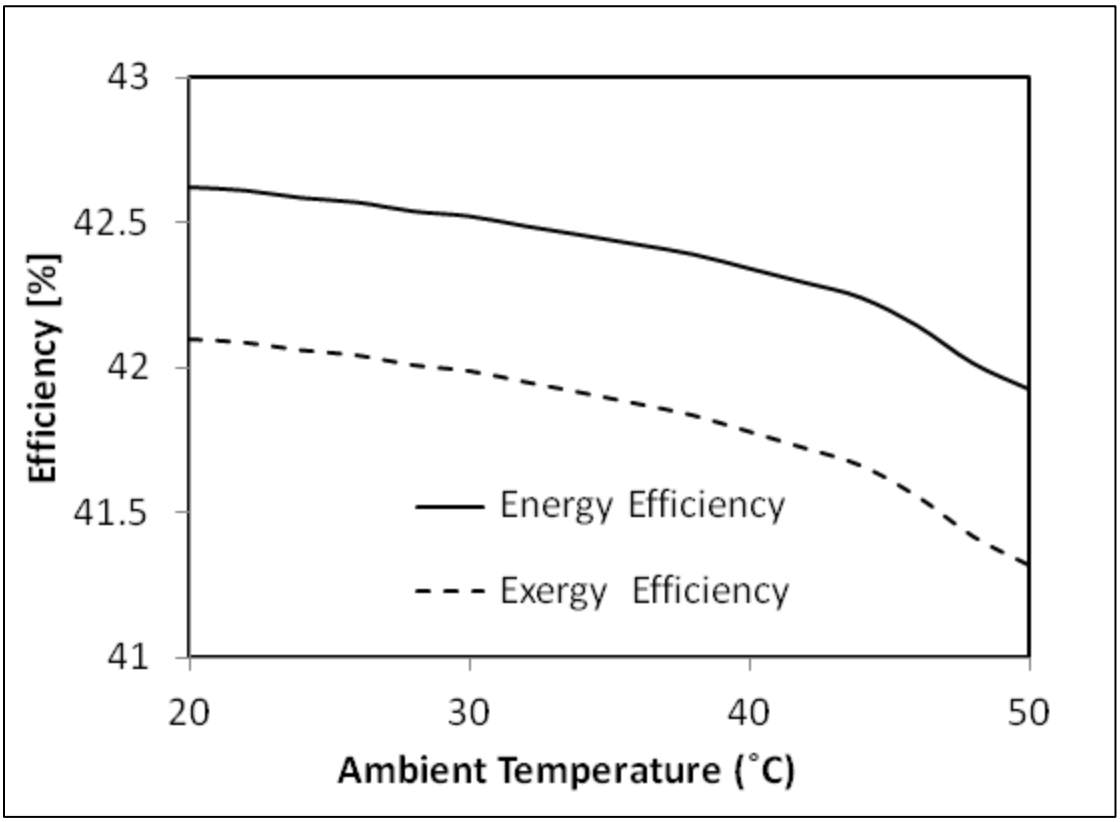

Figure 10: Effect of the ambient temperature on the first and second low efficiency. The relative humidity RH = 0 % and the considered pressure ratio of the gas turbine r_p = 10.

After analyzing the performance of GE 5371PA model gas turbine with the pressure ratio of 10, the same analysis is repeated for five other gas turbine models of different size (i.e. with different pressure ratios) as given in Table (11). The purpose of this analysis is to identify the most suitable model to the site considered (Dhahran) with the highest overall performance index taking into account all the performance indicators such as energy efficiency (ENE [%]), exergy efficiency (EXE [%]), levelized cost of electricity (COE [$/kWh]), and the total investment (TI [MM$]). The selected gas turbine models have pressure ratios ranging from 8 to 16.2. The technical specifications and the price of each of the models are listed in Table 11.

Table 11: The specifications of the selected gas turbine models [5]

ID	Manufacturer & Model	Pressure Ratio	Turbine Inlet Temperature [C]	Turbine Exit Temperature [C]	Price [Million $]
198	GE 5251M	8	927	509	9.1
1	GE 5371PA	10	963	485	10.8
103	GE 6551B	11.9	1104	539	15.3
85	GE 7161EC	14.2	1204	549	32.4
427	GE 7F 3-series	16	1343	602	38.5
519	GE GT-7F.04	18.2	1343	602	38.2

Figure (11) shows the variation of the energy and exergy efficiencies for varying pressure ratio. As the pressure ratio (i.e. as the size of the gas turbine) increases both the energy and exergy efficiencies increase. The increasing trend for both of the efficiencies is the same; however, the exergy efficiency remains lower than the energy efficiency for all cases as shown in Figure (11). The energy efficiency varies from 40% to 54% as the pressure ratio is increased from 8 to 18.2. This is due to the increase in the power produced as the size of the gas turbine is increased.

The levelized cost of electricity and the total cost of investment for various pressure ratios are given in Figure (12). As the size of the gas turbine is increased, the total cost of investment increases; however, the levelized cost of electricity decreases. This is due the fact that as the size of the gas turbine increases the net power output increases as shown in Figure (13). The levelized cost of electricity decreases to 0.05 $/kWh for the large size gas turbine with pressure ratio of 18.2. Figure (14) shows the effect of both the ambient temperature and the pressure ratio on the energy efficiency, exergy efficiency and levelized cost of electricity. As the ambient temperature increases both the energy and exergy efficiencies decrease, but the levelized cost of electricity increases. However, the effect of the pressure ratio on efficiencies and the levelized cost of energy is much larger that of the ambient temperature.

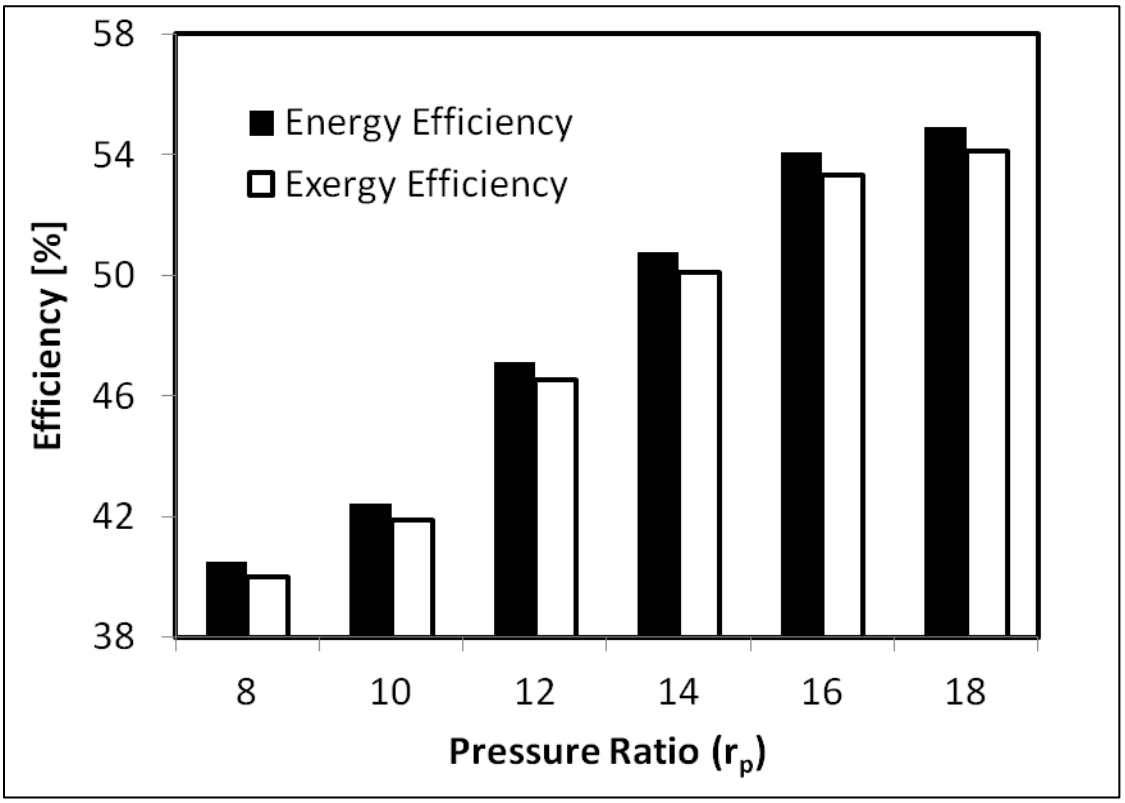

Figure 11: Effect of the pressure ratio of the gas turbine on energy and exergy efficiencies [ambient temperature T = 35˚C and relative humidity RH = 45 %].

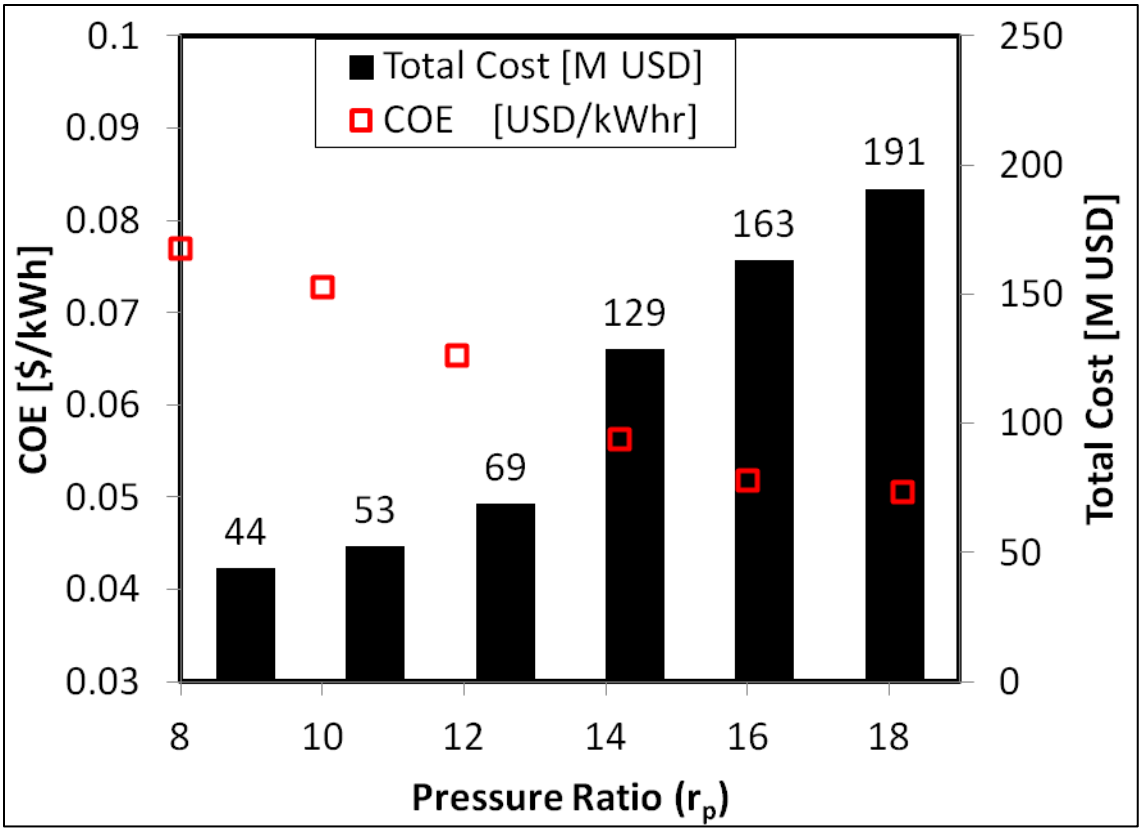

Figure 12: The total cost of the plant and the levelized cost of electricity (COE) for different types of the gas turbines [ambient temperature T = 35˚C and relative humidity RH = 45 %].

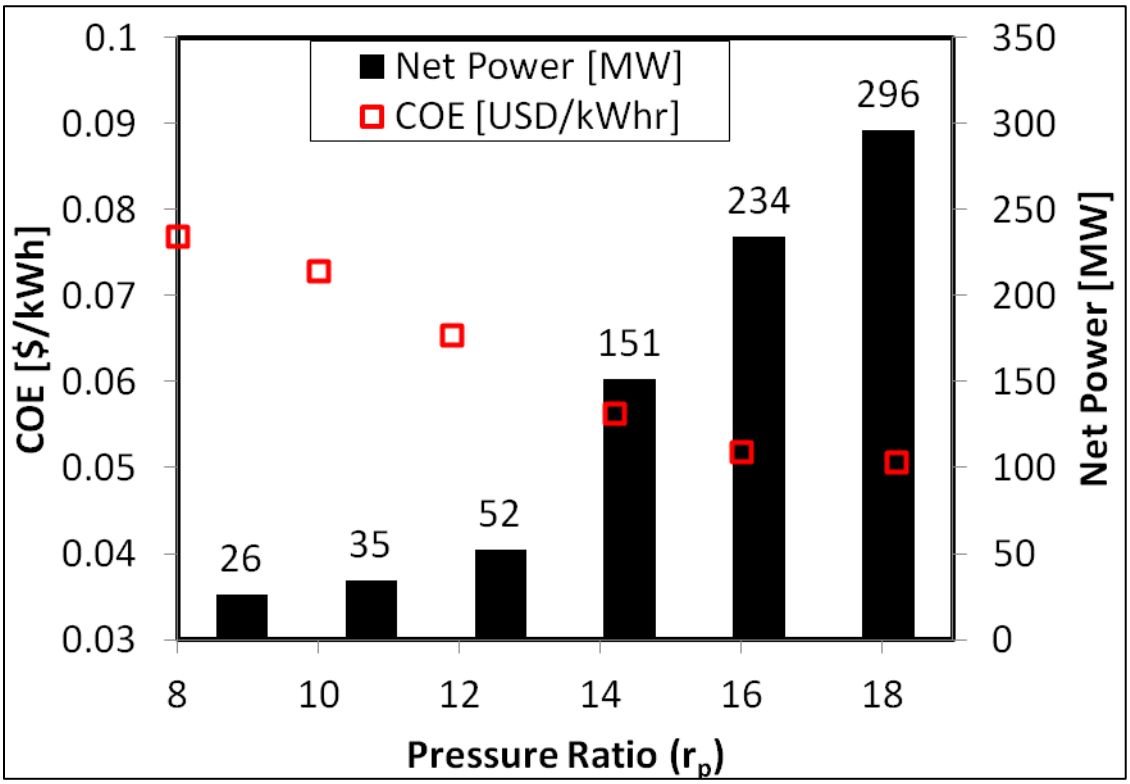

Figure 13: Plant net output power and the levelized cost of electricity for different types of the gas turbines [ambient temperature T = 35˚C and relative humidity RH = 45 %].

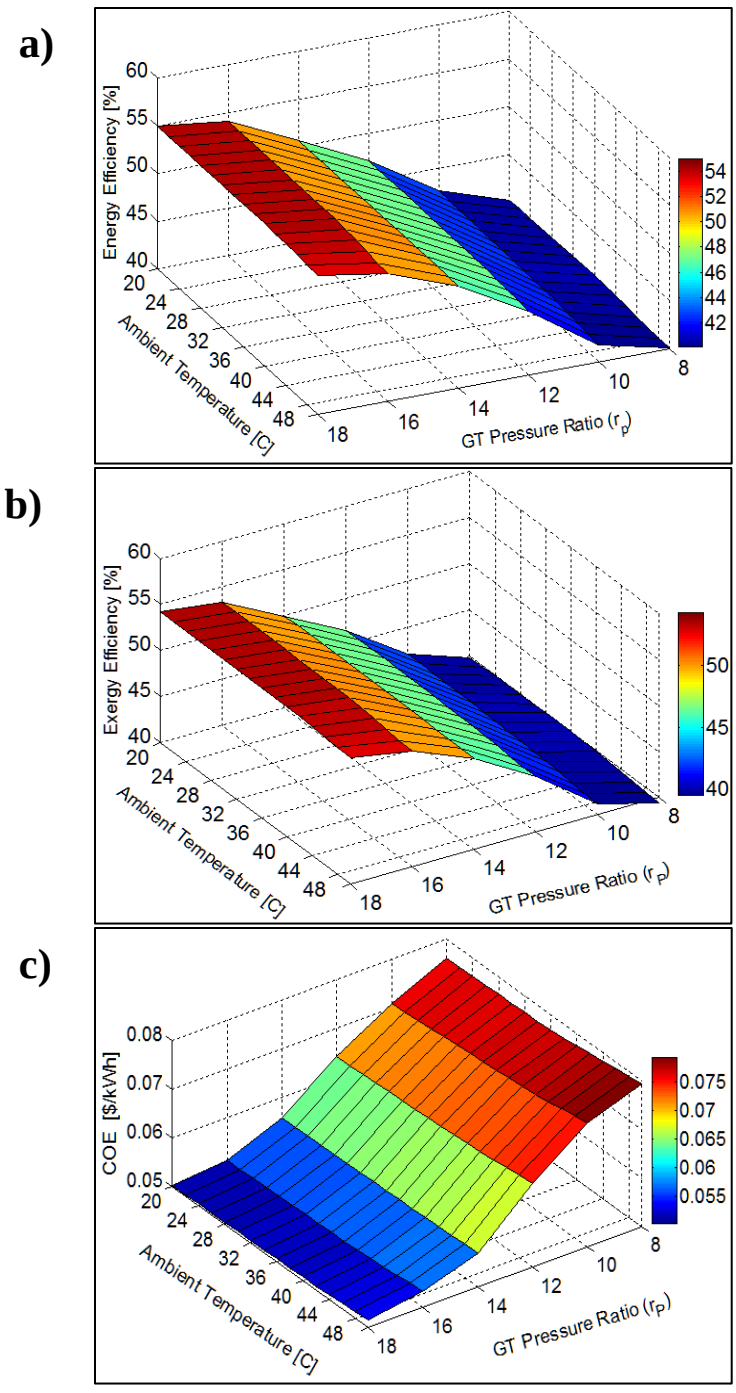

Figure 14: Surface plots of energy efficiency (a), exergy efficiency (b) and levelized cost of electricity (c) variations with the ambient temperature and pressure ratio [relative humidity RH=45 %]

Based on the above analysis it may be concluded that the preferable configuration of the combined cycle power plant is the one with the minimum levelized cost of electricity that is the largest size of the gas turbines with the pressure ratio 18.2. However, in this decision, no consideration is made for the efficiencies and the total investment. As the environmental consciousness increases among the society and economic considerations become more important, it becomes essential to consider also other performance indicators such as the energy efficiency, exergy efficiency and total investment in the decision making process. In the following, we consider four performance indicators in evaluating the overall performance of the combined cycle power plant as:

1. Energy efficiency (ENE [%]).
2. Exergy efficiency (EXE [%]).
3. Levelized cost of electricity (COE [$/kWh]).
4. Total investment (TI [MM$]).

The procedure for the determining the overall performance index (OPI) is shown in Figure (3). Once the important performance indicators are identified, the impact of each of the performance indicators on the overall performance index is determined based on the experience and the user demand [20]. This is made by assigning a weight to each of the performance indicators. In this regard, we consider three cases as shown in Table (12). In case #1 the emphasis is given to the levelized cost of electricity with a highest weight of 55% (conventional case). In case #2 a higher weight is assigned to the exergy efficiency (environmental conscious case) and in case #3 the economical aspects are emphasized with 30% for the levelized cost of electricity and 30% for the total

investment (economical case). For each case a performance matrix is prepared as shown in Table (5). In the performance matrix, performance levels for each of the performance indicators are determined. For energy efficiency, for example, a goal of 52% and a baseline of 44% have been considered. These limits are the acceptable range of performance for this indicator. In addition, a stretch goal of 56% and an absolute lowest limit of 38% are assumed. Similar assessments are done for the other performance indicators. The acceptable range of performance for the exergy efficiency has been set from 42% to 50%. The stretch goal for the exergy efficiency is set to be 54% and the absolute lowest limit is set to be 36%. For the levelized cost of electricity, the acceptable range of performance was 0.06 – 0.07 $/kWh and that for the total investment was 80 – 120 MM $). The last column in Table (5) shows the assigned weights for each of the performance indicator. The last row in this table gives the level score calculation for each of the performance indicators depending on the value of the relevant performance indicator. Overall performance Index (OPI) is the total value of the level scores of the performance indicators.

Table 12: The three considered cases by changing the weight column

Performance Indicator (PI)	Weight Case#1	Weight Case#2	Weight Case#3
ENE (%)	20	5	20
EXE (%)	20	55	20
COE ($/kWh)	55	20	30
TI (MM$)	5	20	30
	Conventional Case	Environmental Conscious Case	Economical Case

Tables (13 to 15) show the overall performance index values for three different cases as function of the ambient temperature and the size of the gas turbine (i.e. the pressure ratio). In all the three cases ambient temperature of 20^{o}C yields the highest OPI, however, the optimum pressure ratio varies from case to case. For case #1, the optimum configuration of the combined cycle power plant is the one with largest gas turbine with a pressure ratio of 18. However, the optimum pressure ratio for the case #2 and case #3 are 16 and 12, respectively. The overall performance index (OPI) variation with the pressure ratio is shown in Figure (15) for the three cases. It is clear from Figure (15) that there is an optimum selection of the pressure ratio with a maximum OPI for each case. Therefore,

selection of the size of the gas turbine depends on the weights assigned to the performance indicators, which are subject subjected to the local requirements and user choices. Figure (16) shows the total cost and levelized cost of electricity for the three optimum cases of configurations with highest OPI. In case #1 (conventional case) the levelized cost of electricity is low even though the total cost is high. On the other hand, for case #2 (environmental conscious case) the levelized cost of electricity is higher but the total cost of investment is lower. For the case #3 (economical case) the total cost of investment is much lower, in spite of the fact that the levelized cost of electricity is much higher. Therefore, the optimum configuration of the combined cycle power plant depends on the choice and preference of performance indicators of the user and may not necessarily be the one with the lowest levelized cost of electricity.

Table 13: OPI simulation results for Case#1

T/pr	**8**	**10**	**12**	**14**	**16**	**18**
20	32.37	60.85	75.95	83.84	88.70	**89.19**
22	32.23	60.23	75.89	83.84	88.66	89.15
24	32.05	59.50	75.84	83.84	88.64	89.11
26	31.82	58.77	75.78	83.86	88.63	89.07
28	31.48	57.90	75.72	83.85	88.60	89.05
30	31.15	57.06	75.65	83.84	88.54	89.02
32	30.81	56.12	75.58	83.82	88.48	89.01
34	30.54	55.14	75.51	83.80	88.47	89.01
36	30.24	54.11	75.43	83.78	88.45	89.01
38	29.01	53.02	75.37	83.74	88.42	89.03
40	27.31	51.77	75.28	83.69	88.25	89.00
42	25.59	50.47	75.18	83.64	88.10	88.96
44	23.89	48.49	75.03	83.58	87.94	88.93
46	22.01	45.88	74.82	83.50	87.62	88.81
48	20.33	43.57	74.56	83.42	87.22	88.50
50	19.00	41.57	74.33	83.32	86.98	88.29

Table 14: OPI simulation results for Case#2

T/Pr	8	10	12	14	16	18
20	49.65	68.88	78.01	79.49	**80.97**	78.60
22	49.81	68.62	78.00	79.52	80.91	78.58
24	49.94	68.28	77.99	79.58	80.93	78.57
26	50.04	67.96	77.97	79.65	80.96	78.55
28	50.04	67.54	77.95	79.69	80.97	78.56
30	50.03	67.16	77.93	79.71	80.95	78.50
32	50.01	66.71	77.90	79.74	80.92	78.50
34	50.02	66.23	77.87	79.76	80.95	78.52
36	50.01	65.73	77.83	79.77	80.94	78.54
38	49.35	65.20	77.81	79.74	80.93	78.64
40	48.30	64.56	77.76	79.72	80.72	78.67
42	47.22	63.88	77.71	79.69	80.55	78.69
44	46.15	62.79	77.63	79.65	80.38	78.74
46	44.97	61.31	77.52	79.59	80.03	78.73
48	43.87	59.92	77.39	79.53	79.62	78.29
50	42.97	58.76	77.27	79.41	79.39	77.99

Table 15: OPI simulation results for Case#3

T/Pr	8	10	12	14	16	18
20	50.38	69.35	**79.10**	76.50	72.79	67.20
22	50.40	68.99	79.08	76.51	72.69	67.17
24	50.39	68.56	79.07	76.55	72.71	67.13
26	50.35	68.14	79.03	76.64	72.76	67.10
28	50.22	67.61	79.01	76.67	72.82	67.11
30	50.10	67.12	78.98	76.69	72.84	67.03
32	49.97	66.56	78.95	76.72	72.86	67.03
34	49.88	65.97	78.92	76.74	72.89	67.06
36	49.77	65.36	78.88	76.76	72.88	67.09
38	49.02	64.70	78.85	76.74	72.89	67.25
40	47.94	63.94	78.81	76.73	72.76	67.29
42	46.83	63.14	78.76	76.72	72.67	67.32
44	45.73	61.89	78.67	76.69	72.58	67.38
46	44.51	60.22	78.55	76.66	72.41	67.39
48	43.41	58.73	78.40	76.63	72.20	67.24
50	42.53	57.44	78.27	76.54	72.07	67.12

Table 16: OPI simulation results for all the three cases when the ambient temperature is 20˚C.

Pr	Case#1	Case#2	Case#3
8	32.37	49.65	50.38
10	60.85	68.88	69.35
12	75.95	78.01	**79.10**
14	83.84	79.49	76.50
16	88.70	**80.97**	72.79
18	**89.19**	78.60	67.20

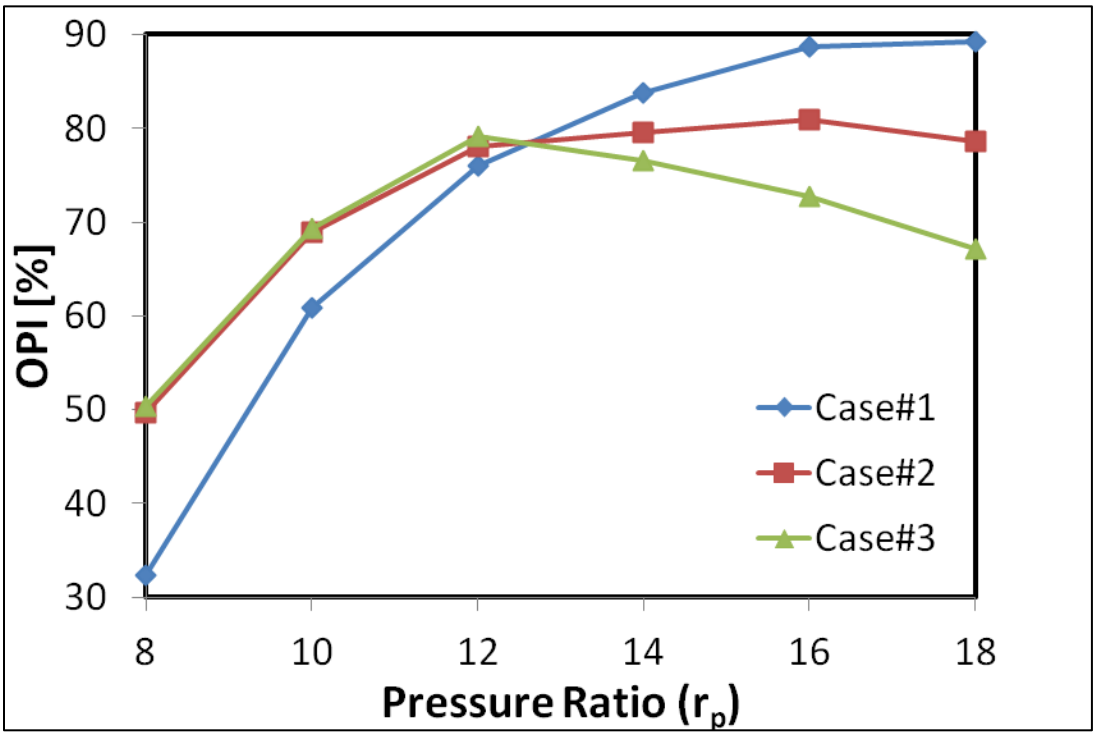

Figure 15: Overall performance index (OPI) variation with the pressure ratio [ambient temperature T = 20 °C and relative humidity RH = 45%]

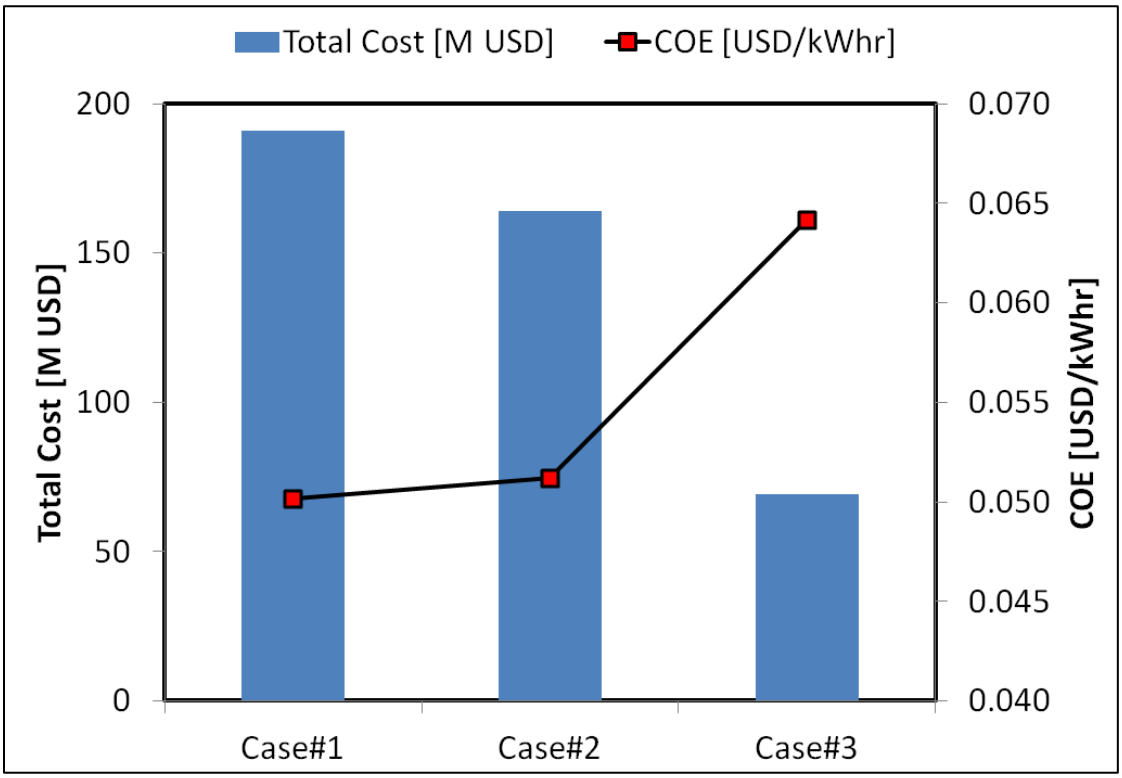

Figure 16: Total cost and levelized cost of electricity for the three optimum cases of configurations with highest OPI.

4.3 Techno-Economic Analysis and Optimization of Different Renewable Energy Systems for Power Generation and Hydrogen Production in Dhahran Area, Kingdom of Saudi Arabia

Solar and wind renewable energy resources are used through PV array and wind turbines to power supply load demand for a typical house located in Dhahran area (Latitude: 26˚ 17'- Longitude: 50˚ 09'), Eastern Province, Saudi Arabia. Six different systems are considered during the simulations as shown in Figure (17). In Systems# 1, 2 and 3, battery bank is used as the storage system while in Systems# 4, 5 and 6, a combination of an electrolyzer, fuel cell and hydrogen tank, is used as a storage system replacing the battery bank. System# 1 comprises PV array with battery bank while in System# 2, the PV array is replaced by wind turbines. System#3 combine solar and wind energy resources in a hybrid system with battery bank storage. On the other hand, for the electrolyzer, fuel cell and hydrogen tank storage system option, the renewable energy resources are; solar for System#4, wind for System# 5 and solar-wind for System#6. Figure (18) shows the load demand profile of a typical resident unit [35] while Figure (19) and Figure (20) show the monthly averaged solar radiation on the horizontal plane and wind speed in Dhahran area, respectively [90]. HOMER generates synthetic hourly solar data from monthly averages using Graham Algorithm [91]. Homer also generates synthetic hourly wind data incorporating Weibull distribution [92]. In the following subsections, a detail description and a schematic diagram of each system are demonstrated and followed by the simulation and optimization results.

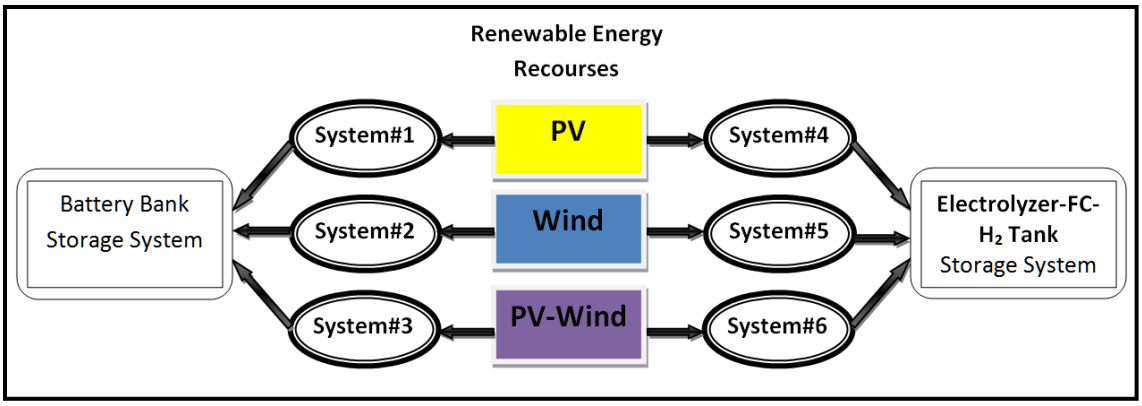

Figure 17: Different renewable energy systems that are considered for the simulations

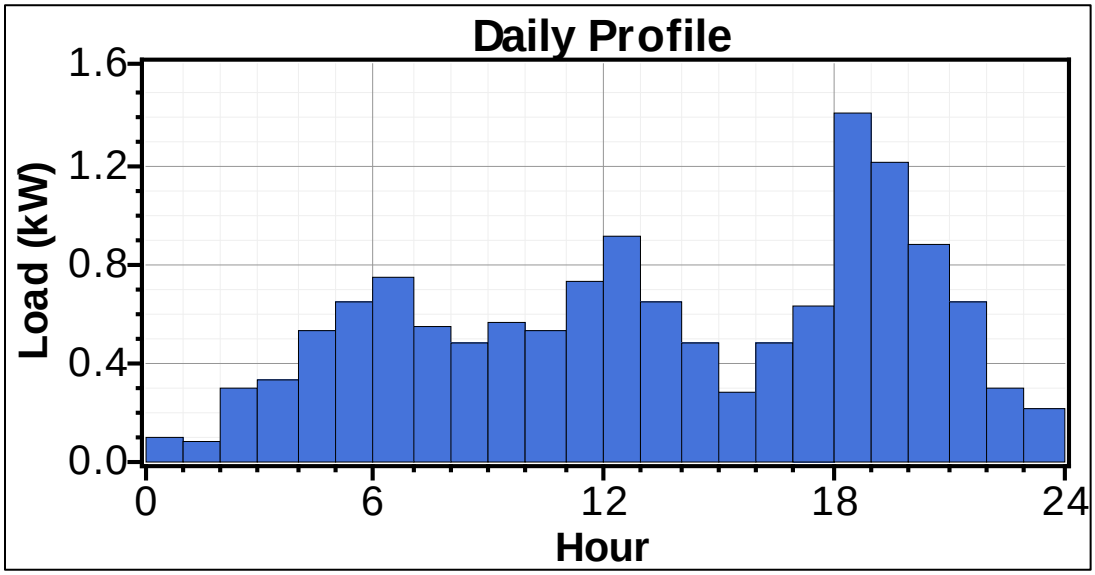

Figure 18: Load demand profile of a typical resident unit [35]

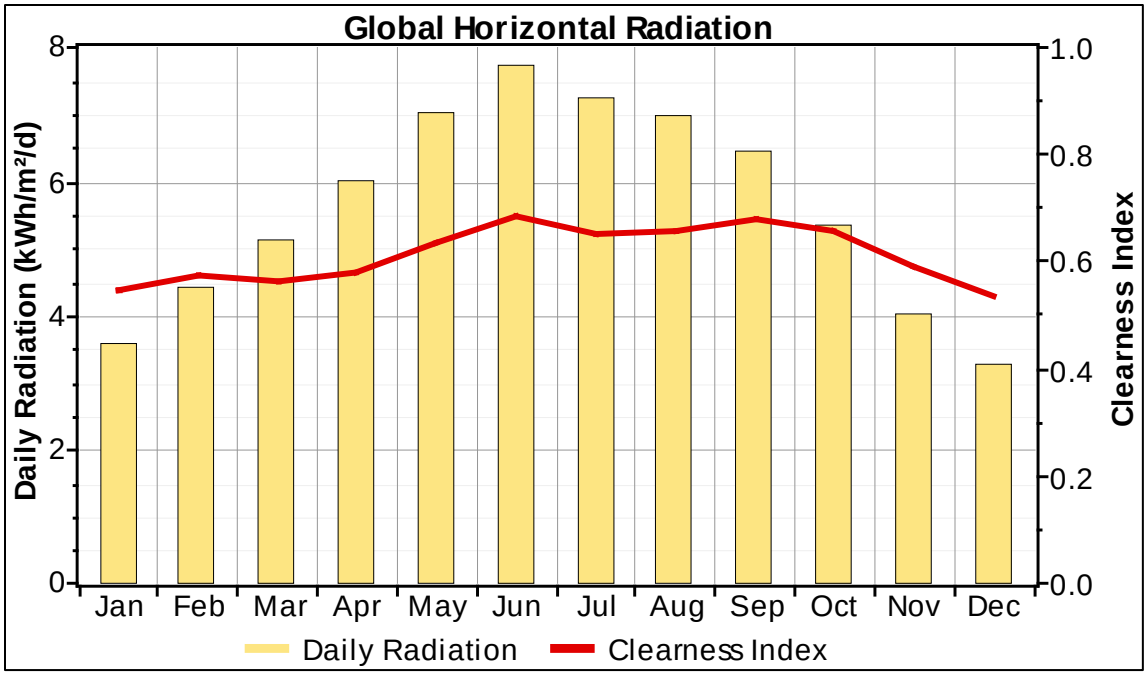

Figure 19: Monthly average solar radiation on horizontal plane at Dhahran [90]

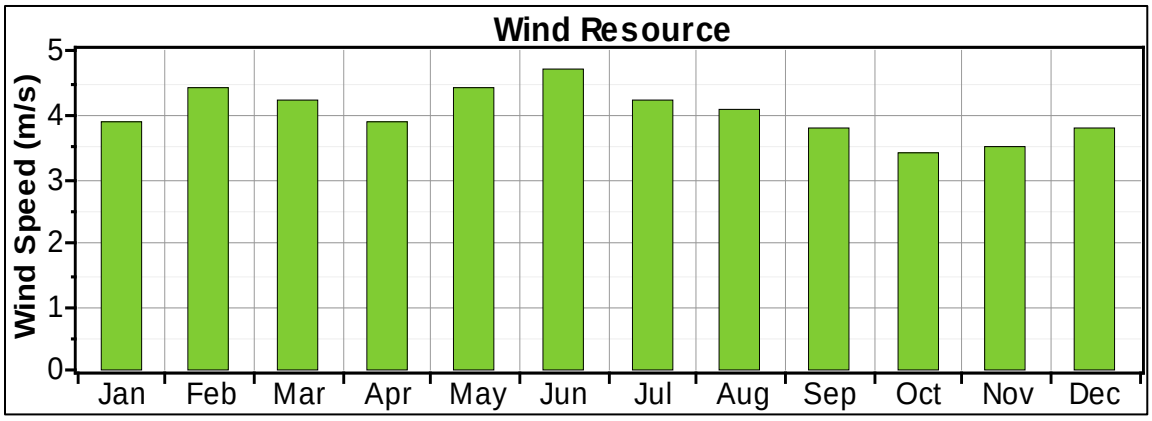

Figure 20: Monthly average wind speed at 10 m height at Dhahran [90]

4.3.1 System#1: PV-Battery Bank System

In this system, the PV panels are used to meet the load requirements of a typical residence unit at Dhahran city. The schematic diagram of this system is shown in Figure (21).

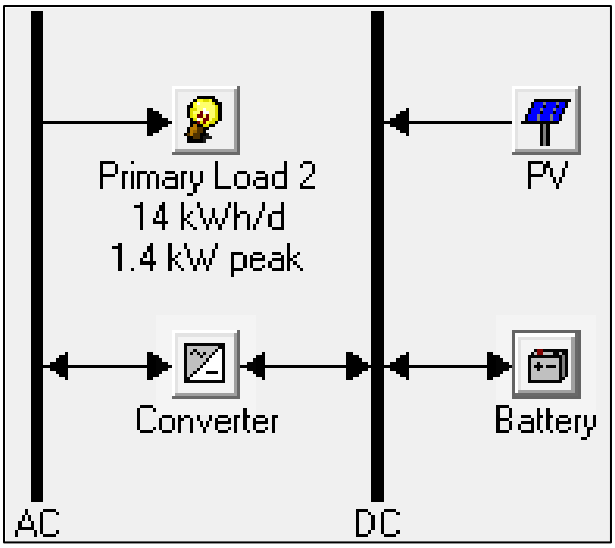

Figure 21: Schematic diagram of System#1 (PV-Battery Bank System)

Hourly base simulations are carried out considering many configurations with different sizes of the system components that lead to cover the load with no deficiency. Among these configurations, the one that cover the load with 100% renewable contribution and has the minimum cost of energy (COE) is to be considered. The range of the PV array size varies from 1 to 8 kW and the range of the batteries varies from 1 to 15 batteries whereas the converter size varies from 1 to 2 kW. The results show that the optimum

system that comprises 4 kW PV array, 10 batteries and 2 kW converter, has the minimum cost of energy (COE). The total net present cost is 48,689 $ and the levelized cost of energy is 0.779 $/kWh. Figure (22) shows the cash flow summary for the net present cost of the system. Figure (23) shows the monthly average electric production of the system.

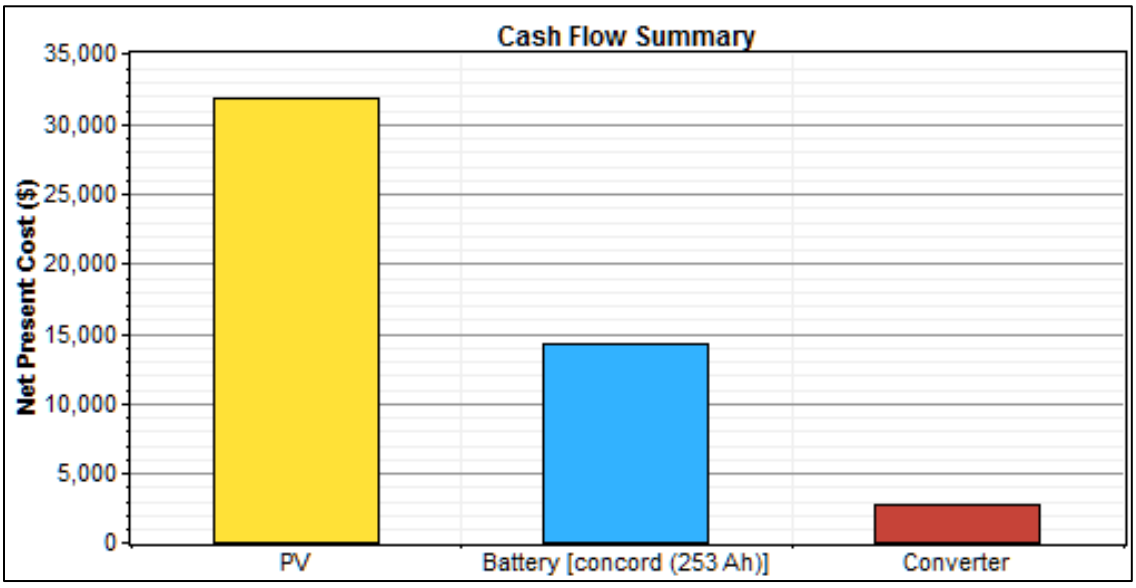

Figure 22: Cash flow summary of System#1 (PV-Battery Bank System)

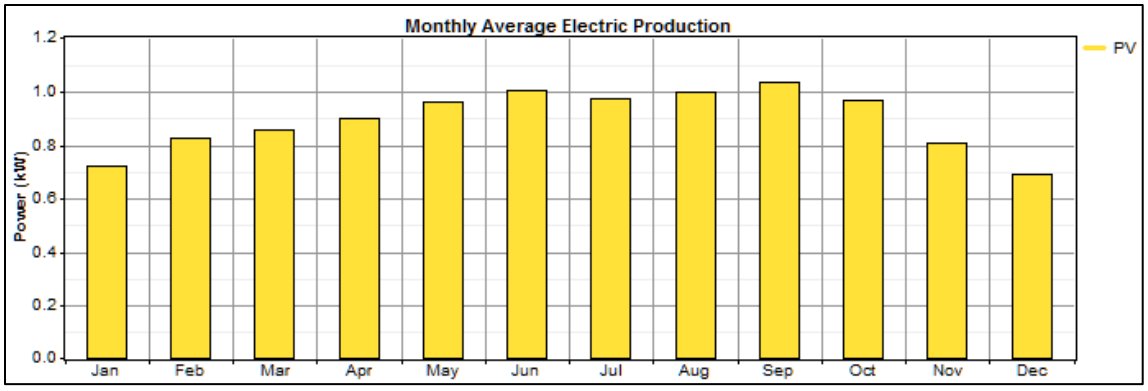

Figure 23: Monthly average electric production of System#1 (PV-battery bank system)

4.3.2 System#2: Wind Turbine-Battery Bank System

In this system, the load has to be met by wind energy as shown in Figure (24). Incorporating either PV array or wind turbines individually, to cover the load, leads to increase the size of the battery bank unless the size of the PV array or the number of the wind turbines is very large. In this case, different number of the wind turbines and batteries are taken into consideration. During the hourly base simulations, the number of the wind turbines varies from 1 to 10 and the number of batteries varies from 1 to 15.

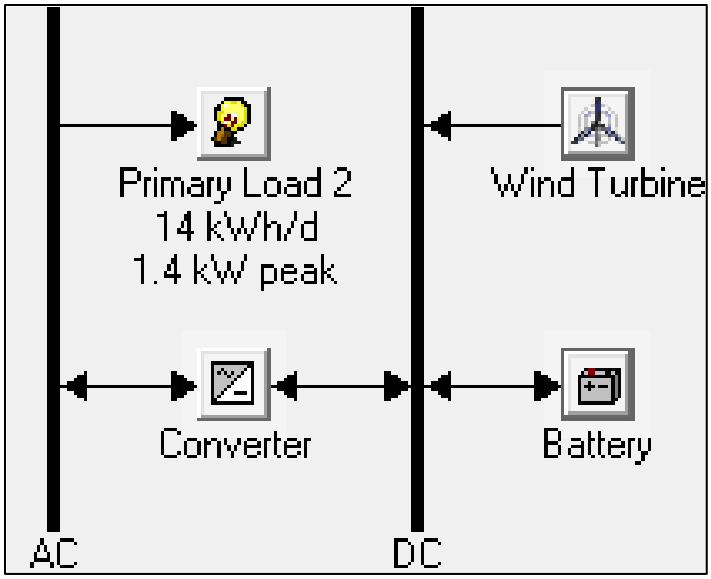

Figure 24: Schematic diagram of System#2 (Wind Turbine-Battery Bank System)

The configuration that has 10 wind turbines, 12 batteries and 2 kW converter has the minimum capital cost of 53,103 $ and the levelized cost of energy is 0.848 $/kWh. More detail of the cash flow is shown in Figure (25). The monthly average electricity production of this system is shown in Figure (26) and the production variability reflects the nature randomness and trend of the wind speed data (Figure (20)).

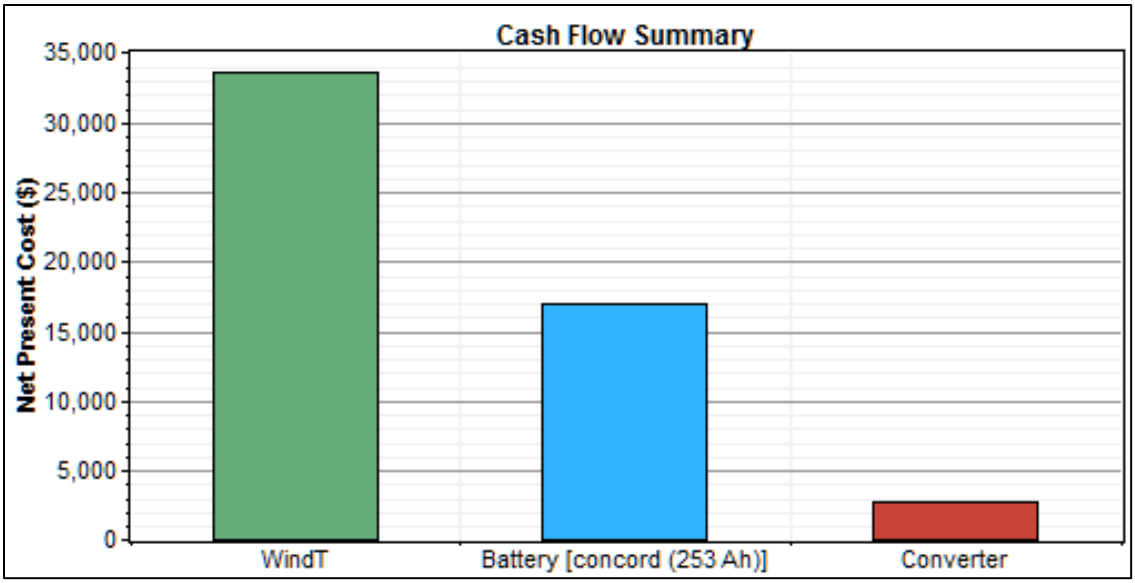

Figure 25: Cash flow summary of System#2 (Wind Turbine-Battery Bank System)

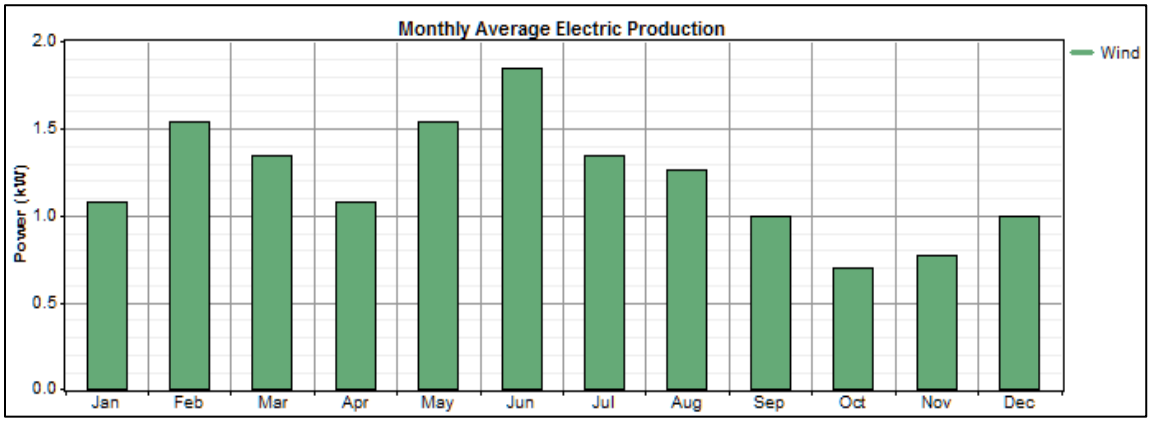

Figure 26: Monthly average electricity production of System#2 (Wind Turbine-Battery Bank System)

4.3.3 System#3: PV-Wind Turbine-Battery Bank System

Solar energy is not available at night and wind energy is not available when the local wind speed is low. Solar and wind energies are integrated together in this system so that each one cover the weakness of the other. This arrangement would lead to decrease the total cost and the levelized cost of energy. Figure (27) shows a schematic diagram of this system.

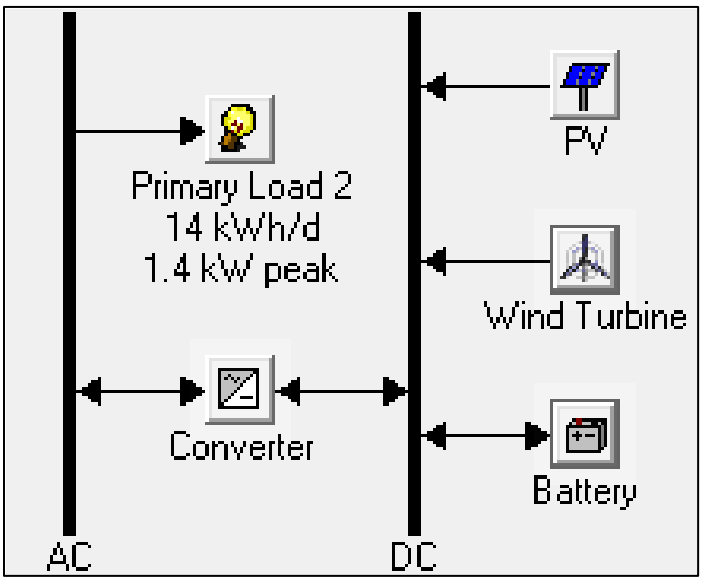

Figure 27: Schematic diagram of System#3 (PV-Wind Turbine-Battery Bank System)

Hourly simulations are carried out incorporating the hourly local weather data. Different sizes of the hybrid system component are considered. The size of PV array varies from 1 to 5 kW; the number of the wind turbines varies from 1 to 2 and the number of the batteries varies from 1 to 15. Among of these configurations, the one which comprises 3 kW PV array, 2 wind turbines, 2 kW converter and 10 batteries gives the minimum cost.

The net present cost of this system is 44,018 $ and the levelized cost of energy is 0.702 $/kWh. More detail about the cash flow is shown in Figure (28). The PV array represents the major cost of the system with 54.3 % whereas the battery bank, wind turbines and the converter represent 32 %, 7.6 % and 6 %, respectively. 85 % of the power is generated by the PV array and 15 % is generated by the wind turbines. The monthly average electricity production of the hybrid system is shown in Figure (29).

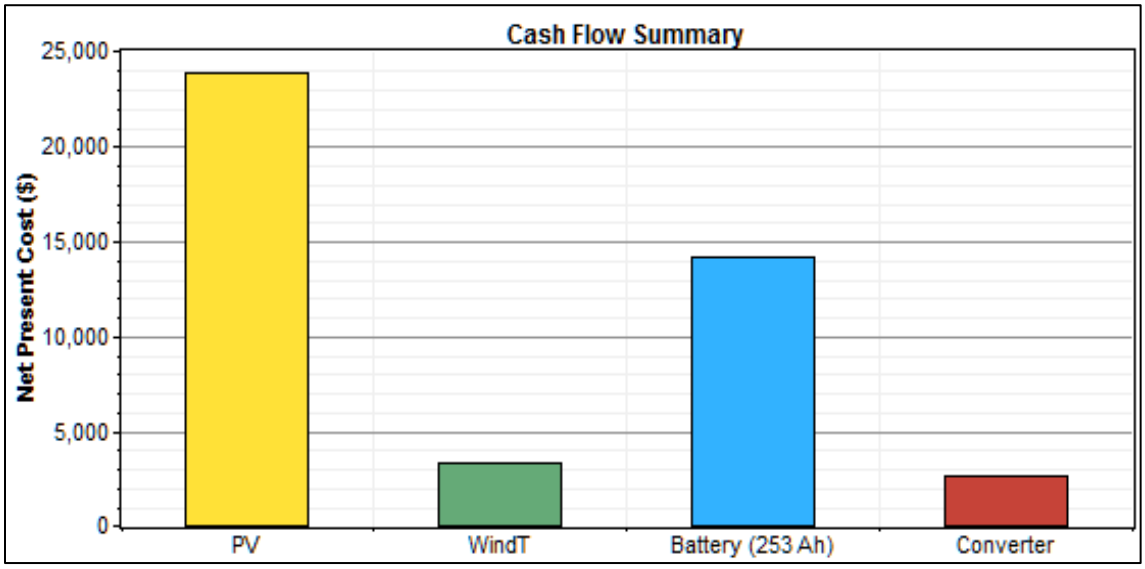

Figure 28: Cash flow summary of System#3 (PV-wind turbine-battery bank system)

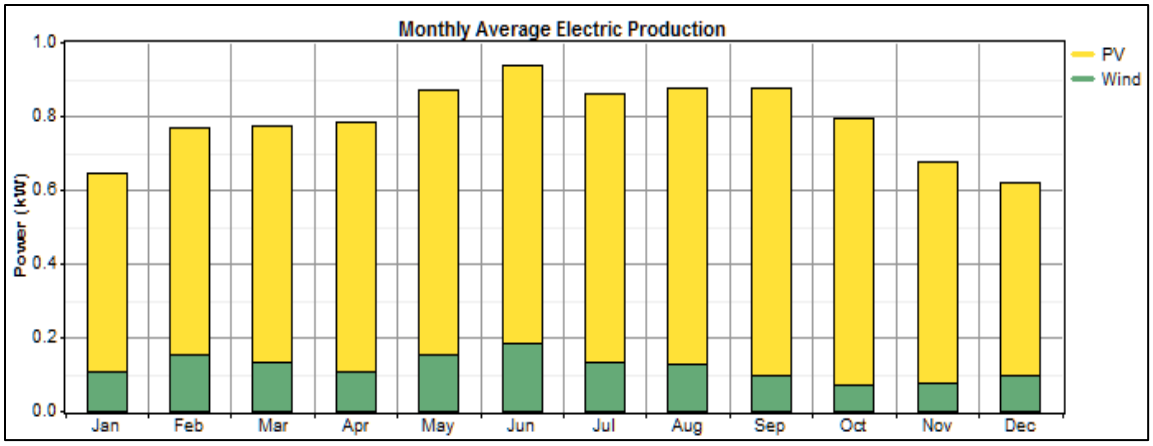

Figure 29: Monthly average electricity production of System#3 (PV-Wind Turbine-Battery Bank System)

4.3.4 System#4: PV-Fuel Cell System

In this system, the generated power by the PV array should cover the load demand and a storage system is needed. In case that the generated power is more than the load demand, the surplus energy goes to the electrolyzer to produce the hydrogen which is then stored in the hydrogen tank. At night or in case that the power generated by the PV array at the sunlight hours cannot meet the load demand, the fuel cell is used to convert the chemical energy of the hydrogen to electricity. The electrolyzer, hydrogen tank and the fuel cell work as a storage system. A schematic diagram of this system is shown in Figure (30)

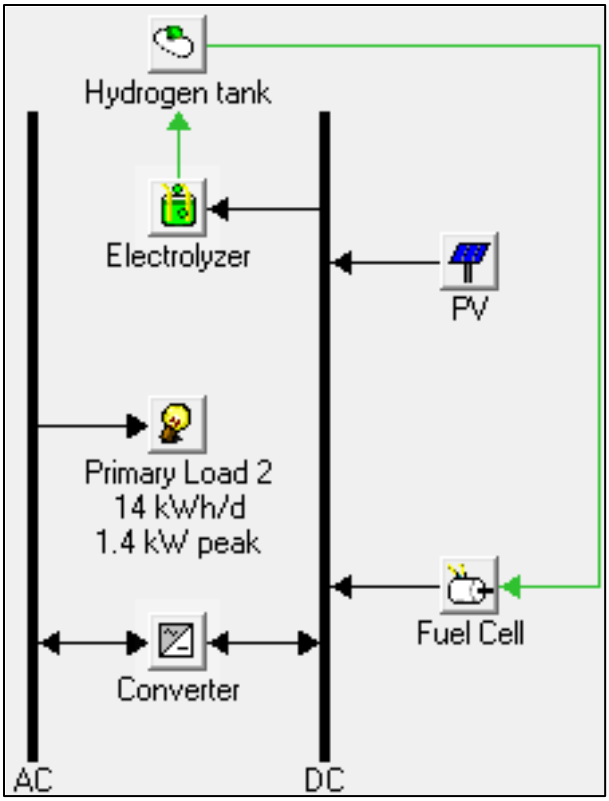

Figure 30: Schematic diagram of System#4 (PV-Fuel Cell System)

Many configurations of the system components are considered during the hourly simulations. The size of the PV array varies from 1 to 10 kW; the size of the fuel cell varies from 1 to 5 kW; the size of the electrolyzer varies from 1 to 8 kW; the size of the hydrogen tank varies from 1 to 12 kg and the size of the converter varies from 1 to 2 kW. Many combinations of these components can meet the load demand however the one that leads to the minimum cost will be chosen as the optimum configuration. The simulation results show that the system that comprises 6 kW PV array, 2 kW fuel cell, 2 kW converter, 5 kW electrolyzer and 7 kg hydrogen tank, gives the minimum COE with 1.608 $/kWh. More details about the cash flow are shown in Figure (31). The PV array represents 47.5 % of the total cost followed by the fuel cell which represents 26 %.

Figure (32) show the monthly average production of this system. The PV array produces 80 % whereas the fuel cell produces 20 %. The monthly average hydrogen production of the 5 kW electrolyzer is shown in Figure (33) and the hydrogen tank storage level is shown in Figure (34). The tank level increases from January until May then; it reaches and stays at the maximum capacity (7 kg) from June until October. The level of the tank decreases during the months of November and December due to the decreasing solar radiation.

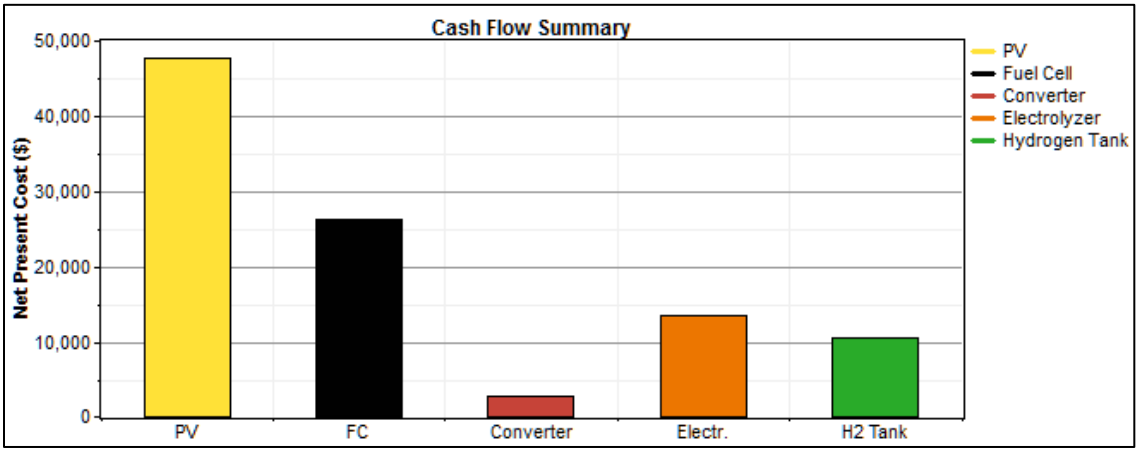

Figure 31: Cash flow summary of System#4 (PV-Fuel cell system)

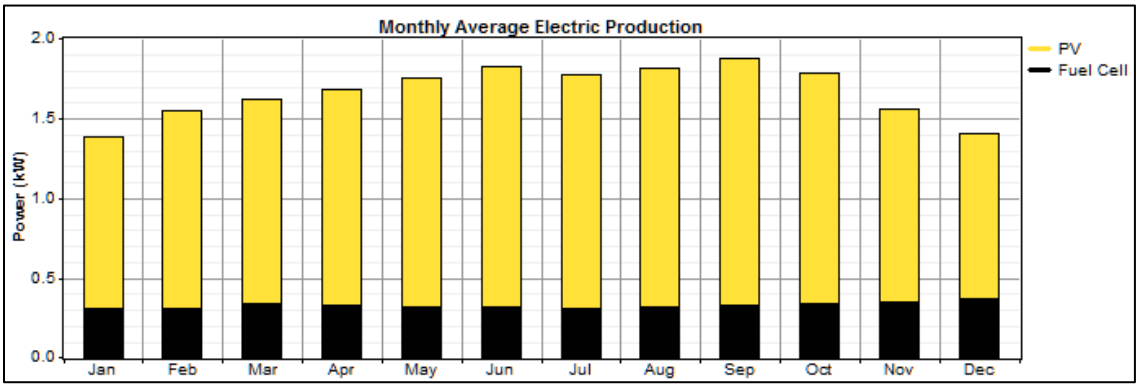

Figure 32: Monthly average electric production of System#4 (PV-Fuel Cell)

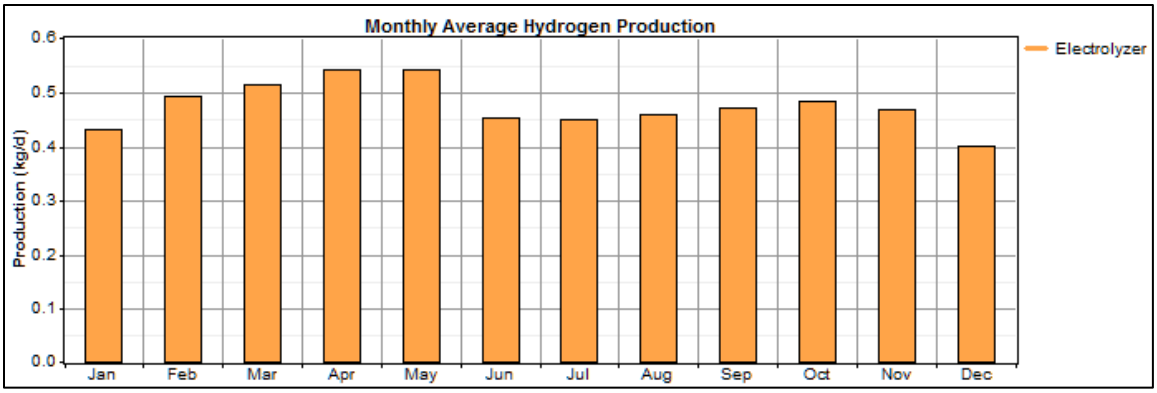

Figure 33: Monthly average hydrogen production of System#4 (PV-Fuel Cell)

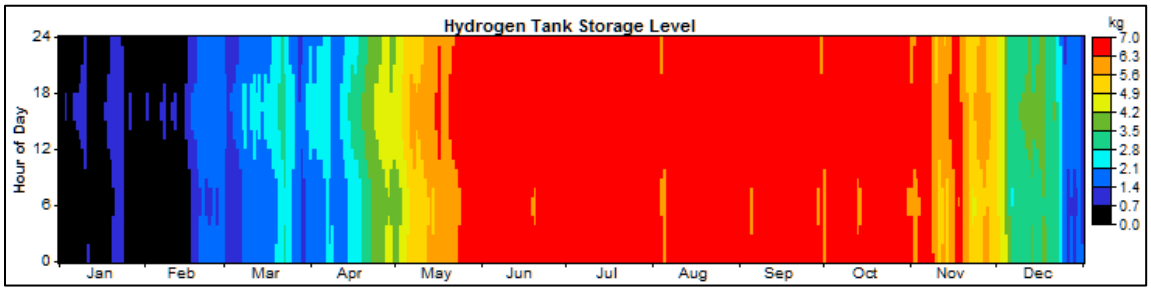

Figure 34: Hydrogen tank storage level of System#4 (PV-Fuel Cell)

4.3.5 System#5: Wind-Fuel Cell System

Wind energy potential in Dhahran area is investigated through replacing the PV array of System#4 by wind turbines as shown in Figure (35). In this case, the power generated by the wind turbines covers the load demand and the surplus electricity goes to the electrolyzer to produce hydrogen which is stored in the hydrogen tank. When the wind speed of the installation location is low, the fuel cell is used to generate electricity and cover the load demand.

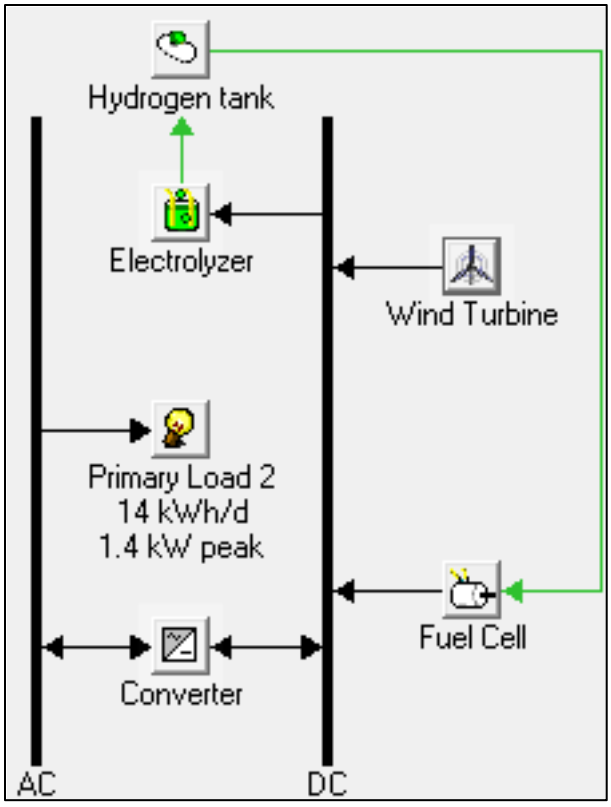

Figure 35: Schematic diagram of Wind-Fuel Cell System

Many configurations of the system components are considered during the simulations. The number of wind turbines varies from 1 to 15; the size of the fuel cell varies from 1 to 4 kW; the size of the electrolyzer varies from 1 to 8 kW; the size of the hydrogen tank varies from 1 to 10 kg and the size of the converter varies from 1 to 2 kW. The minimum COE of 1.564 $/kWh, is achieved with the combination of 15 wind turbines, 2 kW fuel cell, 4 kW electrolyzer, 2 kW converter and 5 kg hydrogen tank. Figure (36) shows the cash flow summary of this system with total net present cost of 97,579 $. The wind turbines represent major contribution of the system cost (more than 51 %) flowed by fuel cell (27 %), electrolyzer (11 %), hydrogen tank (7.7), and converter (3.3 %). Monthly

averaged electric production is shown in Figure (37). It is clear that the electric production follows the trend of the monthly averaged local wind speed of Dhahran area (Figure (20)). It can be observed from Figure (37) that the maximum electric production occurs in June where the monthly average wind speed has a maximum value of 4.7 m/s whereas the minimum electric productions occurs in October where the wind speed is in the order of 3.5 m/s. The wind turbines produce 15,838 kW/yr (88 %) and the fuel cell produces 2,172 kW/yr (12 %). 4 kW electrolyzer is used in this system to produce hydrogen which is sent to the hydrogen tank and used by the fuel cell when it is needed. The monthly average hydrogen production by this system is shown in Figure (38) whereas Figure (39) shows the hydrogen tank storage level. It can be also observed that the hydrogen tank level starts dropping in October due to minimum wind speed at this month.

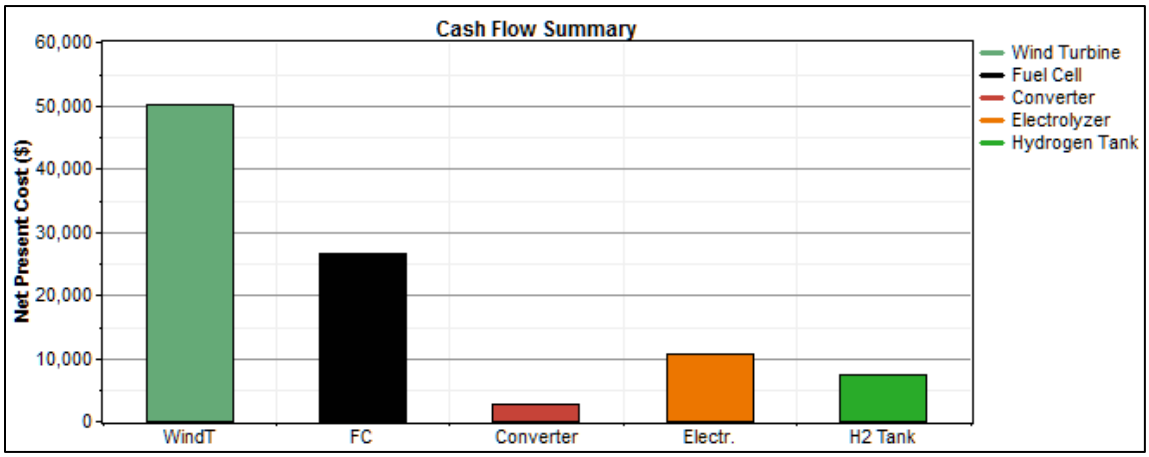

Figure 36: Cash flow summary of System#5 (Wind-Fuel Cell System)

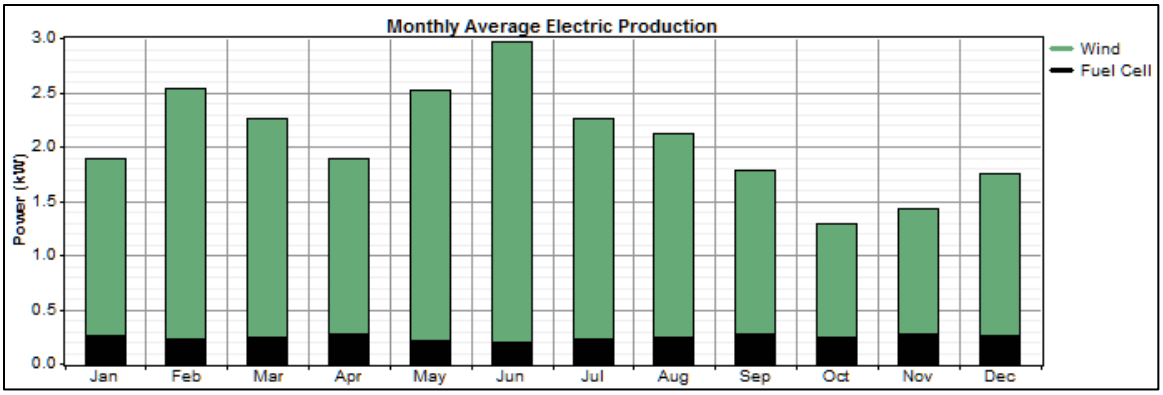

Figure 37: Monthly average electric production of System#5 (Wind-Fuel Cell System)

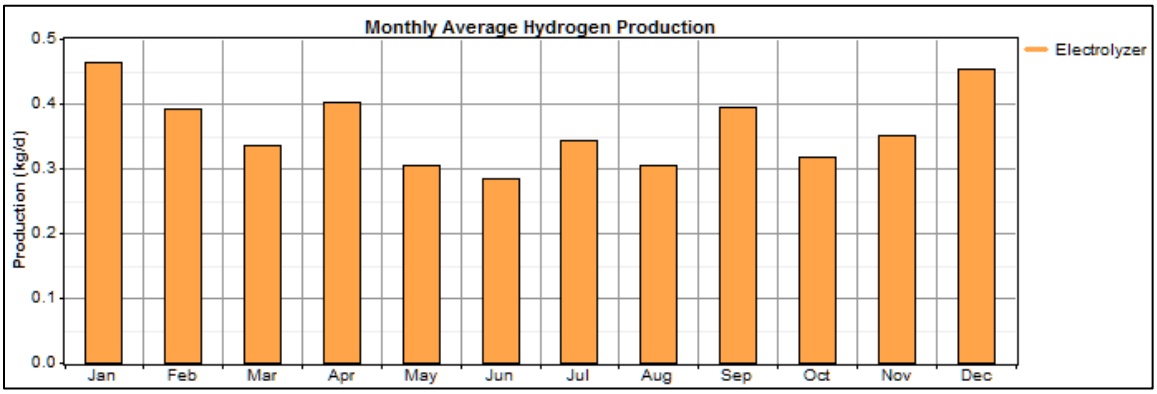

Figure 38: Monthly average hydrogen production of System#5 (Wind-Fuel Cell System)

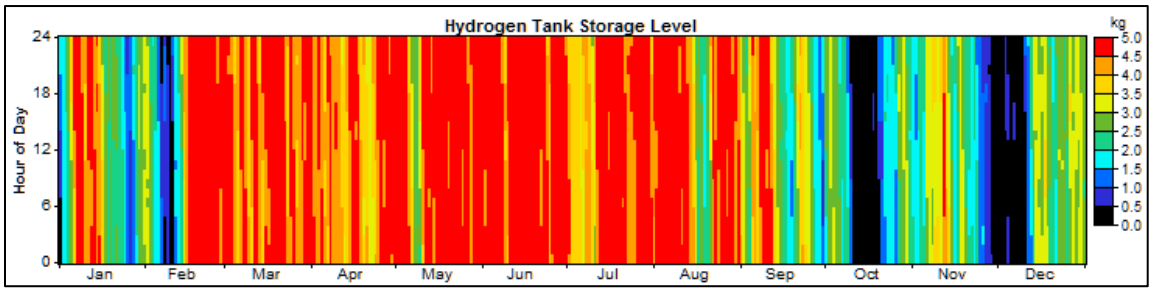

Figure 39: Hydrogen tank storage level of System#5 (Wind-Fuel Cell System)

4.3.6 System#6: PV-Wind Fuel Cell System

In this system, solar and wind resources are integrated with fuel cell-electrolyzer-hydrogen tank, storage system to cover the load demand and examine hydrogen production potential and cost at Dhahran area. A schematic diagram of this system is shown in Figure (40).

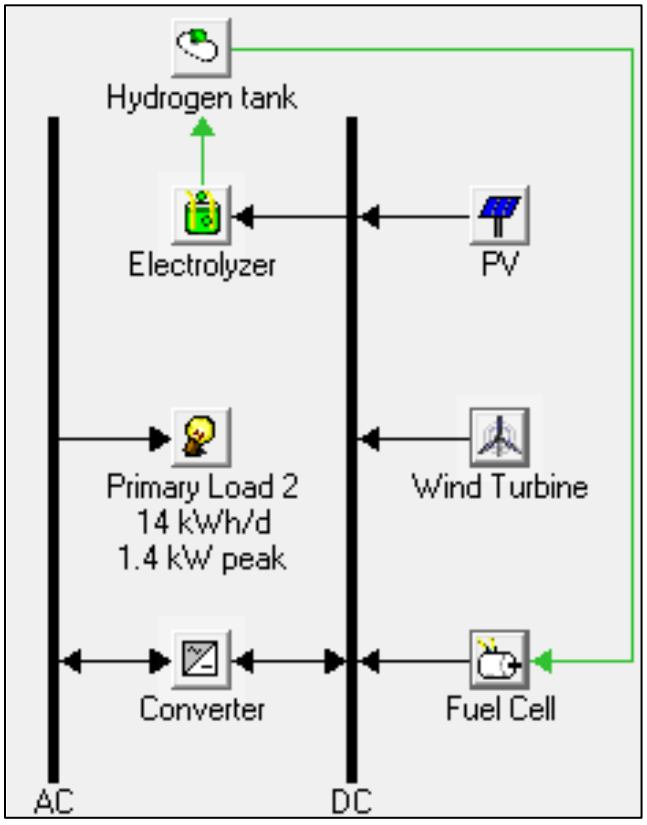

Figure 40: Schematic diagram of PV-Wind-Fuel Cell System

Different configurations are considered during the simulations by changing the sizes of the hybrid system components as; the size of the PV array varies from 1 to 8 kW; the number of the wind turbines varies from 1 to 2; the size of the fuel cell varies from 1 to 3

kW; the size of the electrolyzer varies from 1 to 5 kW; the size of the hydrogen tank varies from 1 to 7 kg and the size of the converter varies from 1 to 2 kW. The system configuration that leads to minimum COE of 1.459 $/kWh has 5 kW PV array, 2 wind turbines, 2 kW fuel cell, 3 kW electrolyzer, 2 kW converter and 6 kg hydrogen tank. More details about the cash flow are shown in Figure (41). It is observed that the PV array represent the major contribution of the total cost (43.5 %) followed by fuel cell (27.6 %), wind turbines (7.3 %), hydrogen tank (9.9), electrolyzer (8.7 %) and converter (3 %). PV array contributes with 69 % of the total electricity production as shown in Figure (42) whereas the wind turbines contribute with 15 % and the fuel cell produces 16 %. Figure (43) shows the monthly average hydrogen production whereas Figure (44) shows the hydrogen tank level. It can be observe that the hydrogen level of this system is better than that in either System#4 or Syetem#5 due to the advantages of integrating two renewable resources (solar and wind) in one hybrid system.

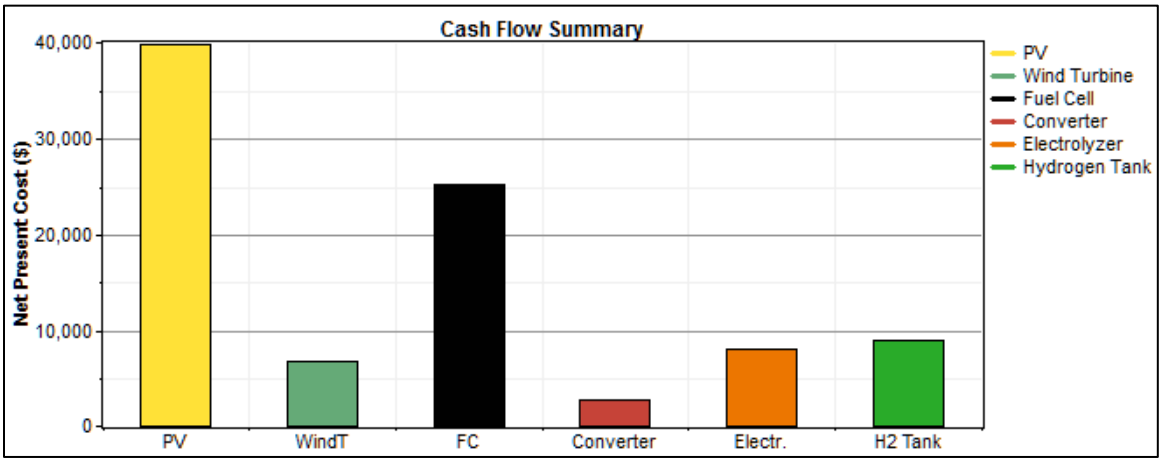

Figure 41: Cash flow summary of System#6 (PV-Wind-Fuel Cell System)

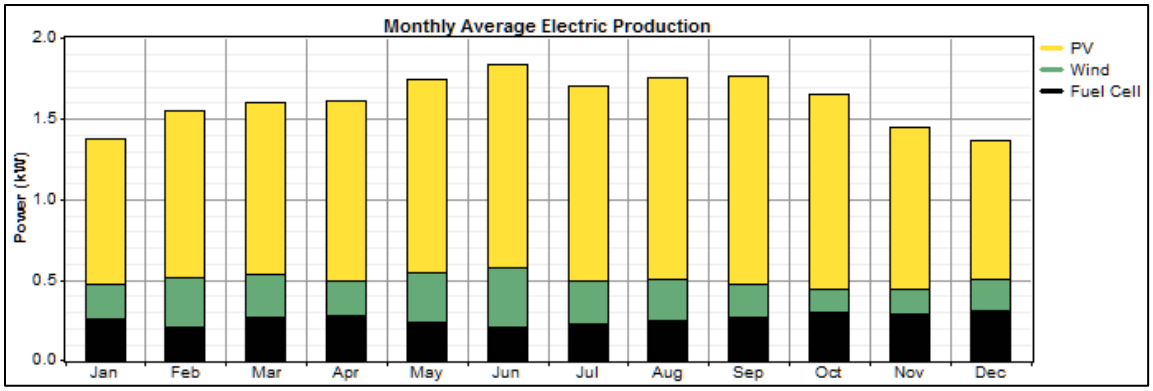

Figure 42: Monthly average electricity production of System#6 (PV-Wind-Fuel Cell System)

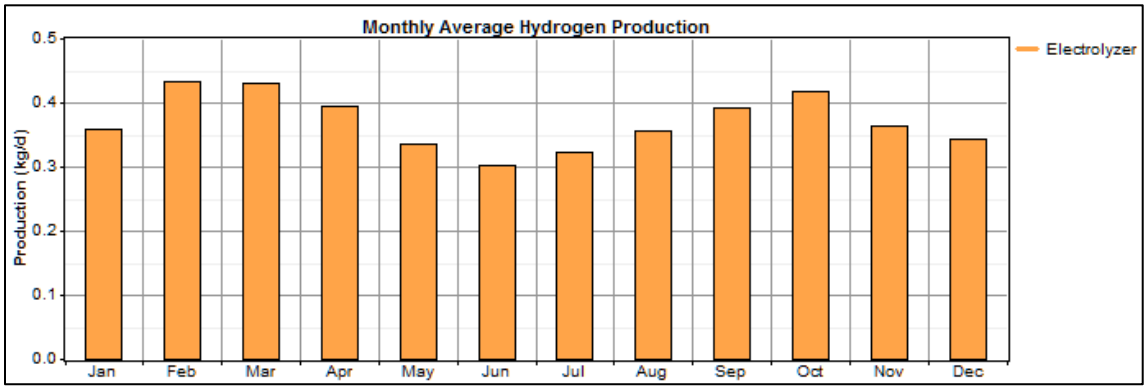

Figure 43: Monthly average hydrogen production of System#6 (PV-Wind-Fuel Cell System)

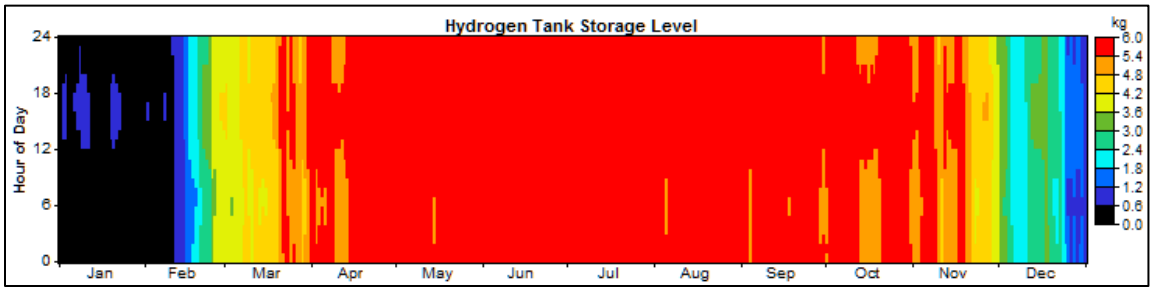

Figure 44: Hydrogen tank storage level of System#6 (PV-Wind-Fuel Cell System)

4.4 Generalizing the Renewable Energy Systems for Power Generation and Hydrogen Production at Several Areas in the Kingdom of Saudi Arabia

The renewable energy systems analyzed above are now considered at different locations in the Kingdom of Saudi Arabia (the map is shown in Figure (45)). Weather data vary from location to location; therefore, different system configurations are expected to satisfy the same load. The target of these simulations is to determine the optimum system configurations that satisfy the load and minimize the cost at each location and compare between the systems and investigate the renewable energy potential in these locations.

Figure 45: Map of the Kingdom of Saudi Arabia showing the locations under study

Table (17) shows the annual average solar radiation and wind speed at five locations in the Kingdom (Dhahran, Riyadh, Jeddah, Abha and Yanbu) [90]. From this table, it is clear that Jeddah City has the maximum annual solar radiation with (5.94 kWh/m^2/day) whereas Riyadh City has the maximum annual wind speed with (4.1 m/s). Figure (46) and (47) show the variation of the monthly average solar radiation and wind speed, respectively. It can be seen that Riyadh has the maximum solar radiation in June but the other cities (Jeddah and Abha) have more solar radiation in winter months. These variations in the weather data affect the simulation results and hence lead to different combinations of the systems components. The best configuration is to be chosen where the minimum levelized cost of energy is achieved while the renewable contribution (RF) is 100%.

Table 17: Annual average solar radiation at different locations in KSA [90]

City	Latitude	Longitude	Daily solar radiation	Wind speed
			kWh/m^2/day	m/s
Dhahran	26°17' N	50° 9' E	5.60	4
Riyadh	24° 39' N	46° 42' E	5.77	4.1
Jeddah	21°28' N	39° 10' E	5.94	3.8
Abha	18°23' N	42° 49 E	5.93	3.9
Yanbu	24°08' N	38° 3' E	5.9	3.7

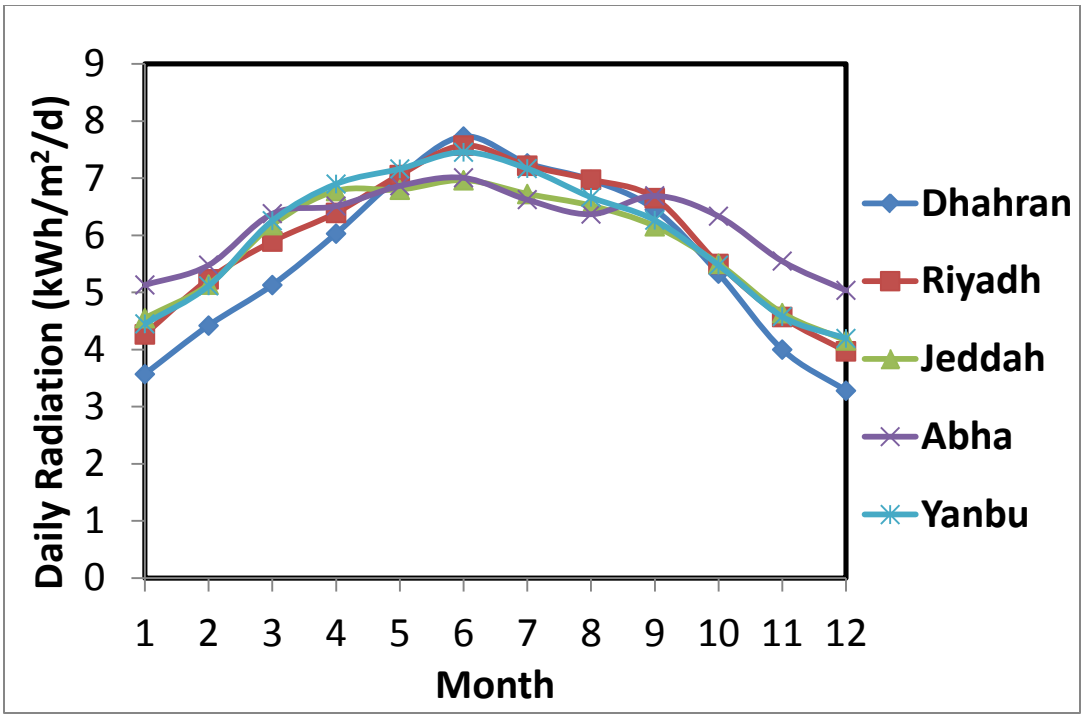

Figure 46: Monthly average daily solar radiation at different location in KSA

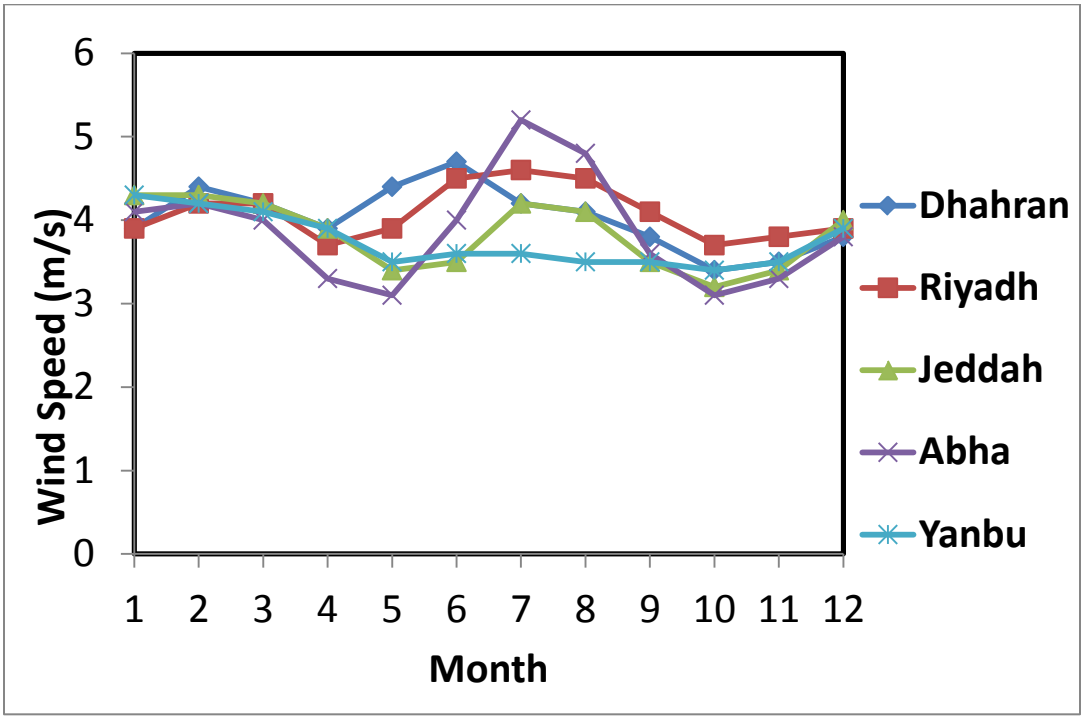

Figure 47: Monthly average wind speed at different location in KSA

The aim of these simulations is to assess the renewable energy resources potentials at different locations in the Kingdom by taking into consideration the different renewable energy systems. Tables (18-22) give summaries of the simulation results of Dhahran, Riyadh, Jeddah, Abha and Yanbu, respectively. These results can be divided into two categories. The first category involves the systems that have battery bank (System#1, 2 and 3) and the second one involves the systems that have; electrolyzer, fuel cell, hydrogen tank which work as a storage system replacing the battery bank (System#4, 5 and 6).

1. The results show that for Dhahran area (Table (18)), System#3 (PV-Wind-Batt) has the minimum COE (0.702 $/kWh) with (3 kW PV array, 1 wind turbine, 10 batteries and 2 kW converter). For the systems that produce hydrogen and use FC/electrolyzer/hydrogen tank as the storage system, System#6 (PV-Wind-FC) has the least COE with 1.459 $/kWh and the hydrogen production cost (COH) is 52.9 $/kg and the combination has 5 kW PV array, 2 wind turbines, 2 kW converter, 2 kW fuel cell, 3 kW electrolyzer and 6 kg hydrogen tank.
2. In Riyadh area (Table (19)), System#3 also gives the least COE with 0.612 $/kWh and the combination was with 2 kW PV array, 3 wind turbines, 7 batteries and 2 kW converter. For the second category, System#6 (4 kW PV array, 2 wind turbines, 2 kW converter, 2 kW fuel cell, 3 kW electrolyzer and 6 kg hydrogen tank) gives the minimum COE with 1.327 $/kWh and COH is 47.2 $/kg.
3. System#3 also gives the minimum cost in Jeddah area (Table (20)) with (2 kW PV array, 3 wind turbine, 7 batteries and 2 kW converter) and the COE is 0.616 $/kWh. For hydrogen production storage systems, System#6 (4 kW PV array, 2

wind turbines, 2 kW converter, 2 kW fuel cell, 3 kW electrolyzer and 2 kg hydrogen tank) gives the minimum COE with 1.28 $/kWh and COH is 45.2 $/kg.

4. In Abha area at the west-south region of the Kingdom (Table (21)), System#3 also gives the best performance and cover the load with minimum COE with 0.614 $/kWh. The configuration comprises 2 kW PV array, 3 wind turbine, 7 batteries and 2 kW converter. On the other hand, for the hydrogen production storage system, System#6 has the minimum COE with 1.208 $/kWh and COH is 43.3 $/kg. The optimum configuration has 4 kW PV array, 2 wind turbines, 2 kW converter, 2 kW fuel cell, 3 kW electrolyzer and 1 kg hydrogen tank.
5. Finally, at Yanbu area (Table (22)), with COE of 0.609 $/kWh, System#3 is the best choice with (2 kW PV array, 3 wind turbine, 7 batteries and 2 kW converter). For the second category, System#6 gives the minimum COE with 1.231 and COH is 43.1 $/kg. The configuration of this system has 4 kW PV array, 2 wind turbines, 2 kW converter, 2 kW fuel cell, 3 kW electrolyzer and 2 kg hydrogen tank.

Table 18: Results of the economic analysis of different renewable energy systems at* Dhahran *area

Location	**Dhahran** (Latitude: 26°17' N – Longitude 50° 9'E)					
	System#1	System#2	System#3	System#4	System#5	System#6
	PV-Batt	Wind-Batt	PV-Wind-Batt	PV-FC	Wind-FC	PV-Wind-FC
PV Array (kW)	4	0	3	6	0	5
Wind Turbines	0	10	1	0	15	2
Batteries	10	12	10	0	0	0
Converter (kW)	2	2	2	2	2	2
Fuel Cell (kW)	0	0	0	2	2	2
Electrolyzer (kW)	0	0	0	5	4	3
Hydrogen Tank (kg)	0	0	0	7	5	6
Total NPC ($)	48,689	53,103	44,018	100,486	97,579	91,459
COE ($/kWh)	0.779	0.848	0.702	1.608	1.564	1.459
COH ($/kg H_2)	0	0	0	45.4	57.7	52.9
RF	1	1	1	1	1	1

Table 19: Results of the economic analysis of different renewable energy systems at* Riyadh *area

Location	**Riyadh** (Latitude: 24°39' N – Longitude 46° 42' E)					
	System#1	System#2	System#3	System#4	System#5	System#6
	PV-Batt	Wind-Batt	PV-Wind-Batt	PV-FC	Wind-FC	PV-Wind-FC
PV Array (kW)	3	0	2	6	0	4
Wind Turbines	0	8	3	0	15	2
Batteries	11	13	7	0	0	0
Converter (kW)	2	2	2	2	2	2
Fuel Cell (kW)	0	0	0	2	2	2
Electrolyzer (kW)	0	0	0	3	4	3
Hydrogen Tank (kg)	0	0	0	7	4	6
Total NPC ($)	42,147	47,816	38,523	94,816	96,147	83,295
COE ($/kWh)	0.671	0.761	0.612	1.513	1.536	1.327
COH ($/kg H_2)	0	0	0	43.2	56.2	47.2
RF	1	1	1	1	1	1

Table 20: Results of the economic analysis of different renewable energy systems at* Jeddah *area

Location	**Jeddah** (Latitude: 21°28' N – Longitude 39° 10' E)					
	System#1	System#2	System#3	System#4	System#5	System#6
	PV-Batt	Wind-Batt	PV-Wind-Batt	PV-FC	Wind-FC	PV-Wind-FC
PV Array (kW)	3	0	2	6	0	4
Wind Turbines	0	10	3	0	13	2
Batteries	13	12	7	0	0	0
Converter (kW)	2	2	2	2	2	2
Fuel Cell (kW)	0	0	0	2	2	2
Electrolyzer (kW)	0	0	0	4	4	4
Hydrogen Tank (kg)	0	0	0	2	11	2
Total NPC ($)	44,982	53,103	38,523	89,907	101,052	80,085
COE ($/kWh)	0.720	0.849	0.616	1.428	1.615	1.28
COH ($/kg H_2)	0	0	0	40	55.8	45.2
RF	1	1	1	1	1	1

Table 21: Results of the economic analysis of different renewable energy systems at* Abha *area

Location	**Abha** (Latitude: 18°23' N – Longitude 42° 49 E)					
	System#1	System#2	System#3	System#4	System#5	System#6
	PV-Batt	Wind-Batt	PV-Wind-Batt	PV-FC	Wind-FC	PV-Wind-FC
PV Array (kW)	3	0	2	5	0	4
Wind Turbines	0	11	3	0	15	2
Batteries	11	14	7	0	0	0
Converter (kW)	2	2	2	2	2	2
Fuel Cell (kW)	0	0	0	2	2	2
Electrolyzer (kW)	0	0	0	5	4	3
Hydrogen Tank (kg)	0	0	0	6	11	1
Total NPC ($)	42,147	59,274	38,523	90,406	106,506	75,428
COE ($/kWh)	0.667	0.949	0.614	1.451	1.704	1.208
COH ($/kg H_2)	0	0	0	40.7	61.6	43.3
RF	1	1	1	1	1	1

Table 22: Results of the economic analysis of different renewable energy systems at* Yanbu *area

Location	**Yanbu** (Latitude: 24°08' N – Longitude 38° 3' E)					
	System#1	System#2	System#3	System#4	System#5	System#6
	PV-Batt	Wind-Batt	PV-Wind-Batt	PV-FC	Wind-FC	PV-Wind-FC
PV Array (kW)	3	0	2	6	0	4
Wind Turbines	0	9	3	0	13	2
Batteries	11	11	7	0	0	0
Converter (kW)	2	2	2	2	2	2
Fuel Cell (kW)	0	0	0	2	2	2
Electrolyzer (kW)	0	0	0	4	4	3
Hydrogen Tank (kg)	0	0	0	1	6	2
Total NPC ($)	42,147	48,343	38,523	87,788	93,682	77,754
COE ($/kWh)	0.669	0.773	0.609	1.401	1.496	1.231
COH ($/kg H_2)	0	0	0	39.5	52.2	43.1
RF	1	1	1	1	1	1

Table (23) gives a summary of the optimization results at all considered locations. The hybrid system that comprises PV, wind turbines and storage batteries leads to minimizing the cost of energy at all of the considered locations comparing with the other systems. Among all considered locations, Yanbu area has the renewable energy potential to meet the load demand with the minimum COE at 0.609 $/kWh. The optimum configuration at Yanbu comprises 2 kW PV array, 3 wind turbines, 2 kW converter and 7 batteries. On the other hand and for the systems that use the hydrogen production storage system, PV/wind hybrid system at Abha area gives the minimum levelized cost of energy (COE) of 1.208 $/kWh and the cost of the hydrogen production (COH) is 43.1 $/kg. The optimum combination of this system has 4 kW PV array, 2 wind turbines, 2 kW converter, 2 kW fuel cell, 3 kW electrolyzer and 2 kg hydrogen tank. The high COE of the stand alone

renewable energy power generation systems comparing with the grid electricity cost is due the expensive energy storage components. The hydrogen production costs by different renewable energy systems for different locations in the kingdom are shown in Table (24). The results show that the System#4 that comprises PV, fuel cell, electrolyzer, and hydrogen tank, has the least levelized hydrogen cost of production (COH) at all considered locations. The minimum COH is achieved by System#4 at Yanbu with 39.5 \$/kg H_2.

Table 23: Levelized cost of energy at different locations

COE ($/kWh)			**Dhahran**	**Riyadh**	**Jeddah**	**Abha**	**Yanbu**
Category#1	System#1	PV-Batt	0.779	0.671	0.72	0.667	0.669
	System#2	Wind-Batt	0.848	0.761	0.849	0.949	0.773
	System#3	PV-Wind-Batt	**0.702**	**0.612**	**0.616**	**0.614**	**0.609**
Category#2	System#4	PV-FC	1.608	1.513	1.428	1.451	1.401
	System#5	Wind-FC	1.564	1.536	1.615	1.704	1.496
	System#6	PV-Wind-FC	**1.459**	**1.327**	**1.28**	**1.208**	**1.231**

Table 24: Levelized hydrogen cost of production at different locations

COH (\$/kg H_2)		Dhahran	Riyadh	Jeddah	Abha	Yanbu
System#4	PV-FC	**45.4**	**43.2**	**40**	**40.7**	**39.5**
System#5	Wind-FC	57.7	56.2	55.8	61.6	52.2
System#6	PV-Wind-FC	52.9	47.2	45.2	43.3	43.1

4.5 Thermal and Electrical Characteristics of Semi-Conductive Nanofluid

A numerical approach is used to determine thermal and electrical characteristics of solid-liquid mixture prepared by adding different concentrations of carbon nanotubes (CNT) in to the water or a carrier fluid. The simulations cover a range of CNT concentrations in the carrier fluid including; 0.5%, 1%, 1.5%, 2%, 2.5% and 3%. The general description of the numerical study and the boundary conditions are explained in this section for 1% CNT in water mixture. However, same explanation can hold for other concentration ratios. The water properties are considered to be functions of temperature whereas the properties of CNT, (listed in Table (9)), are considered to be independent of temperature in the range of temperatures used in the present study.

Figure (48a) shows a microscopic image, obtained from the experiment, for 1% CNT added to water. The image is converted to a gray scale, (Figure 48b) and it is, then, meshed in multi-physics solver, (Figure (48c)). Figure (48d) shows the mesh quality at a selected location. The dimensions of the computational domain are shown in the meshed images. Mesh independence test is conducted to ensure that the mesh size does not affect the predictions by monitoring the specific heat at constant pressure and varying the mesh size. The findings are shown in Figure (49). It is observed from this figure that the mesh size does not have an effect on the simulation results since specific heat capacity predicted as a function of temperature overlaps for all the mesh sizes incorporated. The mesh size of 67040 cells (Grid 4) is selected to accomplish further simulations.

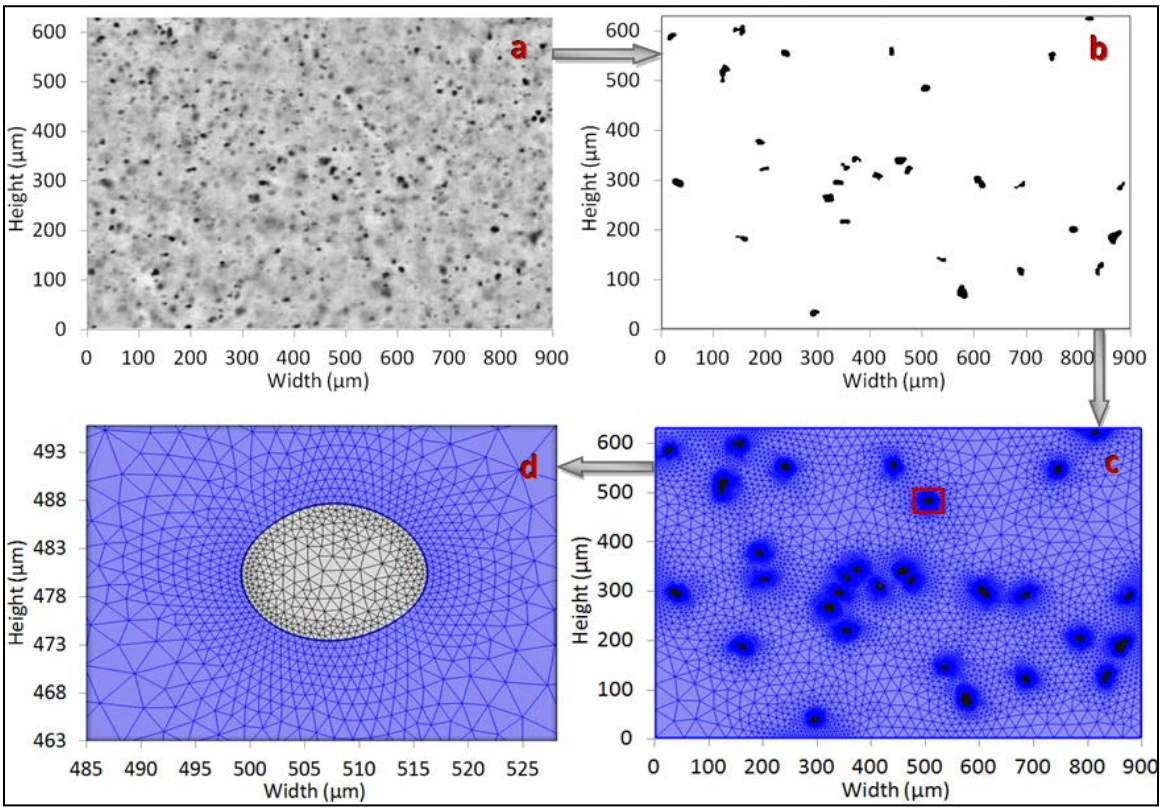

Figure 48: Micro image as obtained from the optical microscope with 1% concentration of CNT in water (a), converted to black and white (b), and meshed multi-physics solver (c), with 67040 cells. (d) shows the mesh at a selected location

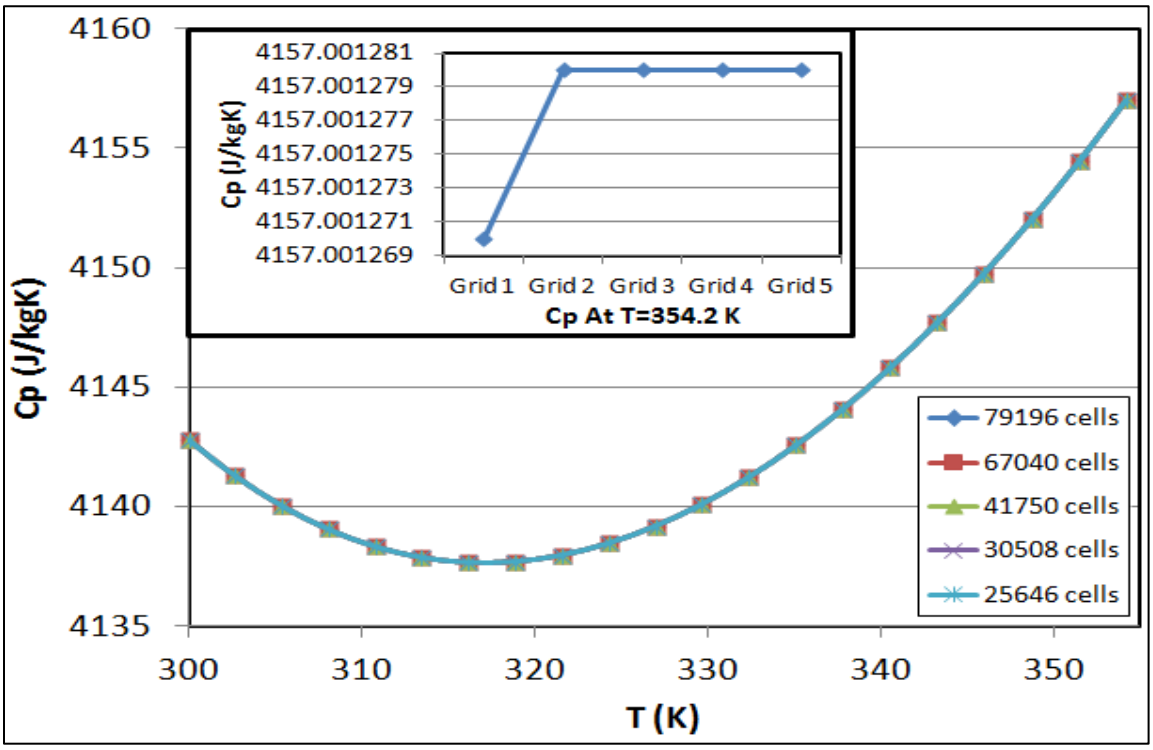

Figure 49: Mesh independence test results

The boundary conditions that are used in the simulations to determine the effective density and thermal conductivity of the water-CNT mixture are shown in Figure (50). Temperature boundary conditions are given on the left and right edges, whereas, thermal insulation boundary conditions are considered on the top and the bottom edges of the computational domain. Temperature difference is specified as 2 K along x –axis and the mean effective density and thermal conductivity are predicted at the mean temperature. The influence of increasing the mean temperature on the mixture effective density and thermal conductivity is investigated by varying the temperatures at the left and right edges of the solution domain. The same computational domain can be used to determine the mean effective specific heat capacity of the mixture. In this case, transient simulation is considered and thermal insulation boundary conditions are specified at all edges except at the left edge where heat flux boundary condition is adapted, which is similar to those used in calorimeters [93]. In addition, it is important to investigate the effect of adding CNT to the water on its electrical characteristics. The mean effective electrical conductivity can be determined using the same computational domain, but this time using electrical insulation boundary conditions on the top and bottom surface and electrical potential boundary condition on the left and right edges of the solution domain. In this case, electric currents model is used sequentially after the heat transfer model solution. This arrangement provided information about the effect of temperature on the electrical characteristics of the nanofluid.

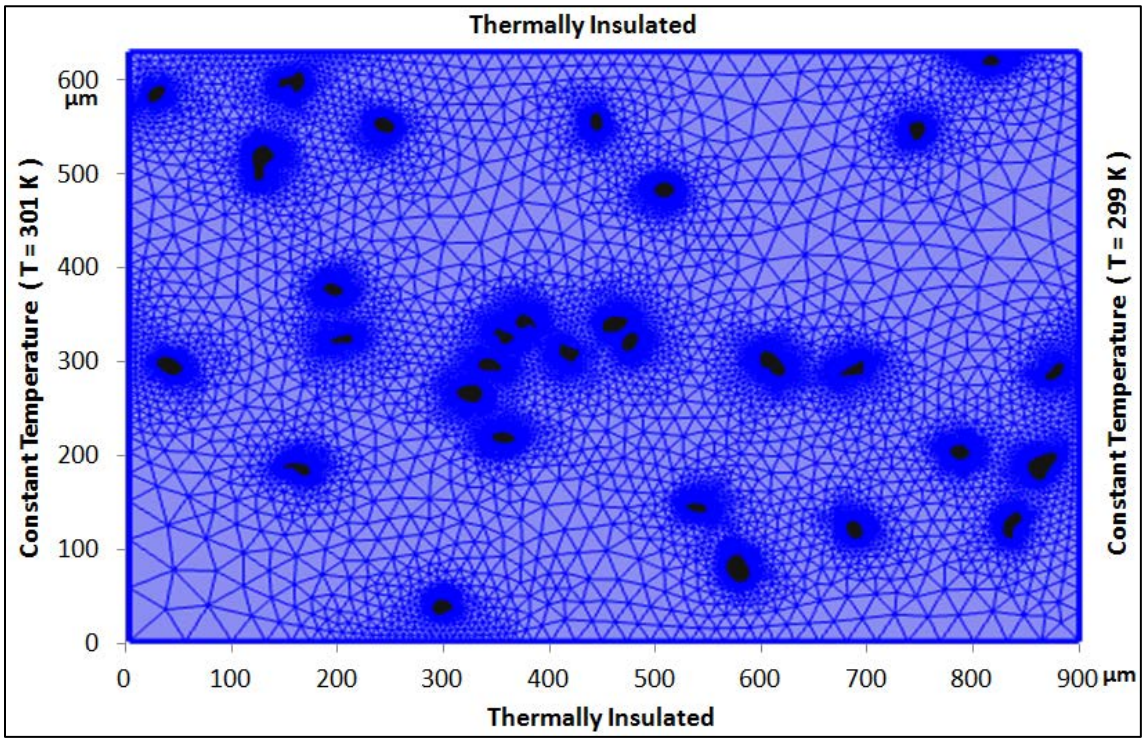

Figure 50: The solution domain and the boundary conditions used to determine the effective density and thermal conductivity. The solution domain comprises carbon nanotubes added to water

4.5.1 Experiment and Validation

An experiment was carried out to examine the thermal and electric characteristics of the deionized water-CNT mixture with 1% CNT concentration. The specific heat capacity was measured using a Differential Scanning Calorimeter (DSC), model DSCQ2000 [93]. The sequence used in the determination was as follows: isotherm of 5 minutes at 25˚C, dynamic ramp with heating rate of 1˚C/min from 25˚C to 70˚C and isotherm of 5 minutes at 70˚C. As a consequence of the nature of the sample (liquid-solid mixture) a crucible hermetic pan was used in order to avoid loss of material by evaporation. The measurements were repeated three times to ensure the repeatability the data and error estimation. The error estimated from the experiment was in the order of 5%.

In parallel with the experiment, numerical simulation is carried out to predict the effective specific heat capacity as function of temperature in line with the experimental conditions. A comparison between the experimental and numerical results at 1% CNT concentration ratio in water is shown in Figure (51). It is observed that both results are in good agreement. The small differences are because of the experimental error and the error related to the numerical simulations such as truncations error.

YSI (Yellow Springs Instrument Co.), model 35 [94], conductance meter was used to measure the effective electrical conductivity in which, the ratio of current to voltage was considered for a conductivity cell immersed in the water-CNT mixture. The mixture was heated from 300K up to 305K while measuring the electrical conductivity.

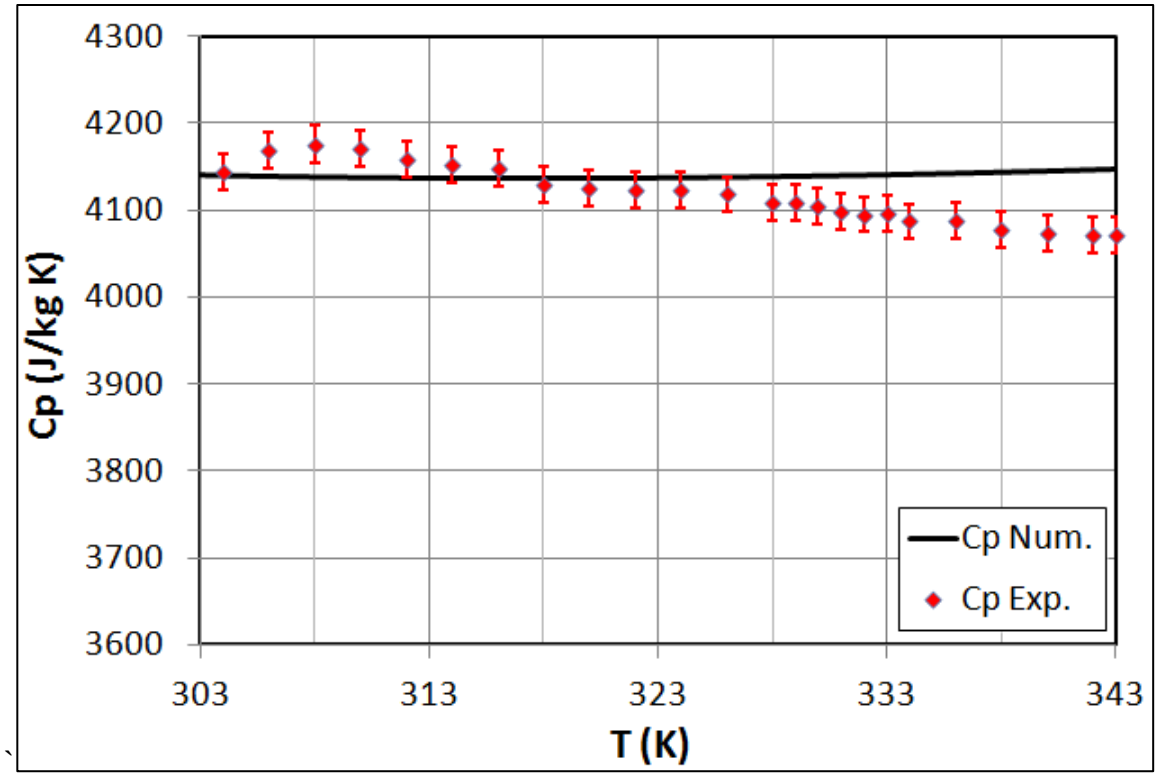

Figure 51: Experimental and numerical results comparison of the effective specific heat capacity of the nanofluid as function of temperature at 1% CNT concentration ratio in water

The electrical conductivity measurements were repeated three times to ensure the repeatability and the average values were considered. The error estimated based on experimental repeatability is in order of 4%. The experimental conditions and the temperature range were incorporated in the numerical simulations to predict the effective electrical conductivity. Figure (52) shows comparison of the experimental and numerical results for the nanofluid effective electrical conductivity as function of temperature at 1% CNT concentration ratio in water. It is evident that the experimental and numerical results are in good agreement.

4.5.2 Effective Properties of the Nanofluid

The influence of CNT concentration on the effective thermal and electrical properties of the water-CNT mixture is investigated. The numerical study is carried out incorporating microscopic images obtained from the experiment that represent the actual distribution of different concentration ratios of CNT in water. Different cases with the appropriate boundary conditions are considered to determine the corresponding thermal and electrical properties. The effect of changing temperature and CNT concentrations on the effective thermal and electrical properties are also investigated.

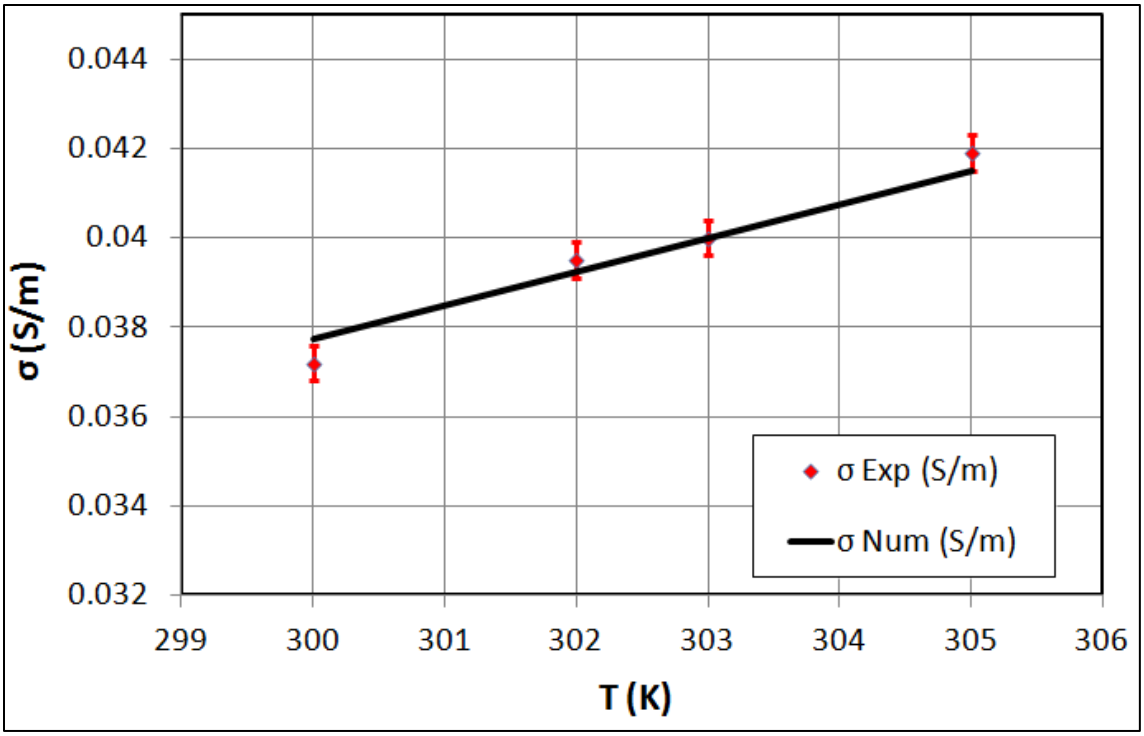

Figure 52: Experimental and numerical results comparison of the effective electrical conductivity of the nanofluid as function of temperature at 1% CNT concentration ratio in water

4.5.2.1 Effective Density and Thermal Conductivity

The effective density and effective thermal conductivity of the water-CNT mixture are predicted numerically incorporating temperature difference along the x-axis in the computational domain. The resulting thermal properties are evaluated on the base of the average temperature in the solution domain. To investigate the effect of temperature change on the effective density and effective thermal conductivity, the previously described procedure is repeated via changing the temperature boundary conditions and simulating different cases for temperature ranging from 300 up to 320 K. The boundary conditions that are shown in Figure (50) are for the case where temperature boundary conditions of 301K and 299K which are specified on the left and right edges, respectively. The effective density and effective thermal conductivity predicted for this case are based on the average temperature of 300K. Figure (53) and (54) show temperature and density contours in the solution domain for 1% CNT in water mixture, respectively. Temperature contours and the heat flux vectors, represented in arrows, are shown in Figure (55). The arrows indicate that the heat flux attains high values near the CNT particles. This can also be observed from Figure (56) which shows magnified contours of heat flux at two selected locations where high heat flux concentration occurs at the boundaries of the CNT particles. This behavior is associated with higher thermal conductivity of CNT as compared to that of the water. Effective density of the mixture can be calculated using the mass based analysis, (Equation (3.35)).

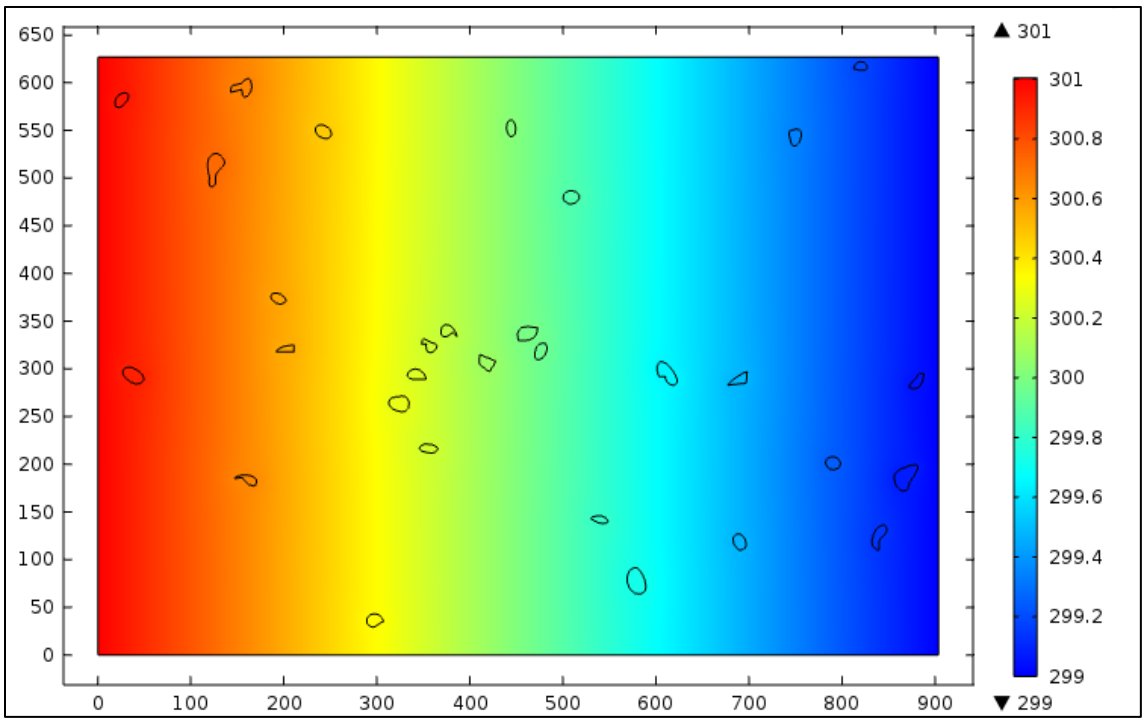

Figure 53: Temperature (K) contours in the solution domain for 1% CNT in water mixture

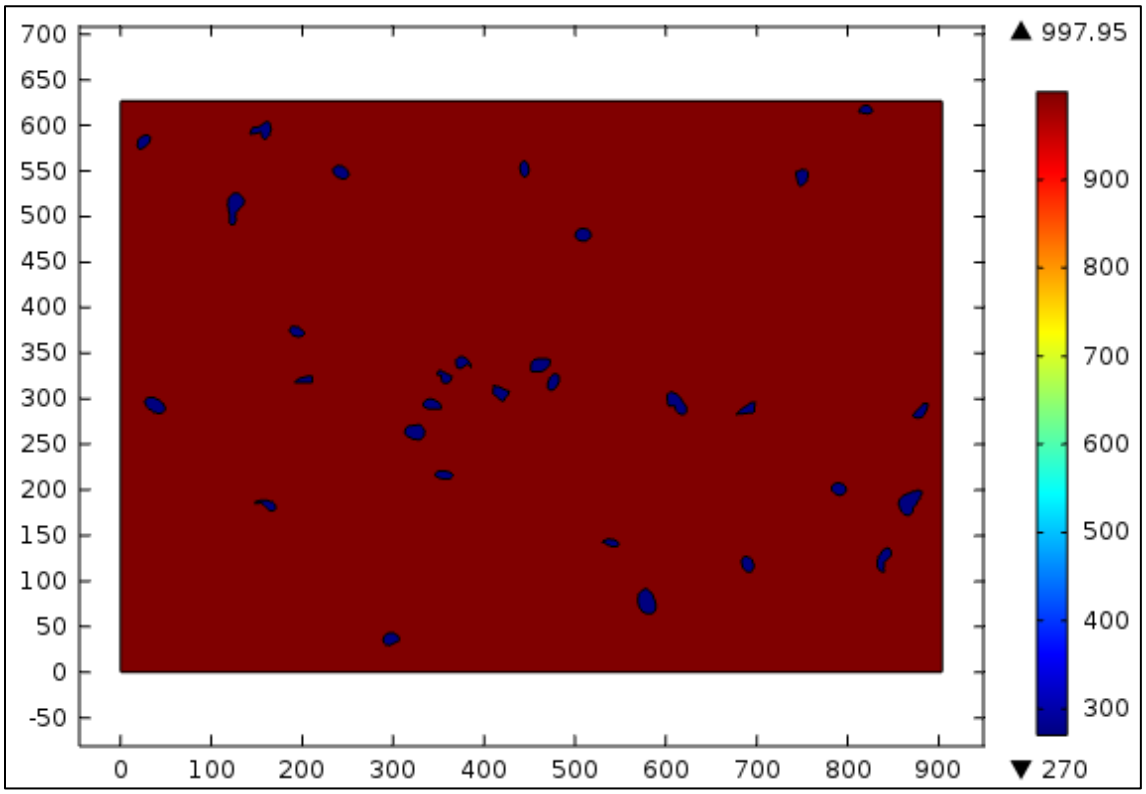

Figure 54: Density (kg/m^3) contours in the solution domain for 1% CNT in water mixture

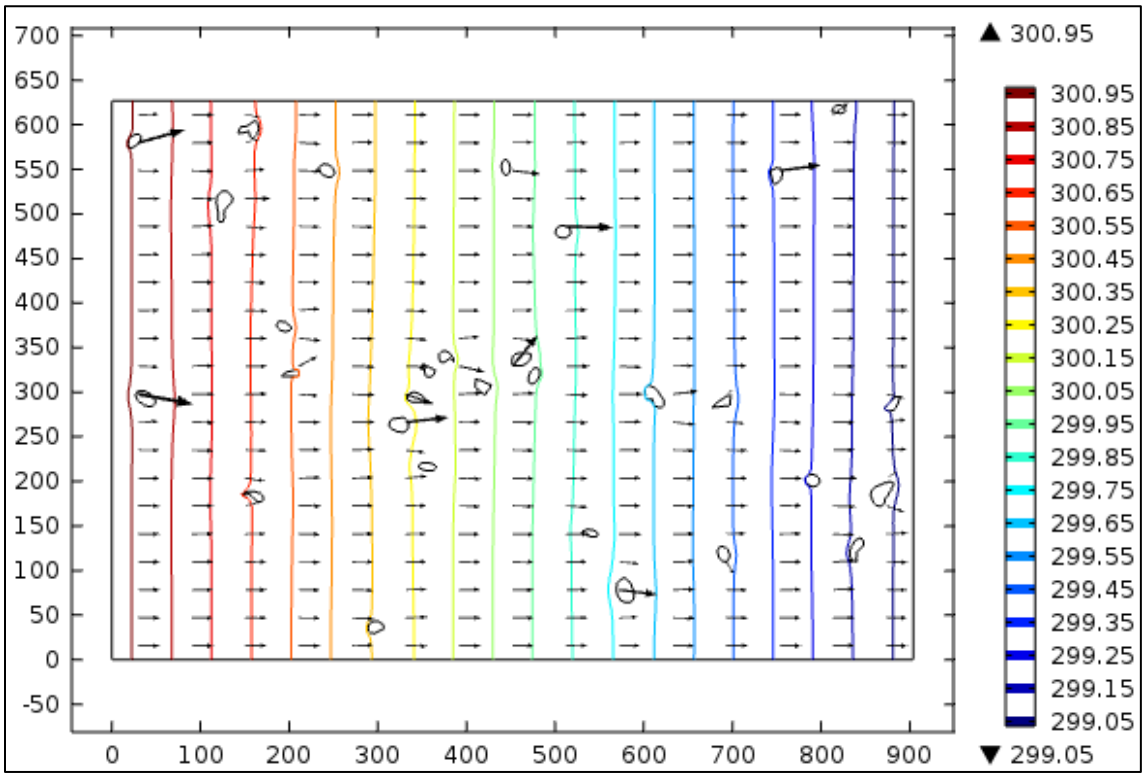

Figure 55: Arrow field of the total heat flux plotted on contours of temperature distribution

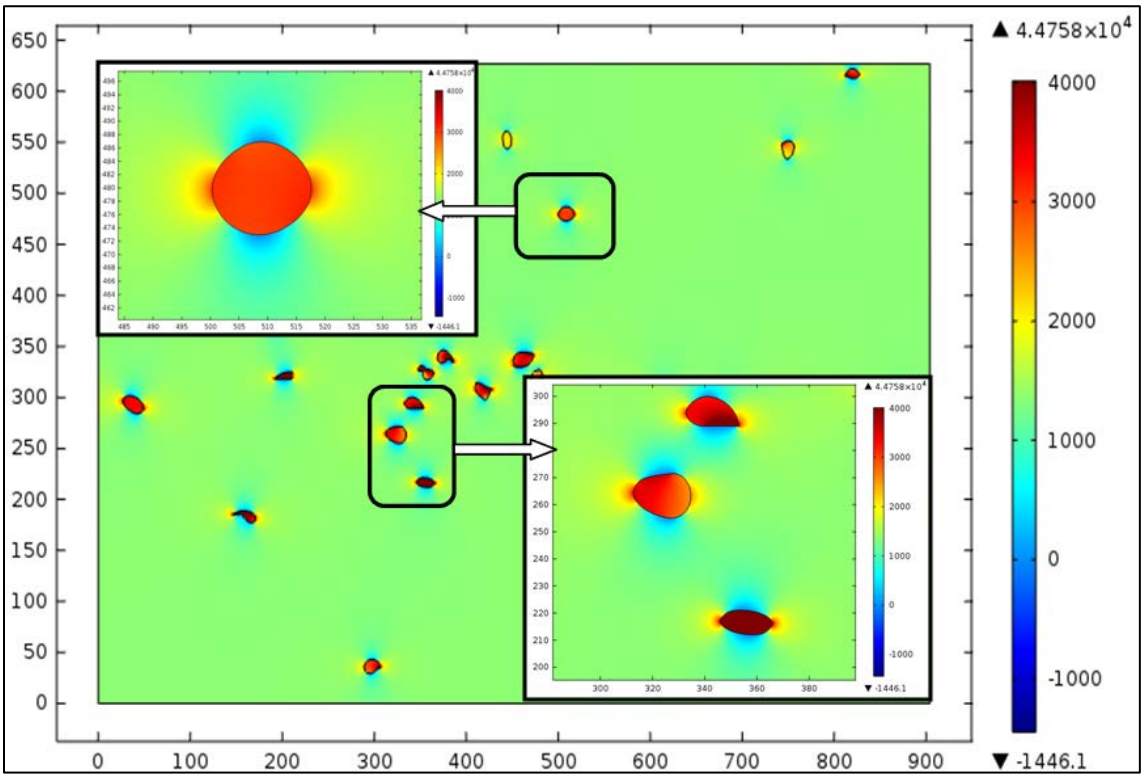

Figure 56: Contours of x-direction heat flux (W/m^2) magnified at two selected locations

Figure (57) shows the numerical predictions of the effective density of the mixture as a function of temperature for different CNT concentrations in the water mixture. The density of the mixture decreases as bulk temperature increases. The density of the CNT is 270 kg/m^3 [85], which is less than the density of the water. Therefore, increasing CNT concentration leads to decrease in the effective density of the mixture. It is evident that the relation between the effective density and temperature is linear for all concentration ratios within the range of temperatures considered, as shown in Figure (57). Therefore, a curve fitting technique is adopted to obtain a mathematical expression for the effective density of the mixture as a function of CNT concentration. The effective density for all concentrations can be calculated from:

$$\frac{\rho_{eff}}{\rho_o} = b_o + m\frac{T}{T_o} \tag{4.1}$$

where

$$b_o = -0.000288\,(c) + 1.108142 \tag{4.2}$$

$$m = 0.000287(c) - 0.108008 \tag{4.3}$$

$$\rho_0 = -6.990138\,(c) + 997.109139 \tag{4.4}$$

In the above equations, *c* is the percentage of volume concentration multiplied by 100 and T_o is 300K.

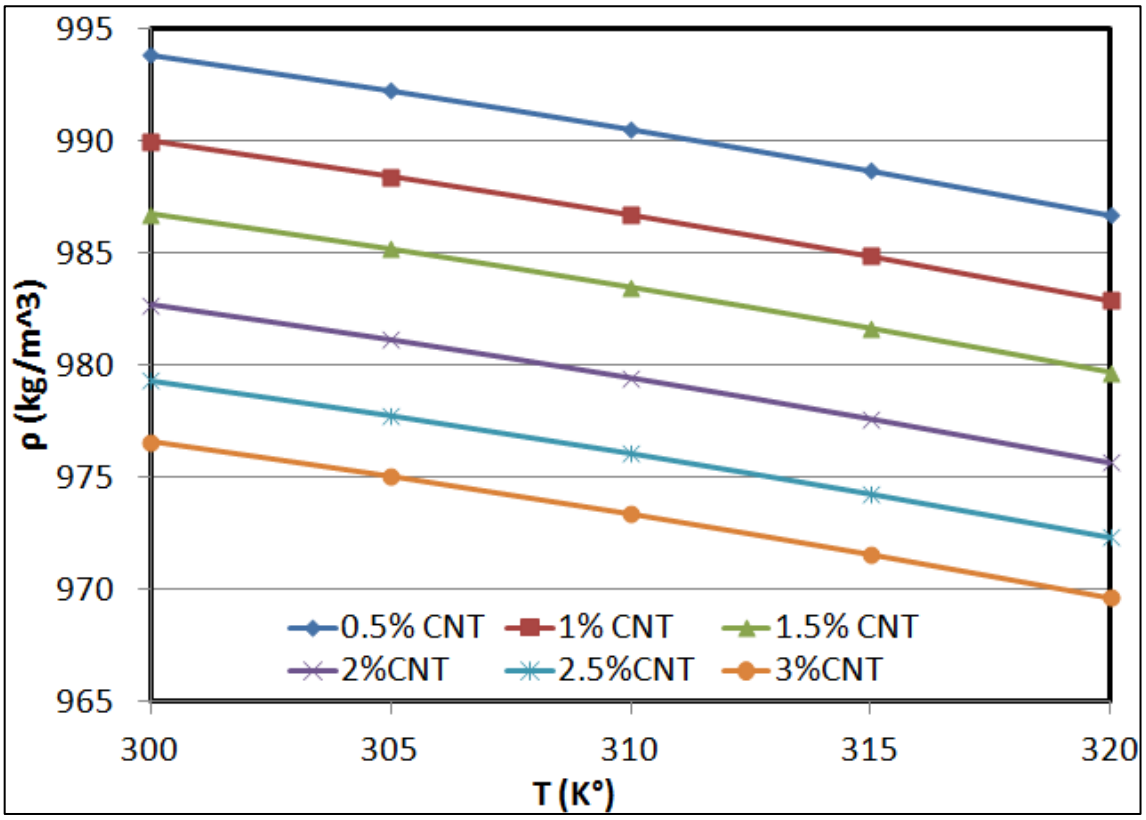

Figure 57: The effective density of the nanofluid as function of temperature at different CNT concentration ratios in water

Figure (58) shows the numerical and mass based predictions of the effective density of the mixture as function of temperature for different CNT concentrations in the water mixture. It is clear from Figure (58) that good agreements are achieved between both results and the percentage of the error is less than 0.01 %.

The effective thermal conductivity is determined using the heat flux along the x-axis, temperature difference and the width of the computational domain. The results of mean effective density and effective thermal conductivity for different temperatures with 1% CNT in water mixture are given in Table (25). Furthermore, mass based calculation of the effective thermal conductivity is given for the comparison reason with the simulation results. It should be noted that experimental conditions are simulated to obtain the thermal conductivity. It is evident that the effective thermal conductivity determined from the mass base calculations is significantly higher than that of the simulations. This is because that CNT has a very high thermal conductivity value, (3000 W/mK, [87]) comparing with water, (0.613 W/mK at 300 K). Since carbon nanotubes are not well connected in the water, heat conduction is suppressed by the water located in between carbon nanotubes in the solution domain. For this reason, large difference is observed between the thermal conductivities determined from the mass based analysis and the simulations. Therefore, utilizing mass based analysis to predict the effective mean thermal conductivity leads to erroneous values of the thermal conductivity.

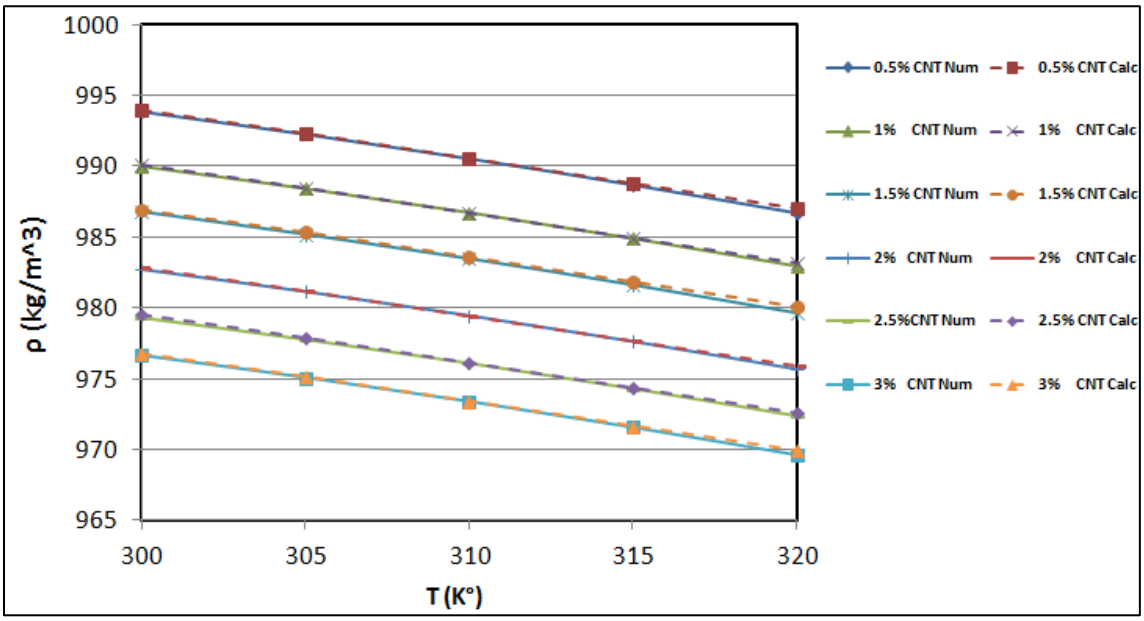

Figure 58: Numerical results and mathematical expression calculated predictions using (Eq. 4.1) of the effective density of the nanofluid as function of temperature at different CNT concentration ratios in water

Table 25: Effective density and effective thermal conductivity determined from mass based analysis and from multi-physics code incorporating micro-images

1%CNT	Density (kg/m^3)	Thermal Conductivity (W/mK)	
T (K)	Mass Based	Mass Based	Virtual Experiment
300	989.999	32.116	0.6181
305	988.420	32.124	0.6261
310	986.709	32.131	0.6336
315	984.866	32.138	0.6407
320	982.890	32.145	0.6473

Figure (59) shows the effective thermal conductivity of the nanofluid as a function of temperature for different CNT concentration ratios in the water. The effective thermal conductivity of the mixture increases with increasing temperature. In addition, the effective thermal conductivity of the mixture enhances by increasing the CNT concentration due its higher thermal conductivity as compare to the water. One can observe from Figure (59) that the relation between the thermal conductivity and the temperature is linear for all concentrations ratios within the temperature range considered. A linear curve fitting relation can be adopted to obtain a mathematical expression for the effective thermal conductivity of the mixture as a function of the CNT

concentration. The effective thermal conductivity with CNT concentration can be written as:

$$\frac{k_{eff}}{k_o} = b_o + m\frac{T}{T_o} \tag{4.5}$$

where

$$b_o = 0.00001\ (c) + 0.292257 \tag{4.6}$$

$$m = -0.00001\ (c) + 0.708441 \tag{4.7}$$

$$k_o = 0.014039\ (c) + 0.603742 \tag{4.8}$$

Figure (60) shows numerical predictions and results of curve fitting for the effective thermal conductivity as function of temperature of the mixture and different CNT concentration ratios in the water mixture. A good agreement is observed and the data plotted reveals that the error calculated from the linear equation is less than 0.05 %.

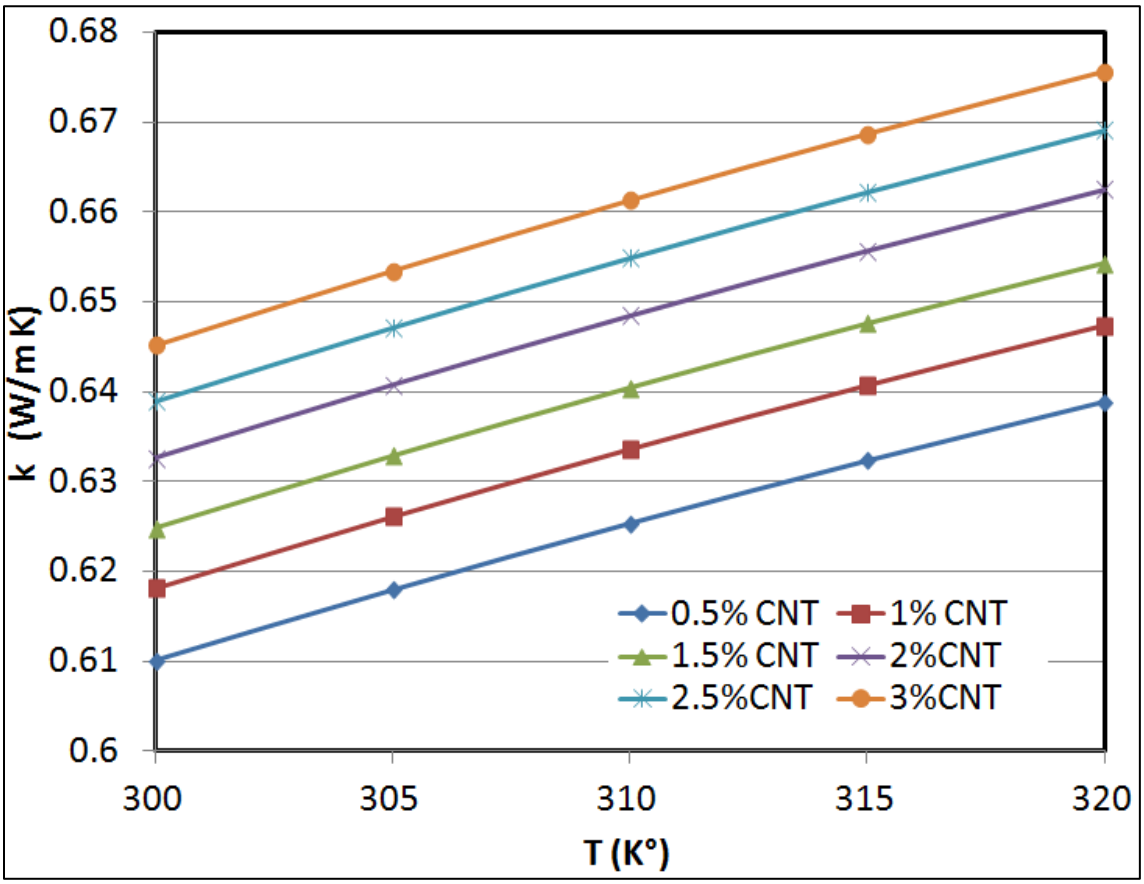

Figure 59: The effective thermal conductivity of the nanofluid as function of temperature at different CNT concentration ratios in water

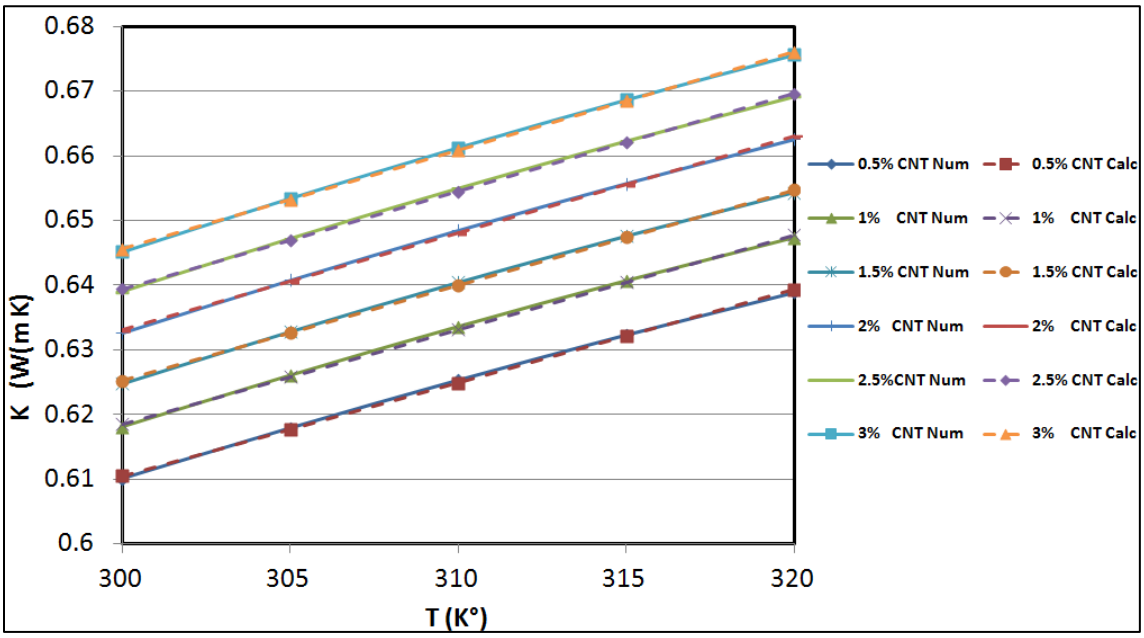

Figure 60: Numerical results and mathematical expression calculated predictions using (Eq. 4.5) of the effective thermal conductivity of the nanofluid as function of temperature at different CNT concentration ratios in water

4.5.2.2 Effective Specific Heat Capacity

The effective specific heat capacity of the water-CNT mixture is determined numerically through a transient analysis. Figure (61) shows the solution domain and the relevant boundary conditions. In this case, thermal insulation boundary conditions are specified at all edges except at the left edge where the heat flux boundary condition of 10 kW/m^2 is introduced. Temperature dependence of the effective specific heat capacity of the mixture for different CNT concentrations in the water mixture is shown in Figure (62). The specific heat capacity increases with increasing temperature and decreases with increasing CNT concentration due to the lower specific heat capacity of CNT as compared to that of the water. Incorporating a second order polynomial curve fitting for these curves makes it possible to obtain a mathematical relation for the effective specific heat capacity of the mixture as a function of the CNT concentration. The effective specific heat capacity for various concentrations can be determined from:

$$\frac{Cp_{eff}}{Cp_o} = a\left(\frac{T}{T_o}\right)^2 + b\left(\frac{T}{T_o}\right) + d \tag{4.9}$$

Where

$$a = -0.0013\,(c) + 0.3172 \tag{4.10}$$

$$b = 0.0027\,(c) - 0.6716 \tag{4.11}$$

$$d = -0.0015\,(c) + 1.3543 \tag{4.12}$$

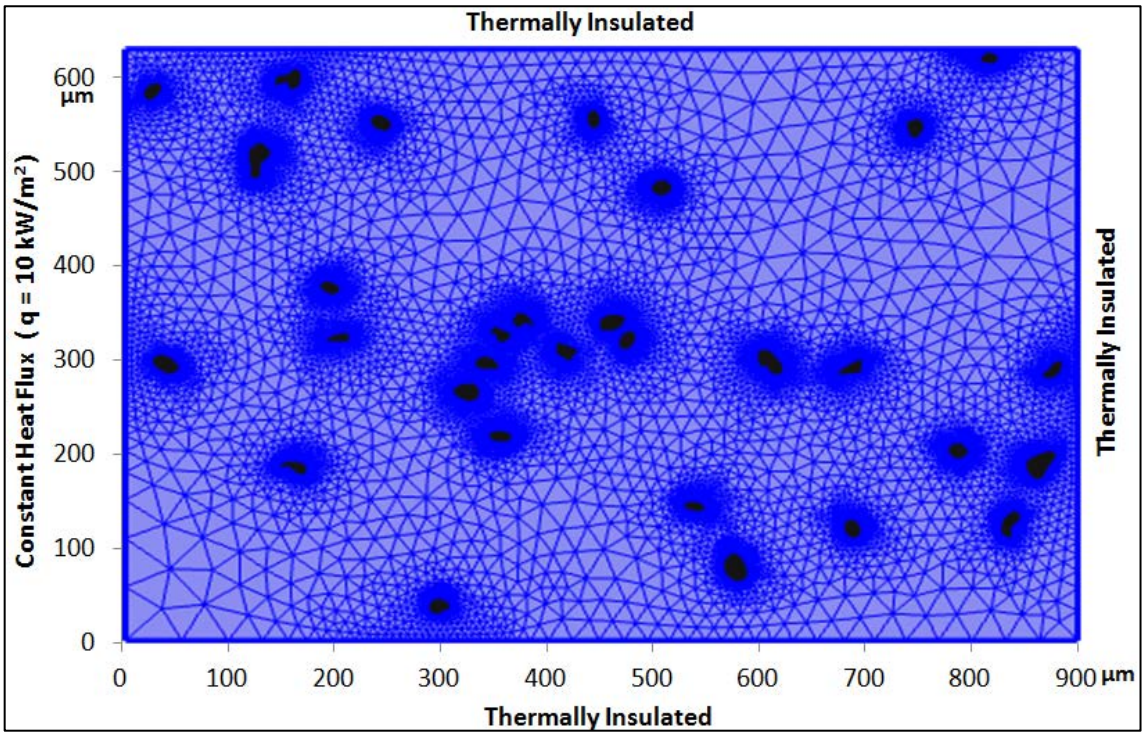

Figure 61: The solution domain and the boundary conditions used to determine the effective specific heat capacity

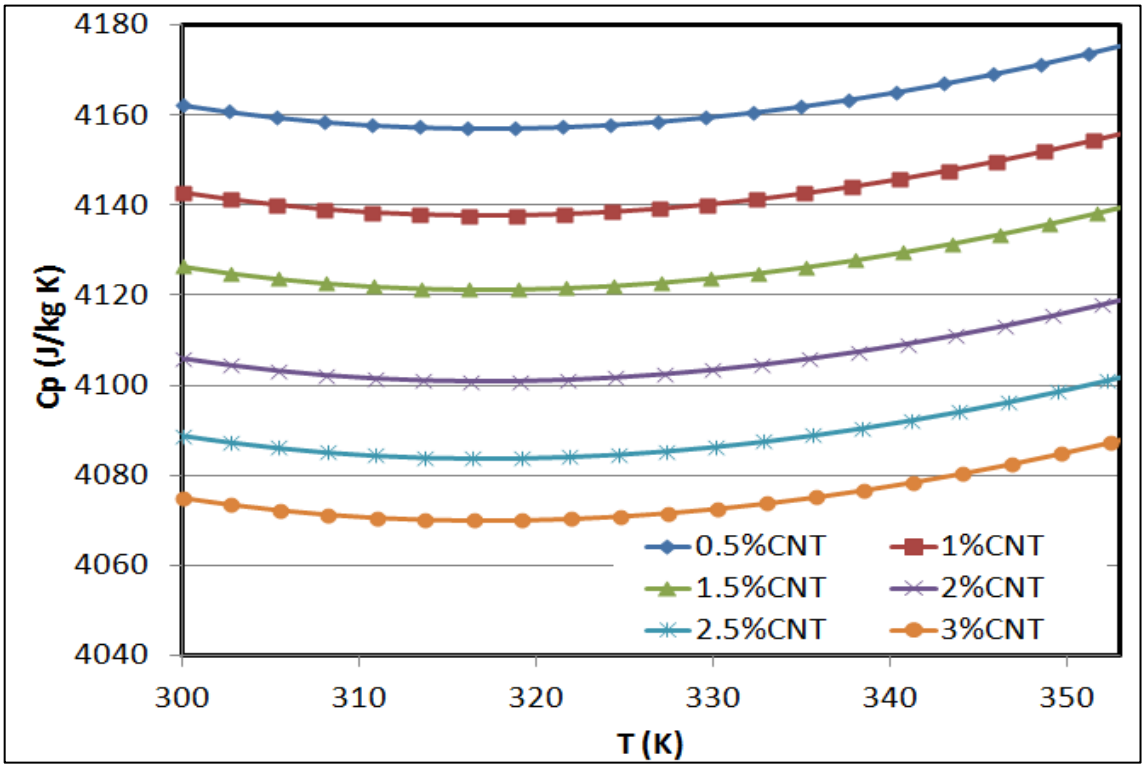

Figure 62: The effective specific heat capacity of the nanofluid as function of temperature at different CNT concentration ratios in water

A comparison between the predictions and the results of equation of the curve fitting for temperature dependent effective specific heat capacity of the mixture due to different CNT concentrations in the water is shown in Figure (63). It is observed that a good agreement is achieved via using the equations of the curve fitting and the error is less than 0.0108%.

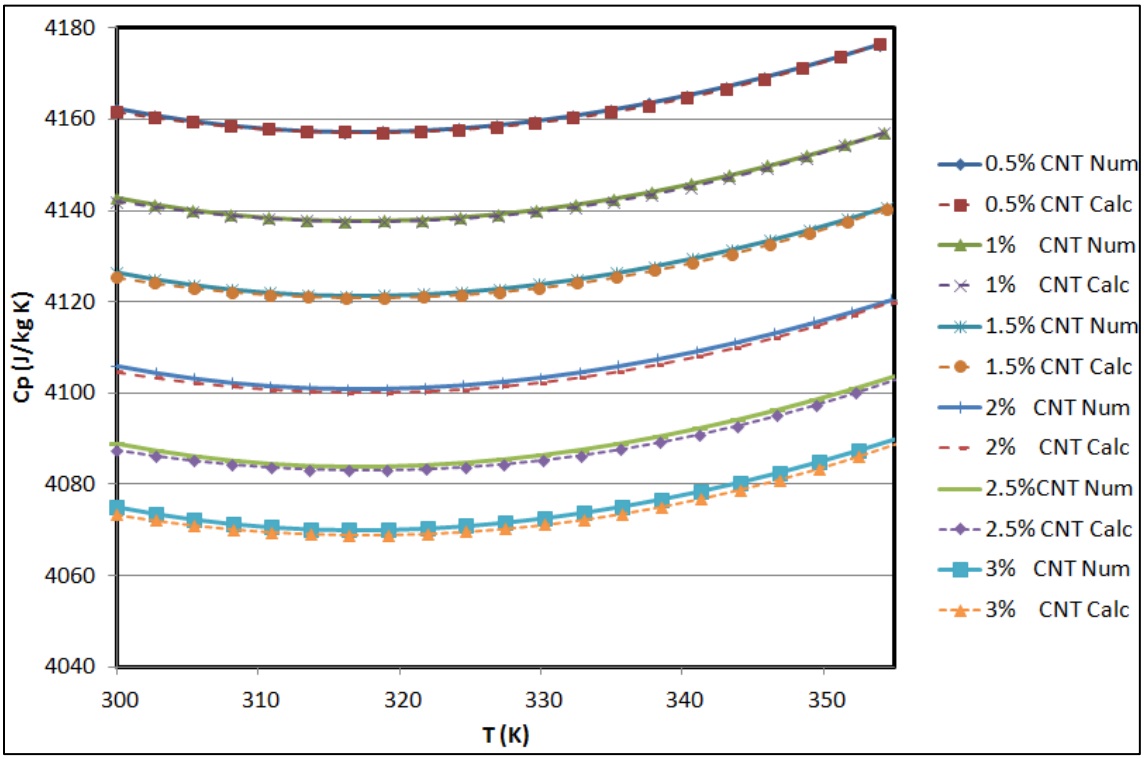

Figure 63: Numerical results and mathematical expression calculated predictions using (Eq. 4.9) of the effective specific heat capacity of the nanofluid as function of temperature at different CNT concentration ratios in water

4.5.2.3 Effective Electrical Conductivity

The effects of the temperature and the CNT concentrations in the water-CNT mixture on the effective electrical conductivity of the mixture are predicted using COMSOL multi-physics code [3]. The influence of temperature on the effective electrical conductivity is also incorporated sequentially. Therefore, the simulation of each case provides the effective electrical conductivity for the corresponding mean temperature obtained from the numerical heat transfer simulations. This procedure is repeated to cover the ranges of CNT concentrations in the water mixture. Figure (64) shows the computational domain and the boundary conditions which are used to simulate the effective electrical conductivity. Electric potential boundary conditions are specified at the left and the right edges as 2 Volts and 1 Volt, respectively. This leads to 1 Volt electrical potential difference along the x-axis as similar to those used in thermal conductivity experiments. On the other hand, electric insulation boundary conditions are specified at the top and the bottom edges of the solution domain.

The contours of the electrical potential for 1% CNT in water mixture is shown in Figure (65) while Figure (66) shows contours of current density along the x-axis magnified at two selected locations. It should be noted that electrical conductivity of CNT is significantly higher as compare to that of the water. Consequently, high current density is observed in Figure (66) for the CNT particles vicinity.

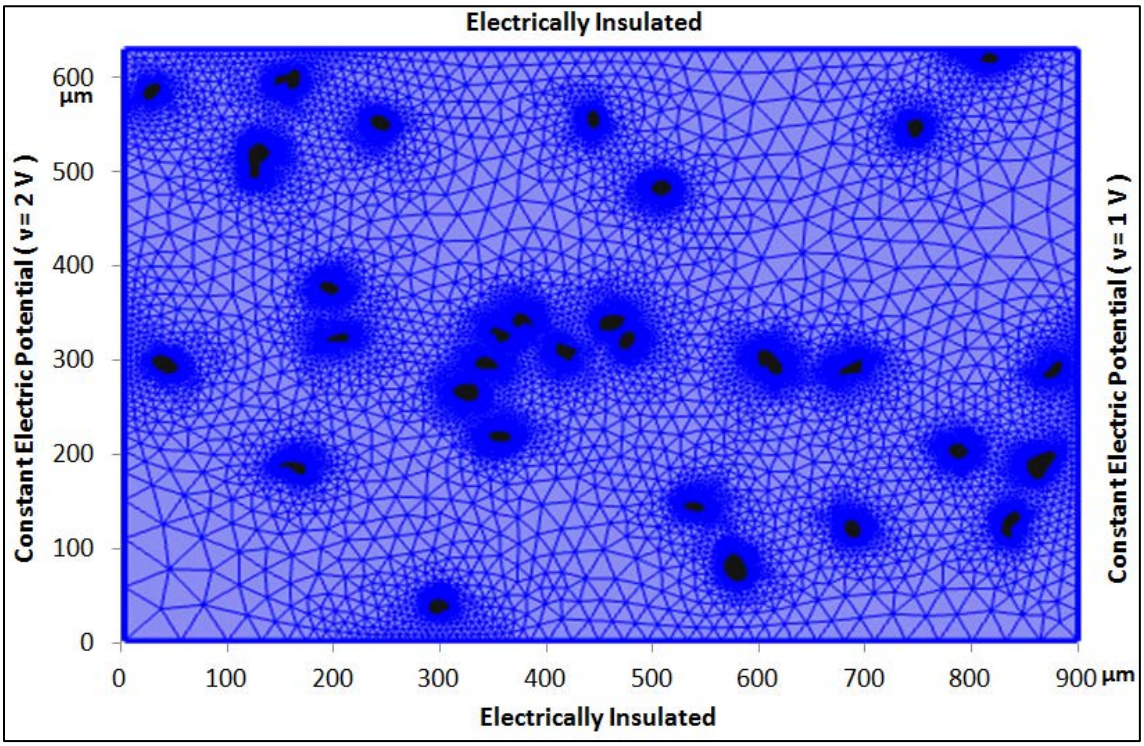

Figure 64: The solution domain and the boundary conditions used to determine the effective electrical conductivity

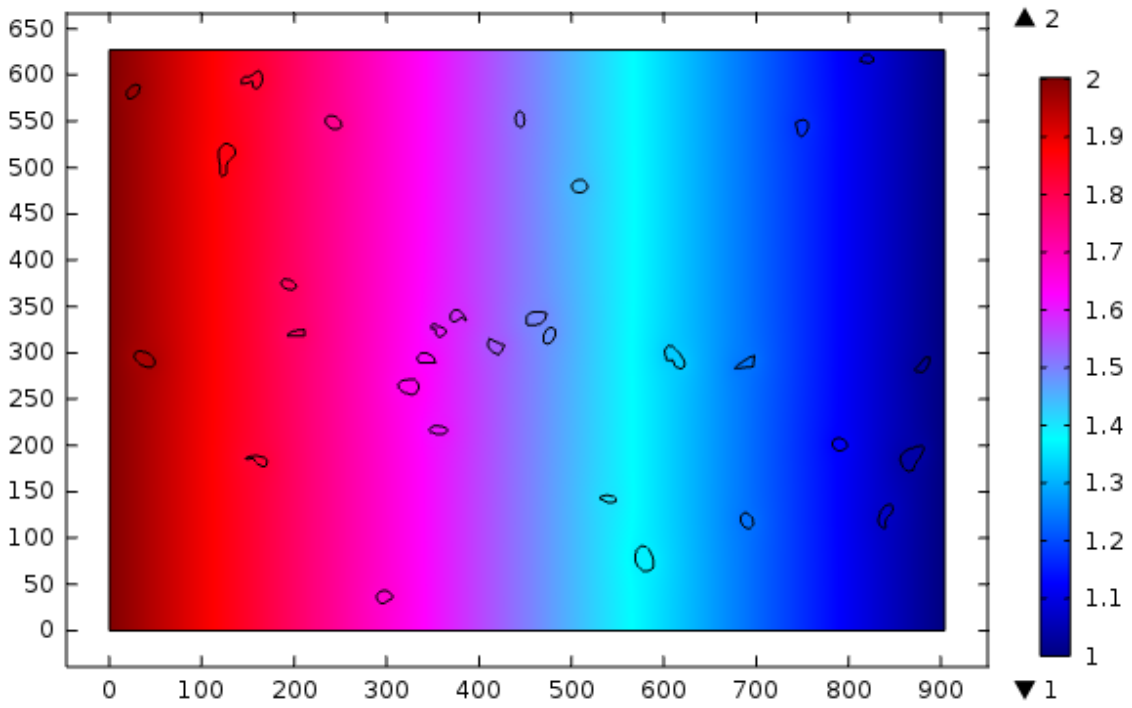

Figure 65: Electrical potential contours (Volts) in the solution domain for 1% CNT in water mixture

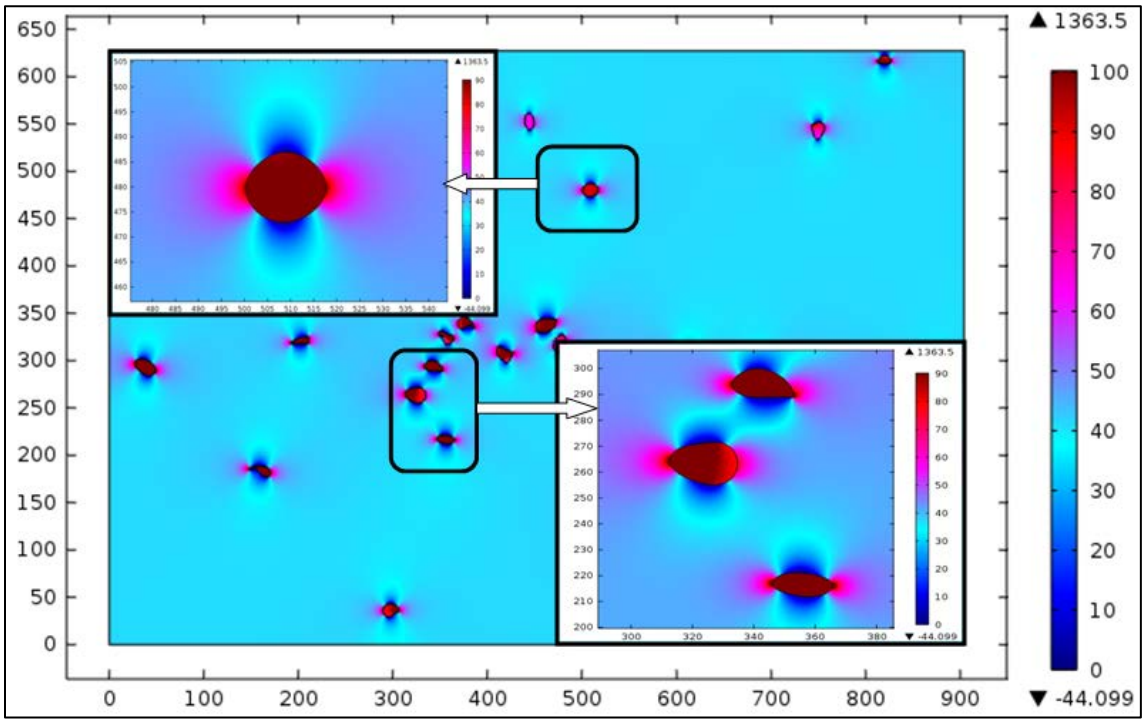

Figure 66: Contours of x-direction current density in (A/m^2) magnified at two selected locations

Figure (67) shows temperature dependence of the effective electrical conductivity of the nanofluid for different CNT concentrations in the water mixture. It is evident from Figure (67) that the effective electrical conductivity increases with temperature. Furthermore, increasing CNT concentrations in the water mixture enhances the electrical conductivity of the mixture. Since the variation is linear, the linear curve fitting is introduced between the effective electrical conductivity and temperature for all considered CNT concentration ratios. The following equation can be used to determine the effective electrical conductivity as a function of the CNT concentrations.

$$\frac{\sigma_{eff}}{\sigma_0} = -5 + 6\frac{T}{T_0} \tag{4.13}$$

where σ_0 is the electrical conductivity at the base temperature T_o = 300 K.

It is evident that the variation of the effective electrical conductivity with CNT concentration is small as shown in Figure (67). The dependence of the effective electrical conductivity on the CNT concentration is not significant; however, it is dependence on temperature is considerable. Since the effect of the CNT concentration is not considerable, only 0.5% CNT concentration is presented for the comparison of electrical conductivity obtained from mass based analysis (Equation (3.38)) and the numerical predictions in Figure (68). The comparison between the effective electrical conductivity findings in Figure (68) shows that good agreement is observed with the percentage error of less than 0.001%.

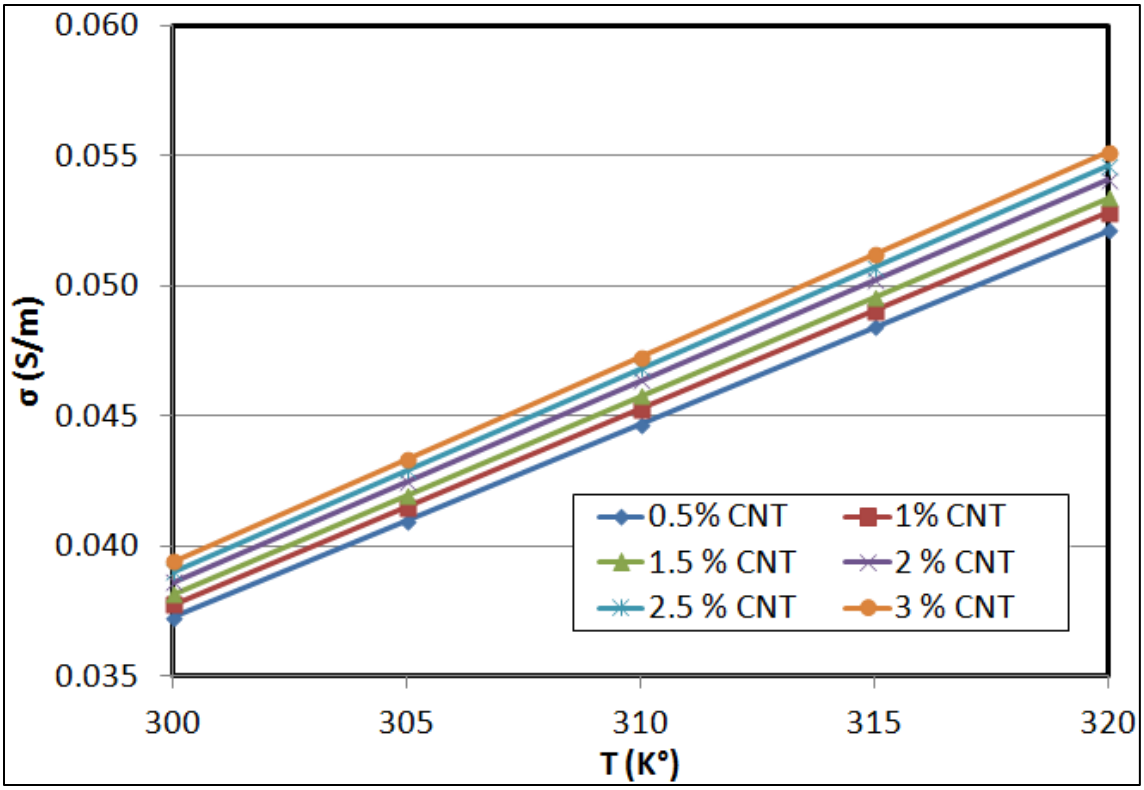

Figure 67: The effective electrical conductivity of the nanofluid as function of temperature at different CNT concentration ratios in water

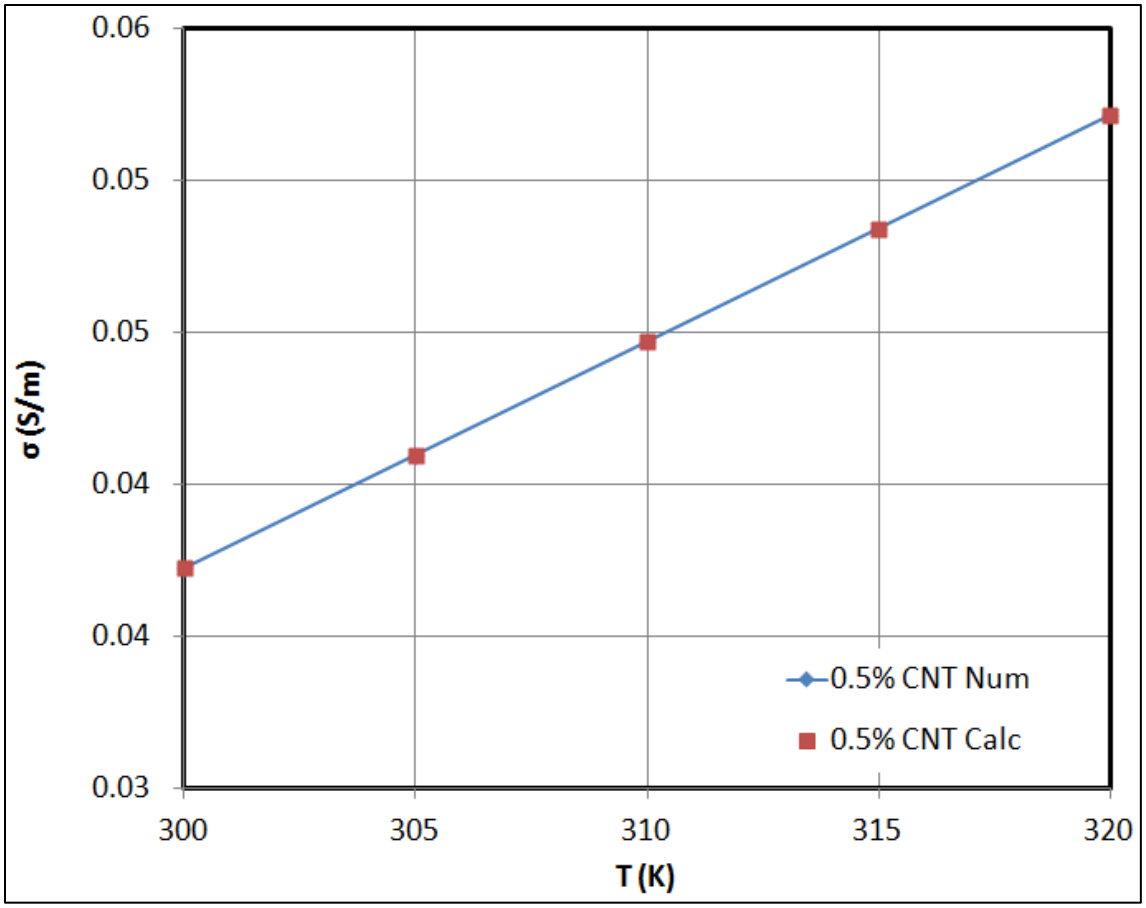

Figure 68: Numerical results and mathematical expression calculated predictions using (Eq. 4.13) of the effective electrical conductivity of the nanofluid as function of temperature at 0.5% CNT concentration ratio in water

4.6 Hydrogen Production via electrolysis incorporating CNT-Water Nanofluid and Industrial Waste Water

In this dissertation, the potential of hydrogen production via electrolysis process is investigated experimentally. A nanofluid and waste water were used in the electrolyzer for possible hydrogen production enhancement. 16 Volts and 10 Volts electrical potentials were applied and the current was 0.01 Ampere for both nanofluid and wastewater electrolysis, respectively. The voltage potential was applied for 30 seconds and the accumulated gas in the electrolyzer was injected to the gas chromatograph. Agilent technologies 7890b Gas Chromatograph (GC) system [95] was used to characterize the hydrogen content in the injected gas samples (Figure (69)). Figure (70) shows a schematic diagram for the hydrogen production and characterization system.

The efficient operation of the electrolysis system for hydrogen production is associated with the electrodes, electrolytic solution, and current-voltage characteristics of the power supply unit. One of the challenges is to increase hydrogen production while incorporating waste water from the food industry. This is because of the fact that the waste water from the food industry contains significant amount of hydrocarbons, which can be utilized for the hydrogen production [96].

Figure 69: Agilent technologies 7890b Gas Chromatograph (GC) system

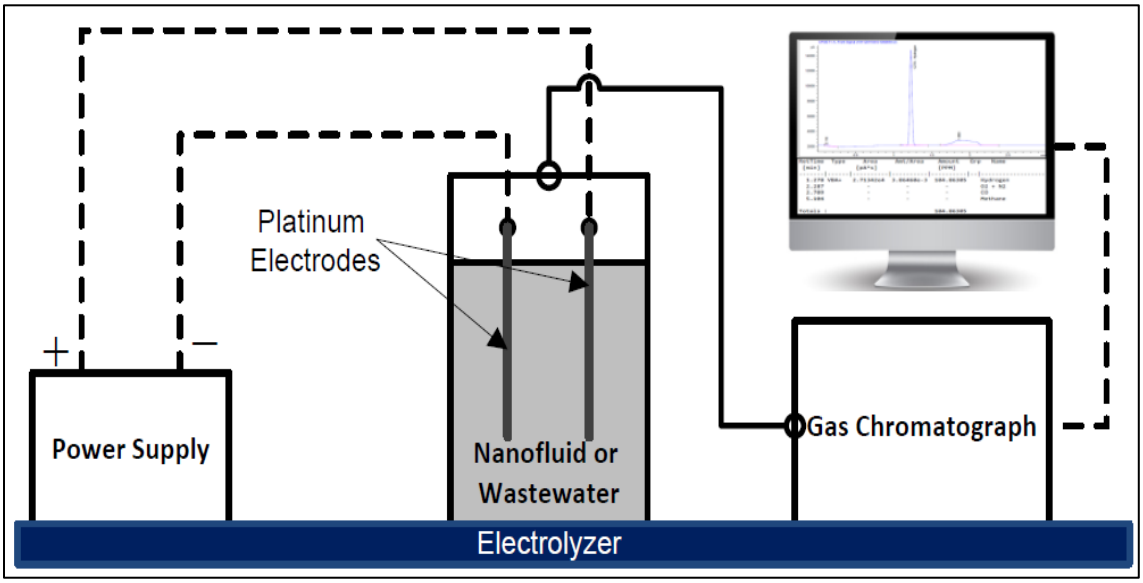

Figure 70: A Schematic Diagram for the hydrogen production and characterization system

Due to low electrical conductivity of the some of the waste water, the energy consumed through electrolysis remains high, which lowers the overall efficiency of the system. Introducing acidic or alkaline medium in the waste water enhances electrical conductivity; however, it has an adverse effect on the electrodes, for example, the presence of alkaline solution gives rise to half reaction at the anode ($4OH^- \rightarrow O_2 + 2H_2O + 4e^-$) because of the poor electrolysis of hydroxyl ions to oxygen at anode [97]. In this case, high potential is necessary to achieve the reactions at reasonable high rates. Therefore, the occurrence of over-potential at anode and ohmic losses in the electrolytic solution reduce the hydrogen production rates considerably [98]. Although attempts to design electrolysis cell to reduce ohmic losses results in some improvement of hydrogen production rates, the improvement of the electrical conductivity of the electrolytic solution is necessary for substantial improvement of the hydrogen production. The nano-fluid formed via mixture of water and Carbon nanotubes (CNT) has higher electrical conductivity than pure water because of significantly high electrical conductivity of CNT. Consequently, improvement of electrical properties of water through addition of CNT gives rise to increased hydrogen production rate.

The current-time characteristics of the hydrogen production unit are shown in Figures (71-77) for deionized water, various CNT concentrations, and three concentrations of waste fluid obtained from the food industry. Figure (78) and (79) show the gas chromatograph detector response verses the retention time for all of the nanofluid and the waste water samples.

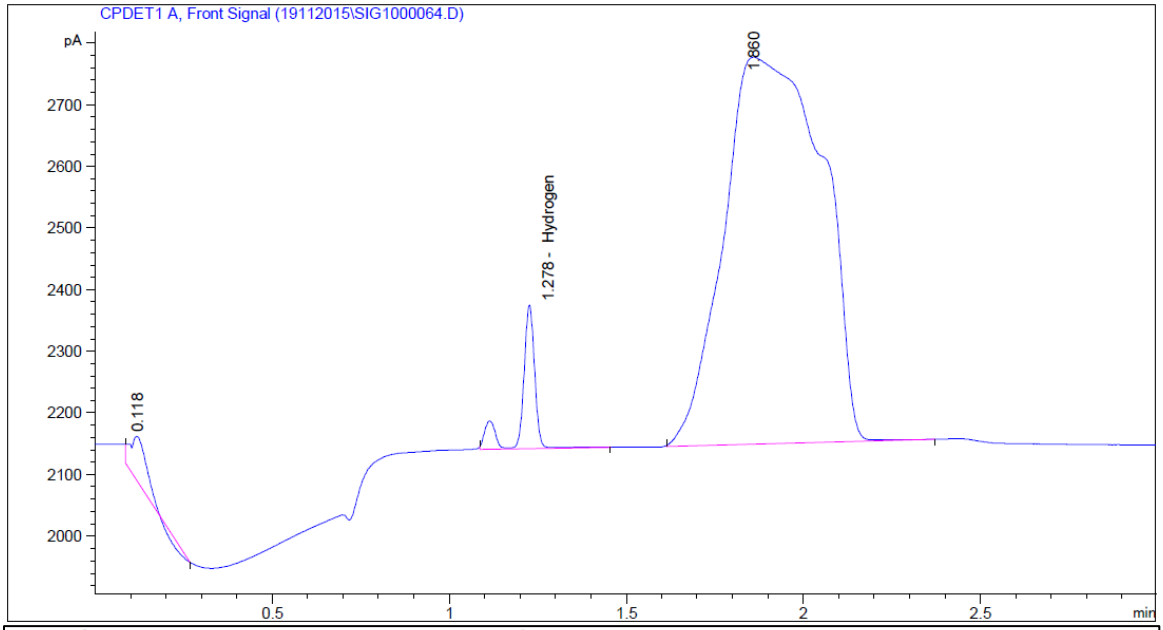

RetTime [min]	Type	Area [pA*s]	Amt/Area	Amount [PPM]	Grp	Name
1.278	VVA+	583.27972	3.86460e-3	2.25415		Hydrogen
2.287		-	-	-		O2 + N2
2.709		-	-	-		CO
5.104		-	-	-		Methane
Totals :				2.25415		

Figure 71: Gas Chromatograph detector response verses the retention time in minutes for Deionized water

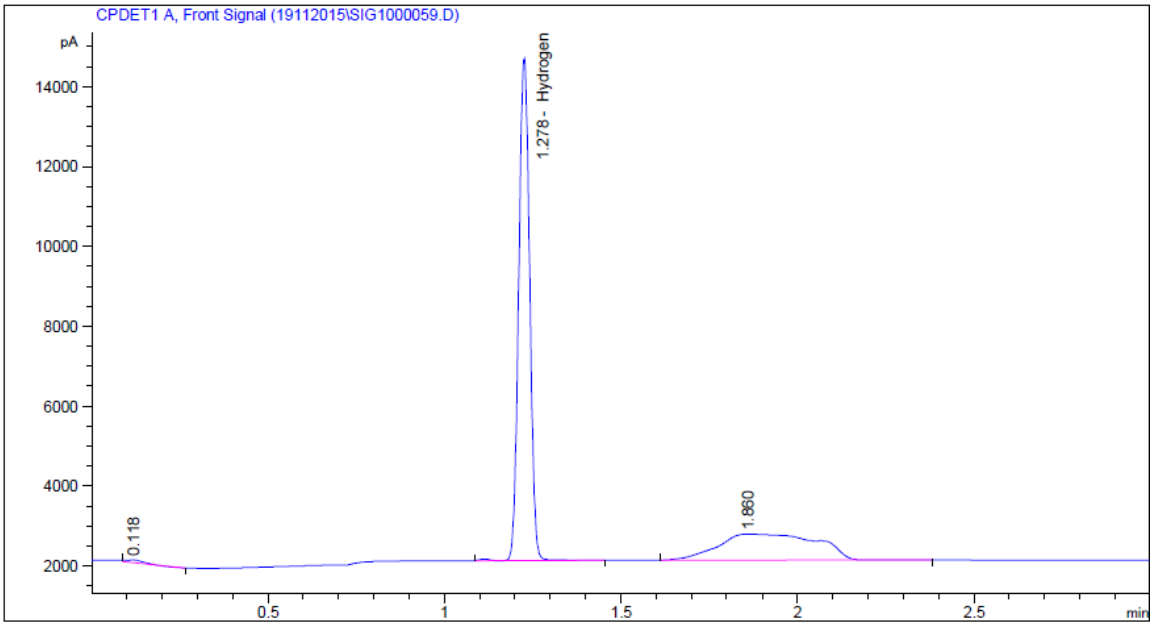

RetTime [min]	Type	Area [pA*s]	Amt/Area	Amount [PPM]	Grp	Name
1.278	VBA+	2.71342e4	3.86460e-3	104.86305		Hydrogen
2.287		-	-	-		O2 + N2
2.709		-	-	-		CO
5.104		-	-	-		Methane
Totals :				104.86305		

Figure 72: Gas Chromatograph detector response verses the retention time in minutes for a sample comprises 0.025 wt% of CNT in water

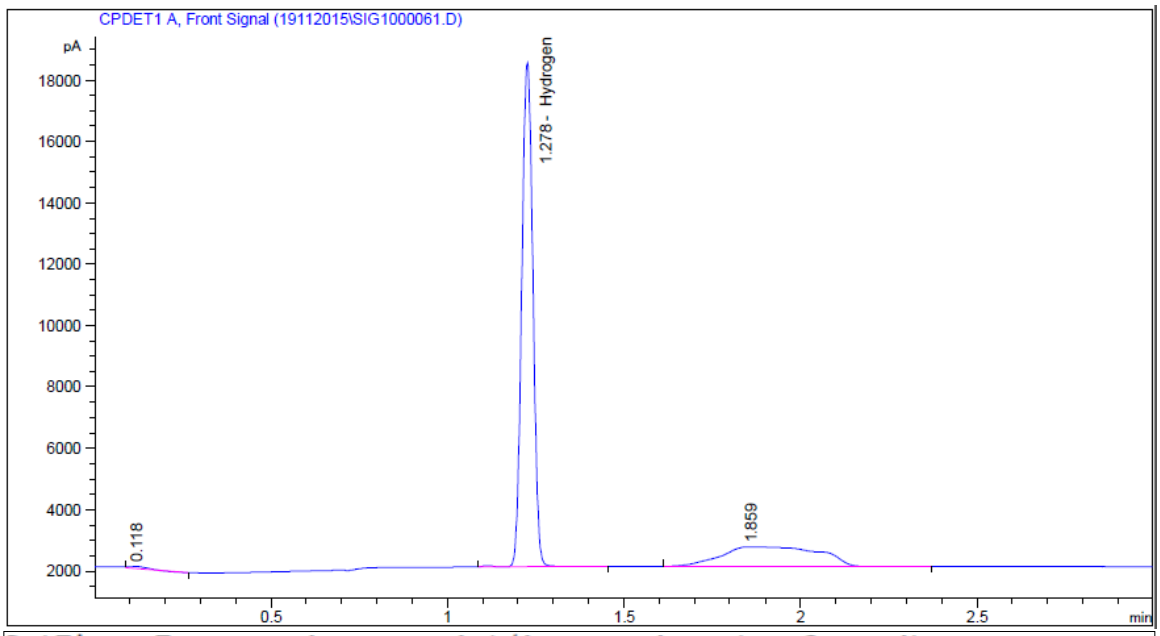

RetTime [min]	Type	Area [pA*s]	Amt/Area	Amount [PPM]	Grp	Name
1.278	VBA+	3.62184e4	3.86460e-3	139.96996		Hydrogen
2.287		-	-	-		O2 + N2
2.709		-	-	-		CO
5.104		-	-	-		Methane
Totals :				139.96996		

Figure 73: Gas Chromatograph detector response verses the retention time in minutes for a sample comprises 0.05 wt% of CNT in water

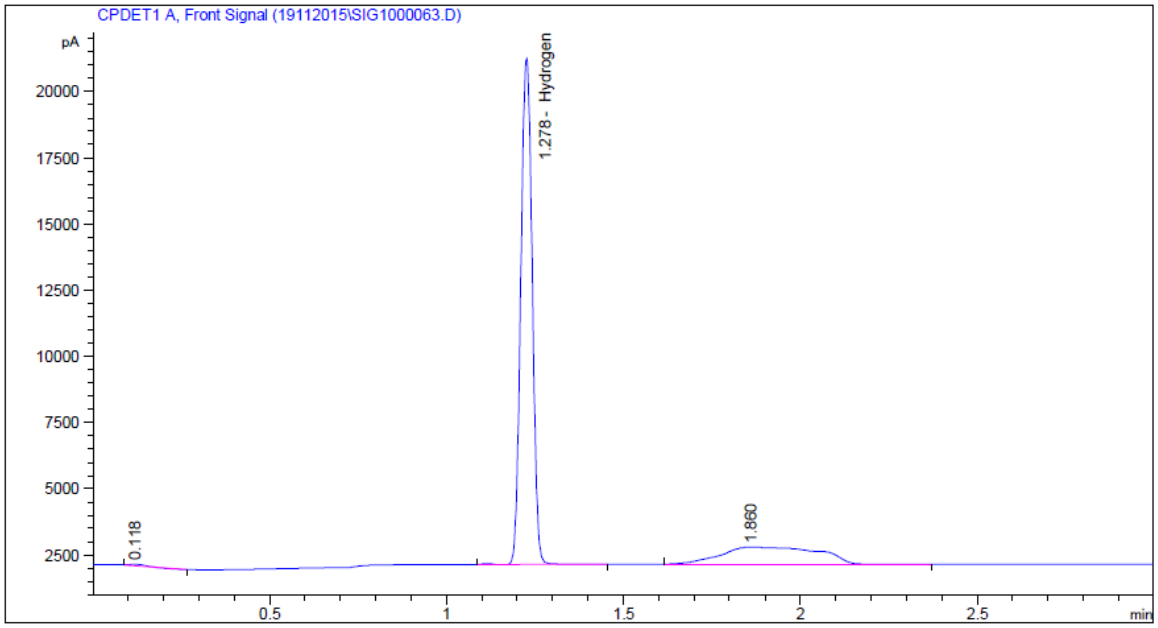

RetTime [min]	Type	Area [pA*s]	Amt/Area	Amount [PPM]	Grp	Name
1.278	VBA+	4.29313e4	3.86460e-3	165.91258		Hydrogen
2.287		-	-	-		O2 + N2
2.709		-	-	-		CO
5.104		-	-	-		Methane
Totals :				165.91258		

Figure 74: Gas Chromatograph detector response verses the retention time in minutes for a sample comprises 0.1 wt% of CNT in water

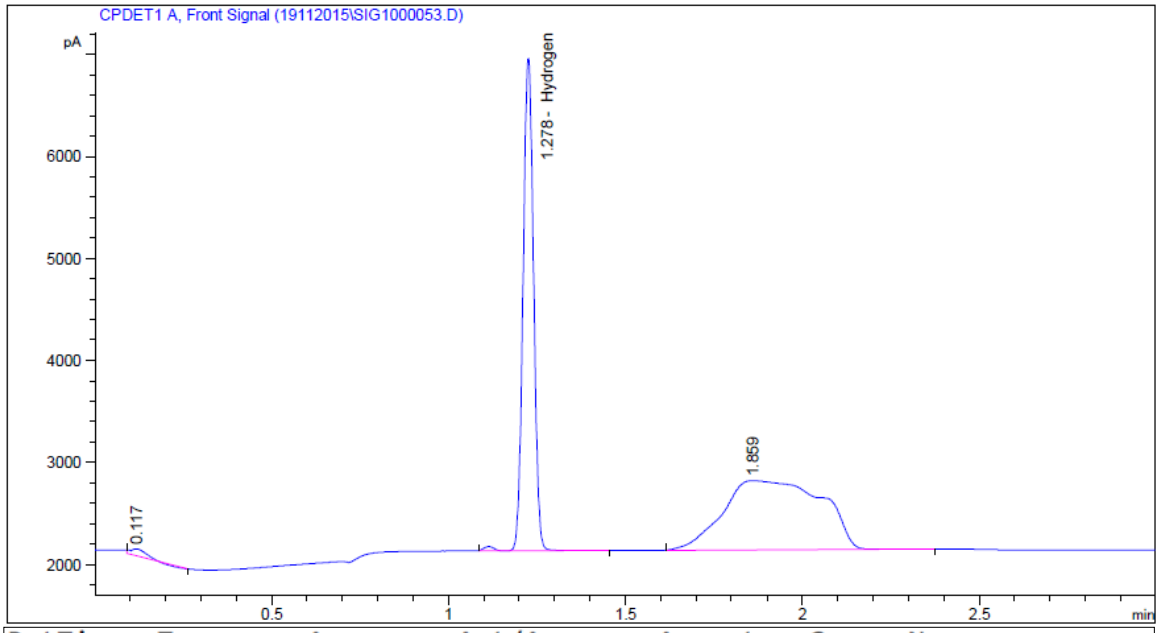

RetTime [min]	Type	Area [pA*s]	Amt/Area	Amount [PPM]	Grp	Name
1.278	VVA+	1.00518e4	3.86460e-3	38.84610		Hydrogen
2.287		-	-	-		O2 + N2
2.709		-	-	-		CO
5.104		-	-	-		Methane
Totals :				38.84610		

Figure 75: Gas Chromatograph detector response verses the retention time in minutes for a sample comprises 25 wt% waste water and 75wt% deionized water

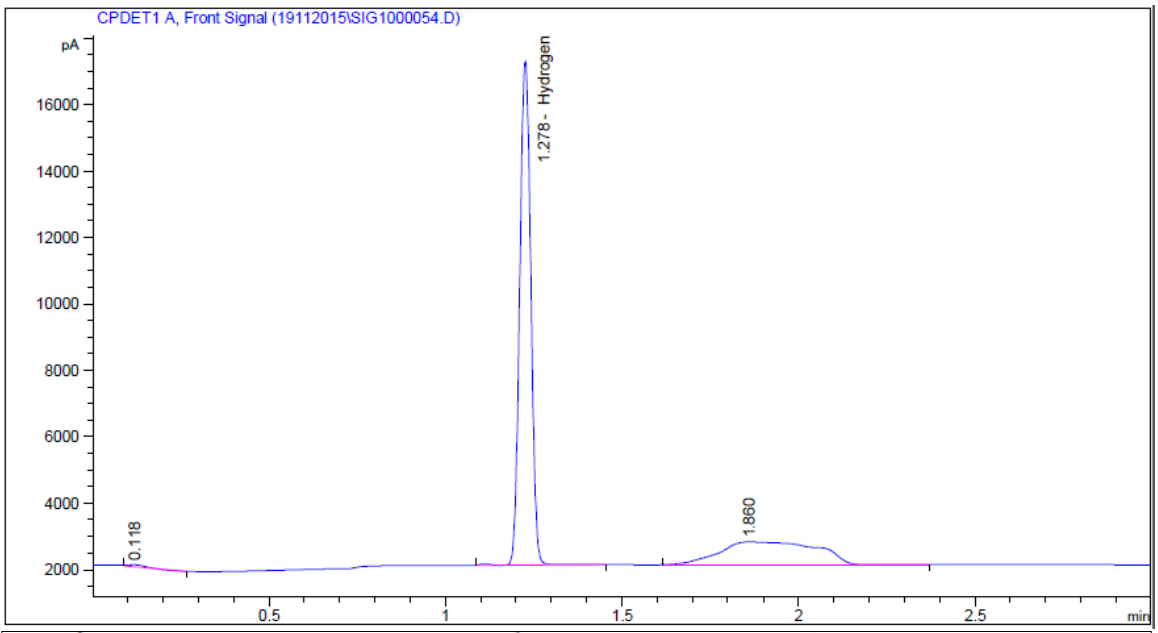

RetTime [min]	Type	Area [pA*s]	Amt/Area	Amount [PPM]	Grp	Name
1.278	VBA+	3.32092e4	3.86460e-3	128.34026		Hydrogen
2.287		-	-	-		O2 + N2
2.709		-	-	-		CO
5.104		-	-	-		Methane
Totals :				128.34026		

Figure 76: Gas Chromatograph detector response verses the retention time in minutes for a sample comprises 50 wt% waste water and 100 wt% deionized water

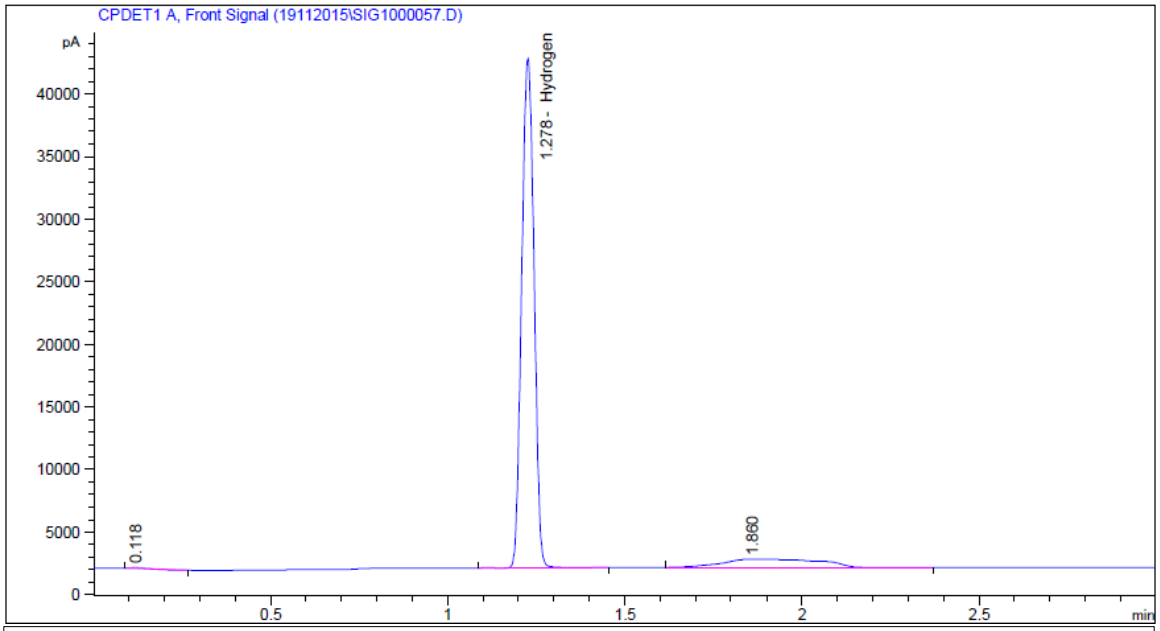

RetTime [min]	Type	Area [pA*s]	Amt/Area	Amount [PPM]	Grp	Name
1.278	VBA+	9.87550e4	3.86460e-3	381.64913		Hydrogen
2.287		-	-	-		O2 + N2
2.709		-	-	-		CO
5.104		-	-	-		Methane
Totals :				381.64913		

Figure 77: Gas Chromatograph detector response verses the retention time in minutes for a sample comprises waste water

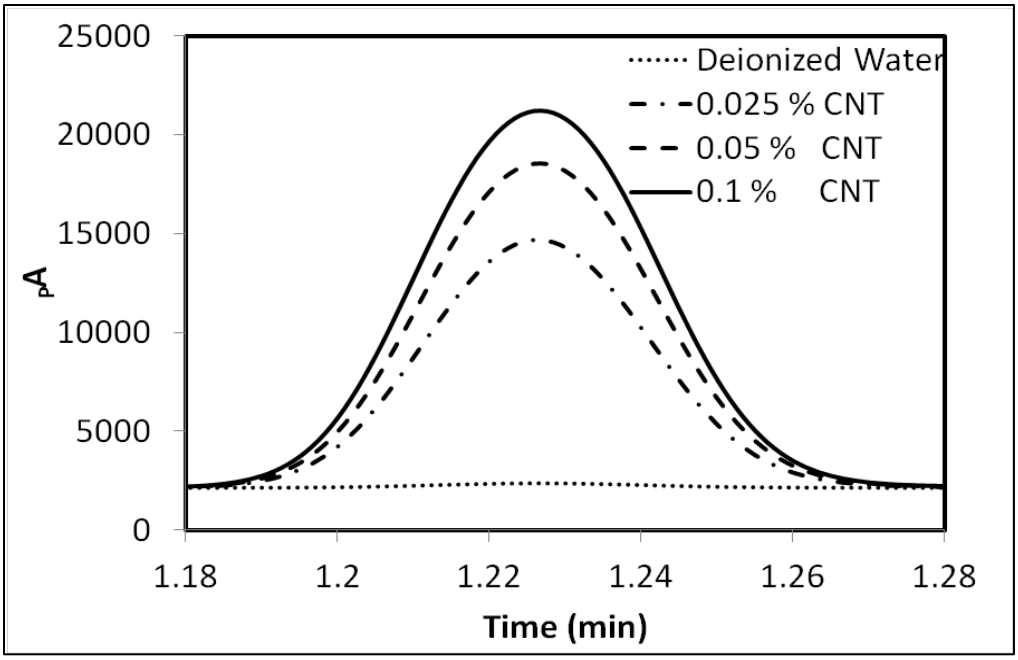

Figure 78: Gas Chromatograph detector response verses the retention time in minutes for the nanofluid samples comprises0.025, 0.05 and 0.1 wt% of CNT in water

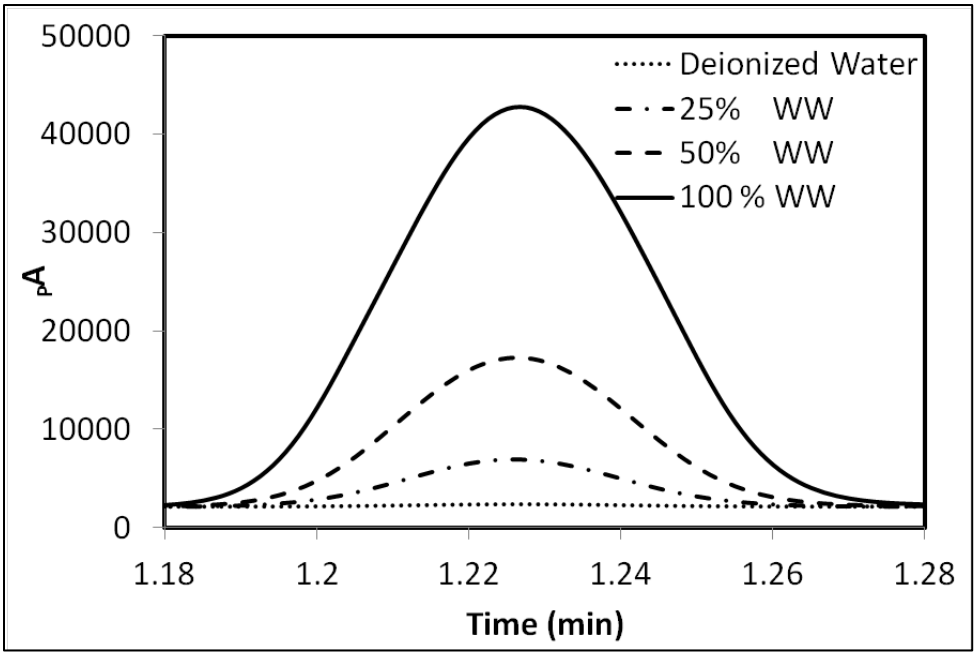

Figure 79: Gas Chromatograph detector response verses the retention time in minutes for a sample comprises 25, 50, 100 wt% of wastewater in water

The use of CNT in the carrier fluid, which is water, provides enhancement of electrical conductivity, which is also shown in Figure (80). However, pH of the water and CNT mixture changes slightly as compared to the distilled water. The slight change in pH is associated with the acid treatment of CNT prior to mixing with water. In this case, some oxides residues located around CNT may dissolve in water and alters pH level. Moreover, this effects the concentration of ionic solution in the water and alters the electrical resistance of the electrolytic solution. The concentration of the electrolytic solution also causes corrosion attack to the electrodes and decomposition of anode, despite the fact that increase of concentration results in enhancement in hydrogen production [99]. In this case, increase in hydrogen production is associated with high number of effective ionic collisions per unit time [99]. Since the change in pH is small, this effect is overruled in the present study. Moreover, inclusion of CNT reduces both the thermal and electrical resistances of the electrolytic solution. In this case, heat generation in the electrolytic solution reduces because of the reduction in electrical resistance. The improvement in thermal conductivity as shown in Figure (81) enhances the heat dissipation in the electrolytic solution while increasing the hydrogen production as shown in Figure (82). Consequently, local temperature increase, particularly in the close region of anode is suppressed by using the CNT in the carrier fluid. However, it was reported that increasing temperature of the solution enhances hydrogen production in a linear fashion [100]. On the other hand, energy needed for the electrolysis increases because of heat dissipation when the electrical resistance of the solution increases. Therefore, the energy input for electrolysis increases because of the energy dissipated through the electrical resistance of the solution. Although hydrogen production increases

in a linear fashion with temperature increase, energy dissipated because of the electrical resistance of the electrolytic solution is substantial. Therefore, the dissipated energy, in terms of heat, may be used effectively to produce hydrogen more than that corresponding to the enhancement of hydrogen production due to temperature increase. In this case, the ohmic loses plays major role for temperature rise, provided that it has an adverse effect on the performance of the electrolysis process [98].

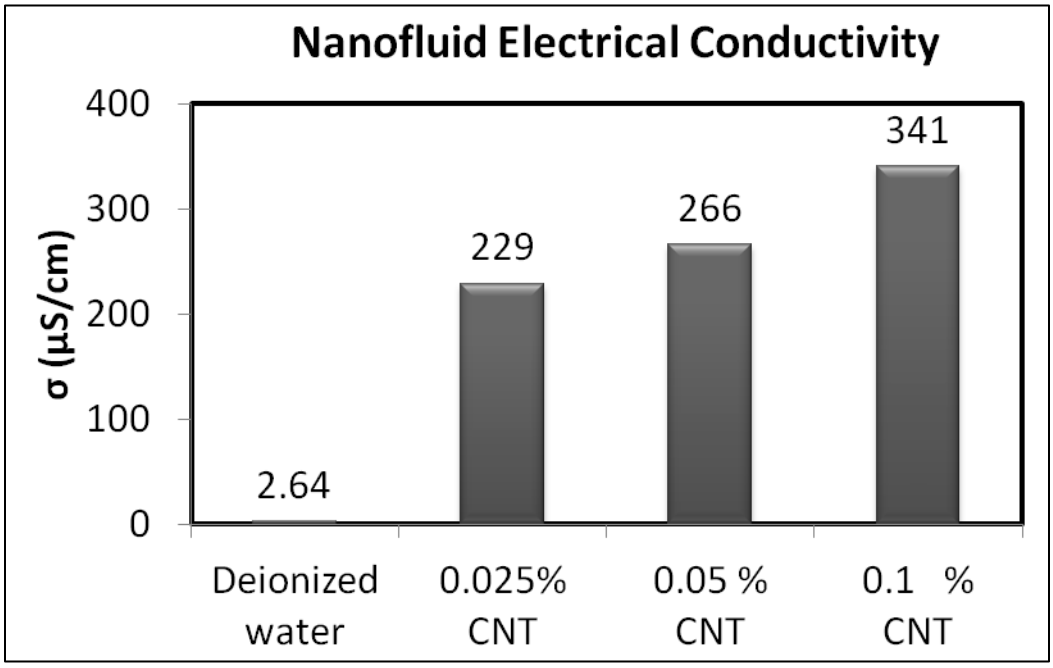

Figure 80: Nanofluid electrical conductivity

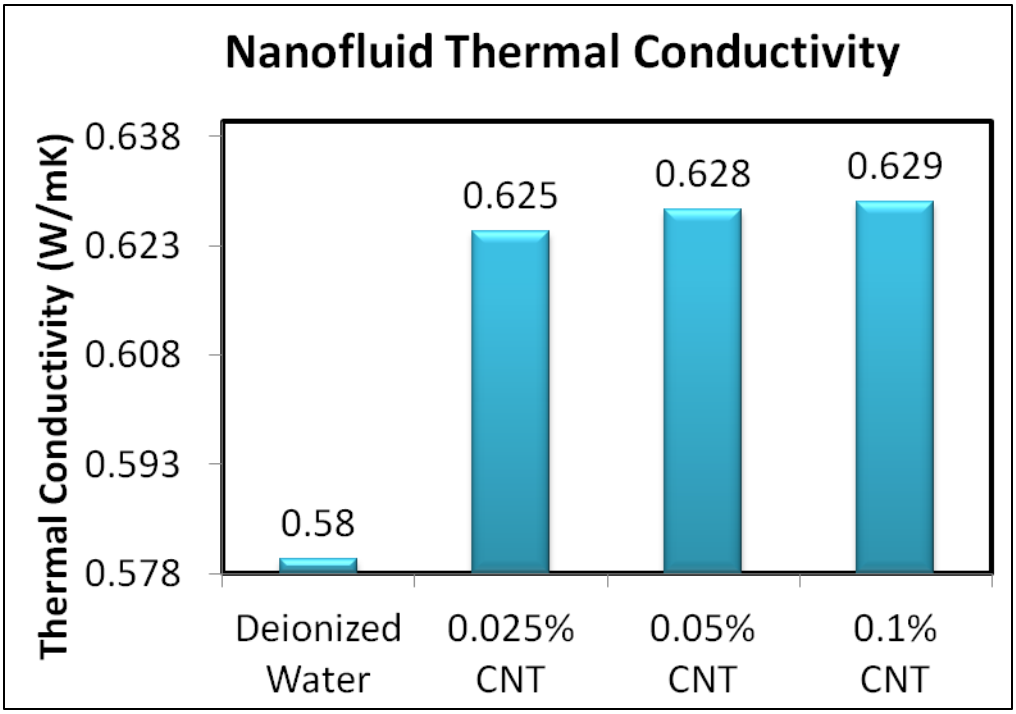

Figure 81: Nanofluid thermal Conductivity

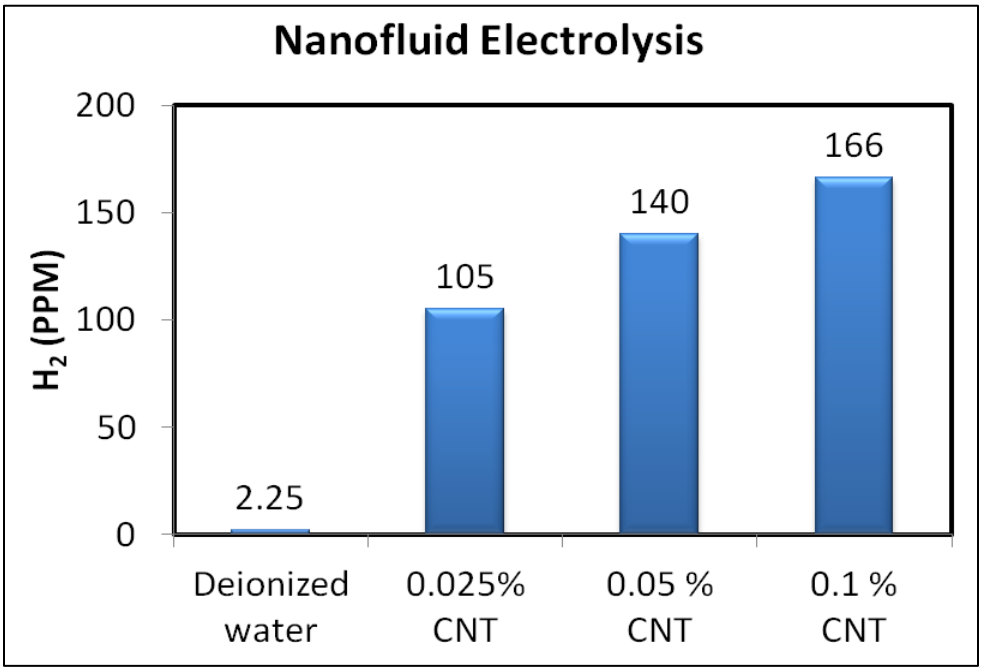

Figure 82: Nanofluid hydrogen production via electrolysis

Although the effect of electrode, applied voltage, and time on the hydrogen production is important, these affects are not studied in details because of the experimental facilities available during this study. It should be noted that increasing applied voltage increases hydrogen production rate as reported in the early study [101]. In addition, the electrodes should remain stable state without any destruction on the electrode surface for prolonged production time. In the case of the waste water obtained from food industry, increasing concentration of the organic substances in the solution increases the electrical conductivity of the solution, which can be seen from Figure (83). Hydrogen production increases significantly with increasing concentration of the organic compounds. This situation can be seen from Figure (84), in which the hydrogen production is shown for three concentrations of the electrolytic solution. The rate of increase with concentration is not linear, which indicates that increasing electrical conductivity results in similar trend in the hydrogen production rate. Although electrical resistance plays an important role in the heat generation in the electrolytic solution, the effect of temperature increase in the solution does not observe to be significantly important on the hydrogen production rate in the present case. This is associated with the rise of temperature during the electrolysis, which is in the order of few degrees centigrade.

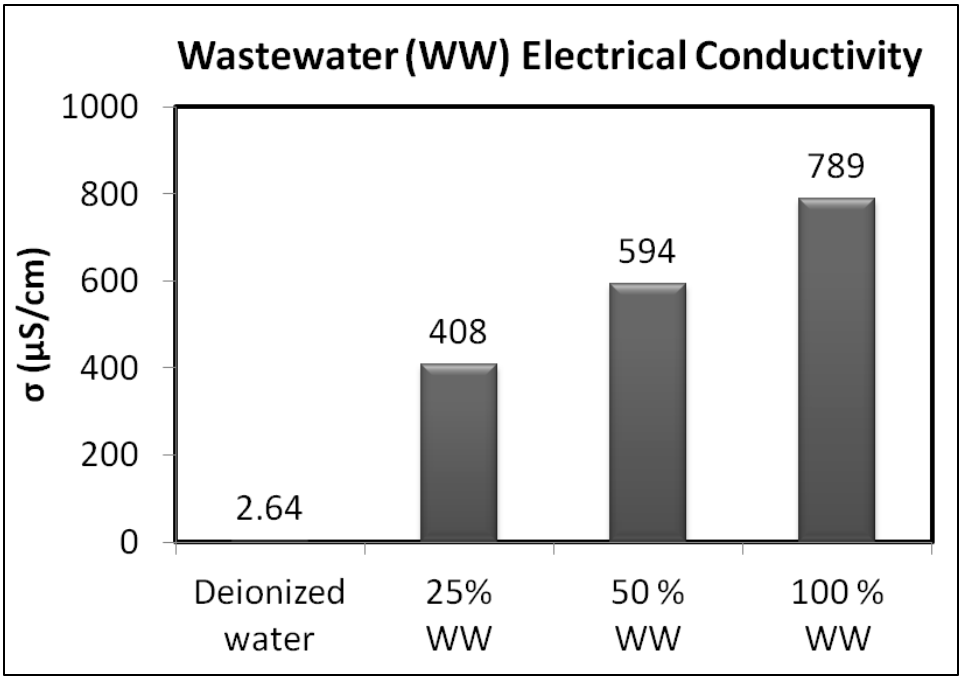

Figure 83: Wastewater (WW) electrical conductivity

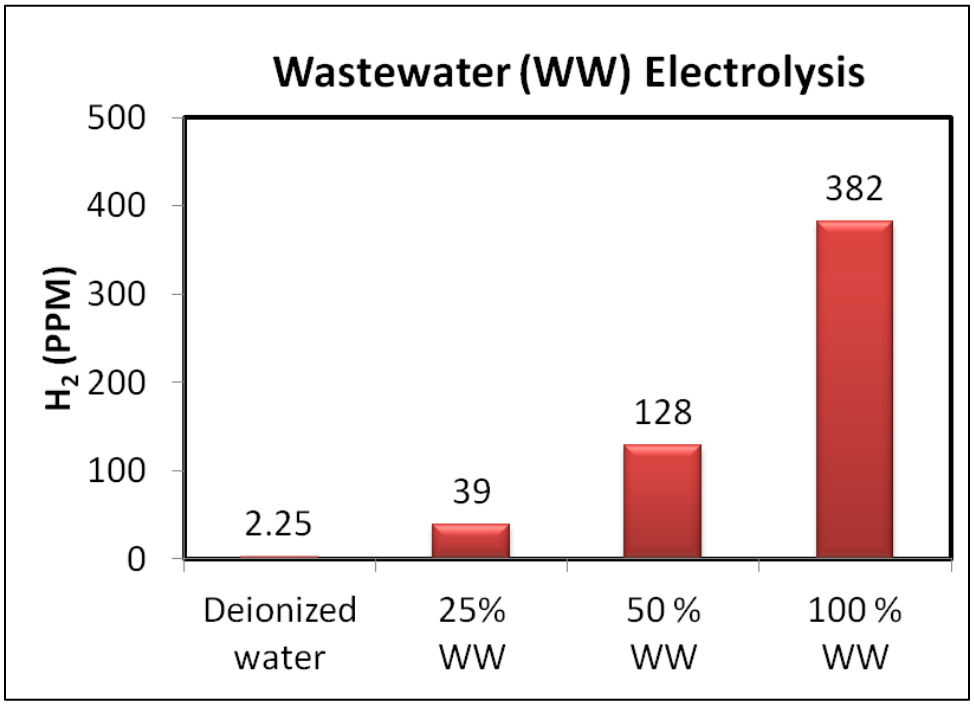

Figure 84: Waste water hydrogen production via electrolysis

CHAPTER 5

CONCLUSIONS

5.1 Summary

In this dissertation, several aspects of performance assessment of a combined cycle related to a power plant incorporating renewable energy sources and hydrogen production are presented. Energy and exergy analysis for the thermal system composes of various components in the combined cycle power plant are included and performance indicators are incorporated when evaluating the system thermal performance. The study also covers economic aspects of the thermal system in terms of exergoeconomic analysis. In addition, an experiment is conducted for possible hydrogen production utilizing conductive nanofluids such as Carbon Nano Tubes and water mixture. The study extended to include the surface characteristics pertinent to nanofluid behavior in droplets, which provide assessment of small particles behavior on the wetted surfaces. Numerical simulations are

carried out to predict the flow field and particle motions in a droplet resembling on the wetted surfaces in relation to self-cleaning of protective glasses for photovoltaic panel and the sections of the inside parts in the electrolyzer unit, which are incorporated in the present study.

Conclusions driven from this dissertation are included under appropriate subsections.

5.2 Overall Performance Analysis of a Combined Power Plant

An exergo-economic analysis was carried out using GT PRO/PEACE Software Packages for combined cycle power plant to determine the optimum configuration for Dhahran, Saudi Arabia. Four performance indicators were considered in the optimization study. These are energy efficiency (ENE [%]), exergy efficiency (EXE [%]), levelized cost of electricity (COE [$/kWh]), and the total investment (TI [MM$]). An Overall performance index is defined in which these four performance indicators are considered with their assigned weight factors to come up with the optimum configuration. Three cases of selection strategies were considered; namely, the conventional case in which the levelized cost of electricity is given a higher priority, the environmental conscious case in which the exergy efficiency is given a higher priority, and the economical case in which the total cost of investment is given a higher priority. It was shown that the optimum configuration and the size of the power plant are different in each of the cases considered. The optimum size (i.e. the pressure ratio) of the gas turbine was found to be 18 for the

conventional case, 16 for the environmental conscious case, and 12 for the economical case.

5.3 Techno-Economic Analysis and Optimization of Different Renewable Energy Systems for Power Generation and Hydrogen Production

Power generation and hydrogen production via renewable energy are investigated at different locations in the Kingdom of Saudi Arabia. The effect of changing solar radiation and wind speed on the power generated are analyzed. Six different renewable power generation systems are considered during hourly base simulation with the aid of HOMER Software. PV array, wind turbines or a combination of PV array and wind turbines in a hybrid system are the power generation alternatives in this study. As storage systems, two scenarios are considered; battery bank or a combination of electrolyzer, fuel cell and hydrogen tank storage system. In the second storage system, the generated power by the system meets the load requirements and the surplus energy goes to the electrolyzer where hydrogen is produced and forward to the hydrogen tank for later use.

For each system, the simulations were repeated at five areas in the Kingdom, namely; Dhahran, Riyadh, Jeddah, Abha and Yanbu, to compare solar and wind renewable energy potentials. Since every location has different solar radiation intensities and wind speed levels throughout full year range of simulations, different configurations of the power generation systems components are expected at each location to meet the same load requirements. The findings revealed that the hybrid renewable energy system that

integrate solar and wind resources through PV array and wind turbines with battery bank storage system, leads to give the minimum cost of energy (COE) of 0.609 $/kWh at Yanbu area. This is true with either storage batteries systems or the systems that comprises of fuel cell, electrolyzer and hydrogen tank as a storage system where the minimum COE of 1.208 $/kWh is achieved at Abha. Hydrogen production by the use of renewable energy resources makes it possible to have an environmental friendly fuel. The results also showed that replacing the battery bank storage system by a combination of fuel cell, electrolyzer and hydrogen tank storage system is possible; however, the cost is still high due to the higher cost of investment. The findings of the present study also provide useful information about the renewable energy potentials in the Kingdom of Saudi Arabia.

5.4 Thermal and Electrical Characteristics of Semi-Conductive Nanofluid

Thermal and electrical characteristics of water-CNT nanofluid mixture are investigated. The characteristics of the CNT and the water mixture include effective, density, thermal conductivity, specific heat capacity, and electrical conductivity. The study is extended to include the influence of CNT concentration on these characteristics. Micro-images representing the actual distribution of the CNT particles in the water mixture are obtained under the microscope for various CNT concentrations used in the experiments. The micro-images are transferred to the multi-physics numerical code and thermal and electrical fields are computed to assess the thermal and the electrical characteristics of the

mixture. Various cases are simulated for different CNT concentrations incorporating the proper boundary conditions for each case of thermal or electrical fields. In addition, experiments are conducted to measure the effective specific heat capacity and the effective electrical conductivity of the mixture. It is found that the results obtained from the experiments agree well with their counterparts resulted from the predictions. The effective thermal conductivity is determined from both mass based analysis and the simulations incorporating the actual image of the nanofluid mixture. The results show that the thermal conductivity determined from the simulations is significantly lower than that corresponding to the mass based analysis. This is because of the carbon nanotubes which are not well connected in the water mixture and the heat conduction is suppressed by the low thermal conductivity of the water located in between the carbon nanotubes in the mixture. The findings reveals that using the mass based analysis to predict the effective mean thermal conductivity results in an erroneously prediction of high thermal conductivity values. It is also observed from the simulations that high values of the thermal heat flux and the current density occur in the vicinity of the CNT boundaries due to higher thermal and electrical conductivities of CNT as compared to the water. For all thermal and electrical properties of water-CNT mixture, mathematical expressions are introduced to predict the properties as a function of CNT concentration. The findings reveal that good agreement between the numerical and mathematical expressions is resulted and the errors for these relations are found to be negligibly small. The findings of the present study provide useful information about the nanofluid properties, particularly water-CNT mixture, for designing the thermo-fluid systems.

5.5 Hydrogen Production via electrolysis incorporating CNT-Water Nanofluid and Industrial Waste Water

Hydrogen production via electrolysis process was investigated experimentally. Due to the poor inherent thermal and electrical conductivities of the pure water, the hydrogen production rate was very low. For possible hydrogen production rate enhancement, small concentration ratios of the Carbon Nano Tubes (CNT) were introduced to the pure water, namely; 0.025, 0.05 and 0.1 wt%. The electrical conductivity measurements showed that increasing the concentration ratio of CNT in the pure water led to increase the electrical conductivity of the mixture and enhance the hydrogen production rate. This is due to the higher electrical conductivity of the CNT comparing to the water.

Waste water obtained from food industry contains high amount of hydrocarbons, which can be utilized for the hydrogen production. The presence of organic substances in the solution increases the electrical conductivity of the solution. As compared to the mixture of water and CNT as well as the distilled water, hydrogen production improves when the organic solution is used as an electrolytic solution such as the waste water from the food industry. Consequently, the present study clearly demonstrates that the waste water from the food industry has a great potential to produce hydrogen using the electrolysis method. However, the proper settings of the concentrations of the organic compounds are important to increase the rate of hydrogen production.

REFERENCES

1. Thomas, G., *Overview of storage development DOE hydrogen program.* Sandia National Laboratories, 2000. **9**.
2. Züttel, A., A. Borgschulte, and L. Schlapbach, *Hydrogen as a future energy carrier*. 2011: John Wiley & Sons.
3. *COMSOL Multiphysics*, *http://www.comsol.com/comsol-multiphysics*. November, 2015.
4. Al-Sharafi, A., A.Z. Sahin, and B.S. Yilbas, *Overall performance index for hybrid power plants.* Energy Conversion and Management, 2015. **100**: p. 103-116.
5. *GT PRO\PEACE, http://www.thermoflow.com/combinedcycle_GTP.html*. November, 2015.
6. *HOMER , http://www.homerenergy.com* November 2015.
7. Bejan, A., G. Tsatsaronis, and M.J. Moran, *Thermal design and optimization*. 1996: John Wiley & Sons.
8. Dincer, I. and H. Al-Muslim, *Thermodynamic analysis of reheat cycle steam power plants.* International Journal of Energy Research, 2001. **25**(8): p. 727-739.
9. Ameri, M., P. Ahmadi, and A. Hamidi, *Energy, exergy and exergoeconomic analysis of a steam power plant: a case study.* International Journal of Energy Research, 2009. **33**(5): p. 499-512.
10. Kaviri, A.G., et al., *Exergoenvironmental optimization of heat recovery steam generators in combined cycle power plant through energy and exergy analysis.* Energy conversion and management, 2013. **67**: p. 27-33.

11. Memon, A.G., et al., *Parametric based thermo-environmental and exergoeconomic analyses of a combined cycle power plant with regression analysis and optimization.* Energy Conversion and Management, 2015. **92**: p. 19-35.

12. Carcasci, C. and B. Facchini, *Comparison between two gas turbine solutions to increase combined power plant efficiency.* Energy conversion and management, 2000. **41**(8): p. 757-773.

13. Bandayapadhyay, S., N. Bera, and S. Bhattacharyya, *Thermoeconomic optimization of combined cycle power plants. Energy conversion and management.* vol, 2001. **42**: p. 359-371.

14. Marrero, I., et al., *Second law analysis and optimization of a combined triple power cycle.* Energy Conversion and Management, 2002. **43**(4): p. 557-573.

15. Carapellucci, R. and A. Milazzo, *Repowering combined cycle power plants by a modified STIG configuration.* Energy Conversion and Management, 2007. **48**(5): p. 1590-1600.

16. Polyzakis, A., C. Koroneos, and G. Xydis, *Optimum gas turbine cycle for combined cycle power plant.* Energy conversion and management, 2008. **49**(4): p. 551-563.

17. Woudstra, N., et al., *Thermodynamic evaluation of combined cycle plants.* Energy Conversion and Management, 2010. **51**(5): p. 1099-1110.

18. Ozturk, M., *Energy and exergy analysis of a combined ground source heat pump system.* Applied Thermal Engineering, 2014. **73**(1): p. 362-370.

19. Fontalvo, A., et al., *Exergy analysis of a combined power and cooling cycle.* Applied Thermal Engineering, 2013. **60**(1): p. 164-171.

20. Baghernejad, A. and M. Yaghoubi, *Exergy analysis of an integrated solar combined cycle system.* Renewable Energy, 2010. **35**(10): p. 2157-2164.

21. Khaljani, M., R.K. Saray, and K. Bahlouli, *Comprehensive analysis of energy, exergy and exergo-economic of cogeneration of heat and power in a combined gas turbine and organic Rankine cycle.* Energy Conversion and Management, 2015. **97**: p. 154-165.

22. Al-Sulaiman, F.A., *Exergy analysis of parabolic trough solar collectors integrated with combined steam and organic Rankine cycles.* Energy Conversion and Management, 2014. **77**: p. 441-449.

23. Yang, H., Z. Wei, and L. Chengzhi, *Optimal design and techno-economic analysis of a hybrid solar–wind power generation system.* Applied Energy, 2009. **86**(2): p. 163-169.

24. Diaf, S., et al., *A methodology for optimal sizing of autonomous hybrid PV/wind system.* Energy Policy, 2007. **35**(11): p. 5708-5718.

25. Nfah, E., J. Ngundam, and R. Tchinda, *Modelling of solar/diesel/battery hybrid power systems for far-north Cameroon.* Renewable Energy, 2007. **32**(5): p. 832-844.

26. Nfah, E. and J. Ngundam, *Modelling of wind/diesel/battery hybrid power systems for far North Cameroon.* Energy conversion and management, 2008. **49**(6): p. 1295-1301.

27. Arribas, L., et al., *PV–wind hybrid system performance: A new approach and a case study.* Renewable energy, 2010. **35**(1): p. 128-137.

28. Zhou, W., H. Yang, and Z. Fang, *Battery behavior prediction and battery working states analysis of a hybrid solar–wind power generation system.* Renewable Energy, 2008. **33**(6): p. 1413-1423.

29. Shiroudi, A., et al., *Stand-alone PV-hydrogen energy system in Taleghan-Iran using HOMER software: optimization and techno-economic analysis.* Environment, development and sustainability, 2013. **15**(5): p. 1389-1402.

30. Kalinci, Y., *Alternative energy scenarios for Bozcaada island, Turkey.* Renewable and Sustainable Energy Reviews, 2015. **45**: p. 468-480.

31. Silva, S., M. Severino, and M. De Oliveira, *A stand-alone hybrid photovoltaic, fuel cell and battery system: a case study of Tocantins, Brazil.* Renewable Energy, 2013. **57**: p. 384-389.

32. Dursun, B., *Determination of the optimum hybrid renewable power generating systems for Kavakli campus of Kirklareli University, Turkey.* Renewable and Sustainable Energy Reviews, 2012. **16**(8): p. 6183-6190.

33. El Khashab, H. and M. Al Ghamedi, *Comparison between hybrid renewable energy systems in Saudi Arabia.* Journal of Electrical Systems and Information Technology, 2015.

34. Rehman, S., et al., *Feasibility study of a wind–pv–diesel hybrid power system for a village.* Renewable Energy, 2012. **38**(1): p. 258-268.

35. Mokheimer, E.M., et al., *A New Study for Hybrid PV/Wind off-Grid Power Generation Systems with the Comparison of Results from Homer*. International Journal of Green Energy, 2015. **12**(5): p. 526-542.

36. Elhadidy, M., *Performance evaluation of hybrid (wind/solar/diesel) power systems.* Renewable Energy, 2002. **26**(3): p. 401-413.

37. Rehman, S., *Wind energy resources assessment for Yanbo, Saudi Arabia.* Energy Conversion and Management, 2004. **45**(13): p. 2019-2032.

38. Shaahid, S. and I. El-Amin, *Techno-economic evaluation of off-grid hybrid photovoltaic–diesel–battery power systems for rural electrification in Saudi Arabia—a way forward for sustainable development.* Renewable and Sustainable Energy Reviews, 2009. **13**(3): p. 625-633.

39. Harish, S., et al., *Enhanced thermal conductivity of ethylene glycol with single-walled carbon nanotube inclusions.* International Journal of heat and mass transfer, 2012. **55**(13): p. 3885-3890.

40. Nasiri, A., et al., *Effect of CNT structures on thermal conductivity and stability of nanofluid.* International Journal of heat and Mass transfer, 2012. **55**(5): p. 1529-1535.

41. Mondragón, R., et al. *Characterization of physical properties of nanofluids for heat transfer application*. in *Journal of Physics: Conference Series*. 2012. IOP Publishing.

42. Jeong, J., et al., *Particle shape effect on the viscosity and thermal conductivity of ZnO nanofluids.* International Journal of Refrigeration, 2013. **36**(8): p. 2233-2241.

43. Moghaddami, M., A. Mohammadzade, and S.A.V. Esfehani, *Second law analysis of nanofluid flow*. Energy Conversion and Management, 2011. **52**(2): p. 1397-1405.

44. Santra, A.K., S. Sen, and N. Chakraborty, *Study of heat transfer due to laminar flow of copper–water nanofluid through two isothermally heated parallel plates.* International Journal of Thermal Sciences, 2009. **48**(2): p. 391-400.

45. Colla, L., et al., *Water-based Fe2O3 nanofluid characterization: thermal conductivity and viscosity measurements and correlation.* Advances in Mechanical Engineering, 2012. **4**: p. 674947.

46. Lamas, B., et al., *Critical analysis of the thermal conductivity models for CNT based nanofluids.* International Journal of Thermal Sciences, 2014. **78**: p. 65-76.

47. Mallick, S., A. Mishra, and L. Kundan, *An investigation into modelling thermal conductivity for alumina–water nanofluids.* Powder Technology, 2013. **233**: p. 234-244.

48. Mohebbi, A., *Prediction of specific heat and thermal conductivity of nanofluids by a combined equilibrium and non-equilibrium molecular dynamics simulation.* Journal of Molecular Liquids, 2012. **175**: p. 51-58.

49. Maxwell, J.C., *A treatise on electricity and magnetism*. Vol. 1. 1881: Clarendon press.

50. Hamilton, R. and O. Crosser, *Thermal conductivity of heterogeneous two-component systems.* Industrial & Engineering chemistry fundamentals, 1962. **1**(3): p. 187-191.

51. Yu, W. and S. Choi, *The role of interfacial layers in the enhanced thermal conductivity of nanofluids: a renovated Maxwell model.* Journal of Nanoparticle Research, 2003. **5**(1-2): p. 167-171.

52. Tam, D., et al., *Marangoni convection in droplets on superhydrophobic surfaces.* Journal of Fluid Mechanics, 2009. **624**: p. 101-123.

53. Tong, A.Y., S. Kasliwal, and H. Fujimoto, *On the successive impingement of droplets onto a substrate.* Numerical Heat Transfer, Part A: Applications, 2007. **52**(6): p. 531-548.

54. Francois, M. and W. Shyy, *Computations of drop dynamics with the immersed boundary method, part 2: Drop impact and heat transfer.* Numerical Heat Transfer: Part B: Fundamentals, 2003. **44**(2): p. 119-143.

55. Chen, L., et al., *Effects of roughness of gas diffusion layer surface on liquid water transport in micro gas channels of a proton exchange membrane fuel cell.* Numerical Heat Transfer, Part A: Applications, 2012. **62**(4): p. 295-318.

56. Sun, D., J. Xu, and Q. Chen, *Modeling of the Evaporation and Condensation Phase-Change Problems with FLUENT.* Numerical Heat Transfer, Part B: Fundamentals, 2014. **66**(4): p. 326-342.

57. Banerjee, R.K., et al., *Evaluation of Enhanced Heat Transfer Within a Four Row Finned Tube Array of an Air Cooled Steam Condenser.* Numerical Heat Transfer, Part A: Applications, 2012. **61**(10): p. 735-753.

58. Wegener, M., *A numerical parameter study on the impact of Marangoni convection on the mass transfer at buoyancy-driven single droplets.* International Journal of Heat and Mass Transfer, 2014. **71**: p. 769-778.

59. Girard, F., M. Antoni, and K. Sefiane, *On the effect of Marangoni flow on evaporation rates of heated water drops.* Langmuir, 2008. **24**(17): p. 9207-9210.

60. Thokchom, A.K., et al., *Analysis of fluid flow and particle transport in evaporating droplets exposed to infrared heating.* International Journal of Heat and Mass Transfer, 2014. **68**: p. 67-77.

61. Bhardwaj, R., X. Fang, and D. Attinger, *Pattern formation during the evaporation of a colloidal nanoliter drop: a numerical and experimental study.* New Journal of Physics, 2009. **11**(7): p. 075020.

62. Huang, L., et al., *Effect of contact angle on water droplet freezing process on a cold flat surface.* Experimental Thermal and Fluid Science, 2012. **40**: p. 74-80.

63. Talbot, E., et al., *Evaporation of picoliter droplets on surfaces with a range of wettabilities and thermal conductivities.* Physical Review E, 2012. **85**(6): p. 061604.

64. Chan, C.L. and C. Chen, *Effect of gravity on the stability of thermocapillary convection in a horizontal fluid layer.* Journal of Fluid Mechanics, 2010. **647**: p. 91-103.

65. Schatz, M.F. and G.P. Neitzel, *Experiments on thermocapillary instabilities.* Annual review of fluid mechanics, 2001. **33**(1): p. 93-127.

66. Shanahan, M., K. Sefiane, and J. Moffat, *Dependence of volatile droplet lifetime on the hydrophobicity of the substrate.* Langmuir, 2011. **27**(8): p. 4572-4577.

67. Rowan, S., M. Newton, and G. McHale, *Evaporation of microdroplets and the wetting of solid surfaces.* The Journal of Physical Chemistry, 1995. **99**(35): p. 13268-13271.

68. Cazabat, A.-M. and G. Guéna, *Evaporation of macroscopic sessile droplets.* Soft Matter, 2010. **6**(12): p. 2591-2612.

69. Murisic, N. and L. Kondic, *On evaporation of sessile drops with moving contact lines.* Journal of Fluid Mechanics, 2011. **679**: p. 219-246.

70. Lu, G., et al., *Internal flow in evaporating droplet on heated solid surface.* International Journal of Heat and Mass Transfer, 2011. **54**(19): p. 4437-4447.

71. Pregger, T., et al., *Prospects of solar thermal hydrogen production processes.* International Journal of Hydrogen Energy, 2009. **34**(10): p. 4256-4267.

72. Eker, S. and F. Kargi, *Hydrogen gas production from electrohydrolysis of industrial wastewater organics by using photovoltaic cells (PVC).* International Journal of Hydrogen Energy, 2010. **35**(23): p. 12761-12766.

73. Kargi, F., *Comparison of different electrodes in hydrogen gas production from electrohydrolysis of wastewater organics using photovoltaic cells (PVC).* international journal of hydrogen energy, 2011. **36**(5): p. 3450-3456.

74. Coskun, C., et al., *Investigation of biogas and hydrogen production from waste water of milk-processing industry in Turkey*. international journal of hydrogen energy, 2012. **37**(21): p. 16498-16504.

75. Kotas, T., *The Exergy Method of Thermal Plant AnalysisKrieger*. Melbourne, Australia, 1995.

76. OECD, I., *Projected costs of generating electricity*. 2010, OECD, Paris.

77. Ai, B., et al., *Computer-aided design of PV/wind hybrid system.* Renewable Energy, 2003. **28**(10): p. 1491-1512.

78. *https://www.oeko-energie.de/downloads/bp350u.pdf.* November, 2015.

79. http://www.windturbinewarehouse.com/pdfs/bergey/Bergey%20XL%201.0%20kW%20Turbine%20Specs.03-unenc.pdf. November, 2015.

80. http://www.kansaswindpower.net/bergey_wind_generators.htm. November, 2015.

81. http://www.pvpower.com/pdf/datasheets/concorde/pvx-2120l.pdf. November, 2015.

82. Lambert, T., P. Gilman, and P. Lilienthal, *Micropower system modeling with HOMER.* Integration of alternative sources of energy, 2006. **1**(15): p. 379-418.

83. Kumaresan, V. and R. Velraj, *Experimental investigation of the thermo-physical properties of water–ethylene glycol mixture based CNT nanofluids.* Thermochimica Acta, 2012. **545**: p. 180-186.

84. http://www.cheaptubes.com/mwnts.htm. November, 2015.

85. http://www.creative-nanotech.com/carbon_nanotubes.html. November, 2015.

86. http://www.us-nano.com/inc/sdetail/217. November, 2015.

87. Wu, G.S., et al. *Thermal conductivity measurement for carbon-nanotube suspensions with 3ω method*. in *Advanced Materials Research*. 2009. Trans Tech Publ.

88. Yi, W., et al., *Linear specific heat of carbon nanotubes.* Physical Review B, 1999. **59**(14): p. R9015.

89. Morsi, S. and A. Alexander, *An investigation of particle trajectories in two-phase flow systems.* Journal of Fluid Mechanics, 1972. **55**(02): p. 193-208.

90. *https://eosweb.larc.nasa.gov*. November, 2015.

91. Graham, V. and K. Hollands, *A method to generate synthetic hourly solar radiation globally.* Solar Energy, 1990. **44**(6): p. 333-341.

92. Sharif, M.N. and M.N. Islam, *The Weibull distribution as a general model for forecasting technological change.* Technological Forecasting and Social Change, 1980. **18**(3): p. 247-256.

93. *http://www.tainstruments.com/product.aspx?id=15&n=1&siteid=11*. November, 2015.

94. *http://www.ysi.com/index.php*. November, 2015.

95. *http://www.agilent.com/en-us/products/gas-chromatography/gc-systems/7890b-gc*. November, 2015.

96. Jia, Y.H., et al., *Hydrogen production from wastewater using a microbial electrolysis cell.* Korean Journal of Chemical Engineering, 2010. **27**(6): p. 1854-1859.

97. Dubey, P., et al., *Hydrogen generation by water electrolysis using carbon nanotube anode.* international journal of hydrogen energy, 2010. **35**(9): p. 3945-3950.

98. Yuvaraj, A. and D. Santhanaraj, *A systematic study on electrolytic production of hydrogen gas by using graphite as electrode.* Materials Research, 2014. **17**(1): p. 83-87.

99. Ito, H., et al., *Properties of Nafion membranes under PEM water electrolysis conditions.* international journal of hydrogen energy, 2011. **36**(17): p. 10527-10540.

100. Nikolić, V.M., et al., *Performance comparison of modified poly (vinyl alcohol) based membranes in alkaline fuel cells.* international journal of hydrogen energy, 2011. **36**(17): p. 11004-11010.

101. Khaselev, O., A. Bansal, and J. Turner, *High-efficiency integrated multijunction photovoltaic/electrolysis systems for hydrogen production.* International Journal of Hydrogen Energy, 2001. **26**(2): p. 127-132.

VITA

- Abdullah Mohammed Al-Sharafi
- Born in Hajah, Yemen on January 1st, 1978.
- Received Bachelor of Science (BSc) degree in Mechanical Engineering in June-2003 from Sana'a University, Sana'a, Yemen.
- Received First Honor Awards in all the semesters in the B.S. program.
- Received a scholarship from the Ministry of Higher Education to complete M.S. degree at King Fahd University of Petroleum and Minerals.
- Received Master of Science (Mechanical Engineering) degree in June-2011.
- Appointed as a Lecturer-B in Mechanical Engineering Department at King Fahd University of Petroleum & Minerals, Dhahran, Saudi Arabia in September-2011
- Completed PhD degree program requirements in Mechanical Engineering Department at King Fahd University of Petroleum & Minerals, Dhahran, Saudi Arabia in December 2015.
- Contact Details:
  - Present Address: Department of Mechanical engineering, King Fahd University of Petroleum and Minerals, Saudi Arabia.
  - E-mail Address:
    - alsharafi@kfupm.edu.sa
    - alsharafiy@gmail.com